On the experimental design of the material microstructures

by

Yauheni Staraselski

A thesis
presented to the University of Waterloo
in the fulfillment of the
thesis requirement for the degree of
Doctor of Philosophy
in
Mechanical Engineering

Waterloo, Ontario, Canada, 2014

I hereby declare that I am the sole author of this thesis. This is a true copy of the thesis, including any required final revisions, as accepted by my examiners.

I understand that my thesis may be made electronically available to the public.

ABSTRACT

The design techniques of the components on the macro level are established in the scientific community, however are far behind from the real material performance limits. To obtain those limits, the deeper understanding of the material structure is required. The methods of a new comonents production through standard alloying are the basis of the modern material science manufacturing. The design of the materials with expected required performance limits is the next conceptual step for the materials scientist. As results, to make this step, the problem of a precise material structure analyses on the microstructural level is one os the major importance for the next generation materials design. The complexity of the material structure across the scales(macro-micro) requires a new non deterministic methods for better understanding of the connectivity betwen a materials performance and material microstructure features. This work presents a various new research methodologies and techniques of the material microstructure characterization and numerical design with future applications to the anlyses of the material behavior. The focus of the particular research was to analyse a new cross correlation function of the material structure on the micro length scale and develop a novel framework which allows a better understanding of various important material phenomenas such as failure initiation and recrystallization.

ACKNOWLEDGMENTS

First of all I would like to thank my Father God for All.

Than,I would like to express my sincere gratitude to my advisor Prof. Kaan Inal for the great support of my Ph.D study and research, for his patience and trust. His guidance helped me in all the time of the research and make my life in Canada enjoyable.

My sincere thanks also goes to Dr. Abhijit Brahme, for leading my research for all three years of my work on thesis. Special thanks goes to Dr. Raja K. Mishra for his wise advises and comments. For sharing his invaluable bits of information in the field of the material science.

I would like to say great thank the people who where more than a family for me in Canada- Evdokia Popova, Oxana Skiba and Irina Yakunina. The people who support me and share all happiness and troubles. The people who never let me feel alone in a new country.

I would like to thank my dear University friends - Semen Mikheevsky, Sergei Bogdanov, Masha Bogdanova, Cris Nikols, Kirill Lyzo.

Thanks from the heart to my first teachers of math: Mikhail Volkov and Doctor Dmitri Bazylef, my first scientific advisor Doctor Melas Vyatcheslav.

Besides my advisor, I would like to thank the rest of my thesis committee: Prof. David Fullwood, Prof. Sean Peterson, Prof. Scott Walbridge and Professor Naveen Chandrashekar.

I thank my fellow labmates in University of Waterloo Computational Mechanics research group.

Last but not the least, I would like to thank my family - Anna Staraselski, Mikhail Staraselski, Doctor Yuri Staraselski, Igor Staraselski, Lubou Staraselski, Yakov Staraselski, Doctor Semen Staraselski, Ella Osipova, Klavdia Udasina, Solomon Udasin, Doctor Yulia Isachenko, Olga Letoha.

Dedication

This thesis is dedicated to All I love.

Contents

List of Tables

List of Figures

THESIS STRUCTURE

This thesis is based on the following publications from the permission of co-authors:

1. Chapter 2: Brahme, A., Staraselski, Y., Inal, K., Mishra, R. K. (2012). Determination of the Minimum Scan Size to Obtain Representative Textures by Electron Backscatter Diffraction. Metallurgical and Materials Transactions A, 43(13), 5298-5307.

2. Chapter 3: Staraselski, Y., Brahme, A., Inal, K., Mishra, R. K. (2012). Analytical estimation of distancedisorientation function of the material microstructure. Philosophical Magazin, 1-18.

3. Chapter 4: Staraselski, Y., Brahme, A., Inal, K., Mishra, R. K. (2013) Reconstruction of the 3D Representative volume element from the generalized 2-point correlation function. *International Journal of Plasticity*. (submitted for publication)

4. Chapter 5: Brahme, A., Staraselski, Y., Mishra, R. K, Inal, K., (2013) A new model to predict grain nucleation during dynamic recrystallization. *Mg2012: 9th International Conference on Magnesium Alloys and their Applications*

5. Chapter 5: Popova E., Staraselski, Y., Brahme, A., Mishra, R, K, Inal (2013) Crystal plasticity finite element model coupled with probabilistic cellular automata approach for modeling dynamic recrystallization in magnesium alloys *International Journal of Plasticity*. (accepted for publication)

6. Chapter 5: Staraselski, Y., Popova E., Brahme, A., Mishra, R, K. Inal (2013) The effect of the representative data on the modeling of dynamic recrystallization in magnesium alloys. *Scripta Materialia*. (preparing for submission)

7. Chapter 6: Staraselski, Y., Brahme, A., Mishra, R. , K. Inal, K., (2013) On the local metrics of the incompatibilities analyses with CPFEM. *International Journal of Plasticity*. (submitted for publication)

The following are the contributions by author publications (by Chapters):

Chapter 2: Development of the statistical theory and mathematical framework, numerical algorithms. Development of data mining algorithms.

Chapters 3, 4: Development of the theory and frameworks, numerical algorithms. Data analyses. Papers preparation and submission.

Chapter 5: Development of the physical model of nucleation in the recrystallization problem. Developing a methodology for the representative scan size analyses for the problem of the dynamic recrystallization.

Chapter 6 : Development of the mathematical theory and frameworks, numerical algorithms. Data analyses. Paper preparation and submission.

Chapter 1

General Introduction

Computational methods for material science and engineering can be key tools for advanced alloying and manufacturing processes. Exponential growth of the computational power is introducing new possibilities for numerical models and their applications. On the other hand, the development of the electron backscatter diffraction (EBSD) technique enabled researchers to implement microstructure characteristics such as grain morphology and crystallographic texture into their numerical models. Experimental EBSD maps have been directly employed in numerical models (i.e., finite element models) for modeling various phenomena such as formability, localized deformation, recrystallization. The field of microstructure design is growing rapidly although a standard is yet to be established. One of the first attempts in this field was presented by Adams et al. [2], where the design of a compliant beam to maximize the deflection without plastically deforming the beam was presented. Unfortunately, limited research exists in the field of materials design. [3, 4, 5, 6]. The main idea of the microstructure sensitive design (MSD) methodology consists of two separate parts. The first part [3] is the construction of the microstructure hull, which is a set of all possible 2microstructures used in the optimization. This space can be reduced by the several methodologies such as Fourier transformations, symmetry operators, different activities of the slip systems during the different load conditions, etc. For the construction of the material hull, Adams [2] developed a novel technique of material data characterization. The roots of this technique go back to the work of Bunge [7] in the fields of orientation distribution function analyses and spectral representations of the crystallographic texture.

The continiuos push for the development of engineered materials provides a challenging opportunity in the field of materials science for material characterization and design from the perspective of performance limits and property predictions. The problem of engineering materials at the level of microstructure is a relatively new and promising field. The major focus of the material microstructure optimization is to obtain the desired properties for enhanced material performance. In order to achieve this goal, the material behaviour should be accurately captured at different scales using various approaches/techniques. Optimization techniques are the tools to achieve a desirable objective property from all the possible sets of independent variables (input data). Accordingly, advanced theories in microstructure analyses should be applied in combination with the most efficient optimization techniques. It is well known that, through various processing techniques, it is possible to change both the macroscopic (yield stress, hardening rate, ductility, etc.) and microscopic (grain morphologies, texture, etc.) properties of materials of materials

[7, 8]. Thus, these material processing techniques create a potential bridge between the control and design of the material properties at micro and macro levels1.1). Allmost all modern constitutive models assume

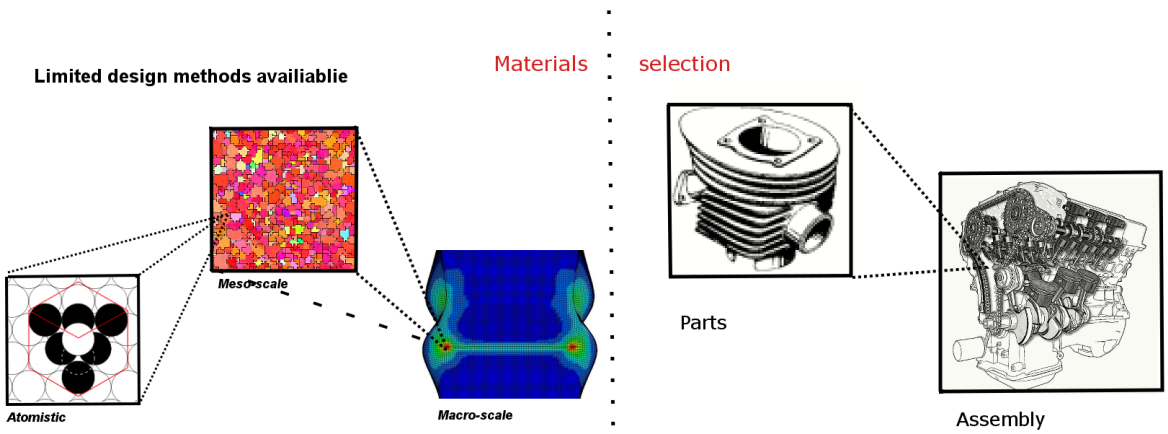

Figure 1.1: Material design across the scales diagram.

that the material deformation behavior depends on the crystal orientation through the resolved critical shear stress (Schmid law), considering the anisotropy of the single crystals. Other studies have shown that anisotropy and yield strength of a material depend not only on the texture, but also on the grain alignment and the number of precipitations in the material [9]. Bunge, in his classical work [7], pointed out a significant experimental observation, he classified face centered cubic (FCC) metal textures into two major classes: deformed and annealed textures. Thus observation makes a valuable scientific contribution, since it provides a connection between microstructural components and manufacturing processes. If one can predict the correlation between texture components with expected alloy properties, this classification can be used as an instruction for the possible solutions to obtain the desired texture components and then, to design the alloy.

1.1 Material Microstructure

Accurate understanding of the connection between the microscopic properties of the material and the macroscopic behavior of the material is a nontrivial physical problem. Numerical design or engineering of the microstructure is a problem of constrained optimization. These constraints can be described as the limitations on grain morphologies and the variation in texture that can be achieved through the processing of the material. Furthermore, microstructure optimization involves extensive computations and experimental measurements. The real material microstructure consists of various complex structural features (particles, inclusions, dispersed second faces, etc.). It should be mentioned that, the lower the considered scale of the microstructure, the more advanced physical model is required to obtain a relationship between the structure and its properties. In the material microstructures (which are hard to obtain precisely in 3D [10]) the different length-scales will predict different expected performance properties. This can be explained by the fact that the lower is the scale of the microstructure is considered the more general physical model is required to obtain a connectivity between a structure and properties. The amount of data that should

be collected for this type of material analyses is significant. For example, for a $1000 \times 1000 \mu m$ sample the amount of measured data points with an EBSD step of $2\mu m$ is 25×10^4 measurements, while going to nano scale requires at least 10^8 more measurements. This makes the data collection for microstructural analyses alone a complicated material research problem. To simplify this, the microstructure data obtained through microscope measurements should be subdivided or clustered by specific phases or states of the full media (for example grains). However, even these clusters of material perform on a high level of uncertainty and complexity. The grain morphology as well as the texture is not randomly distributed and, therefore, not homogenous, which makes the problem of the prediction of the material properties even more complicated. For example, the grain size in a given material has a lognormal distribution. The orientation of the grains are also anisotropic and this anisotropy is reflected in the preferred crystallographic orientation, i.e textures. The term *microstructure* in a particular work is referred to as a combination of the preferred material crystallography states (*texture*) and the arrangement of these states, so-called grains and their geometry (see Fig. 1.2). The color map presented in Fig. 1.2 shows the specific material

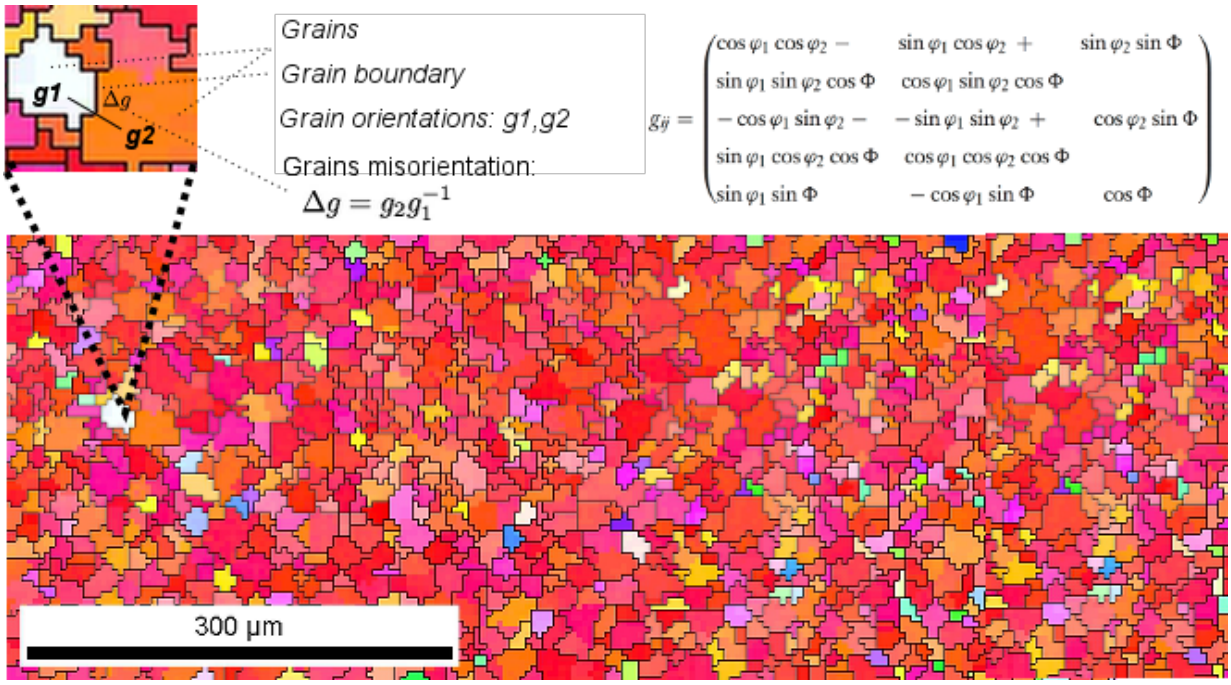

Figure 1.2: General representation of the 2D EBSD microstructure map.

cluster phase or so-called grain. The grains are separated by the boundaries, which are assigned based on misorientation between neighboring pixels. Each color on the map corresponds to an orientation of the measured pixel and is assigned to a pixels data set with some level of confidence or tolerance. There are various ways to mathematically represent the orientation space of the texture of a microstructure. One of the most common approach is assigning an Euler angle triplet (rotation around particular axes) to each pixel g$(\phi 1, \Phi, \phi 2)$. There are lots of different representations of the Euler angles which are reducible at the point of definition of rotation axes. To describe the orientation of a particular grain, the orientation space is provided with a function(g) presenting a mismatch in a rotation space between two orientations of the

arbitrary points. The most common separation metric in an orientation space of grains is the misorientation concept (see Fig. 1.2). However, knowing the misorientation between grains is not usually enough to identify the basis representation of the texture. This is explained by the symmetry of the crystallographical space of the material (as can be seen from Fig. 1.2 the orientation and misorientation are matrices). Next, the disorientation between grains should be calculated to reduce the effect of the symmetry (O) on the representation of the grains orientations. The disorientation, θ, represents a unique misorientation of the specific grain or unit inside the grain according to the minimum possible angle transformation:

$$min\{cos^{-1}(\frac{trace(O^{(i)}g_B g_A^{-1} O^{(j)} - 1)}{2}), cos^{-1}(\frac{trace(O^{(k)}g_A g_B^{-1} O^{(l)} - 1)}{2})\}, \{i, j, k, l = 1, n\} \quad (1.1)$$

where n is a set of all possible symmetric transformation defined for each operator O and A,B are different states or grains(for more detailes see [11]). An EBSD map contains a large amount of relative information about the material at the grain scale; i.e., grain sizes, grain distributions, grain orientations. Furthermore, varios cross correlations and statistical functions, can be be constructed on this data. Furthermore, varios cross correlations and statistical functions which could be constructed on this data as will be discussed further in Sec. 1.2.

Following Fullwood et al. [12] one of the major problems of microstructure design could be quickly divided numerically into separate research categories. A design problem should be identified with a set of the optimized target material properties and criteria. Material properties are dependent on the required performance of the material (energy absorption, failure, etc). Optimization criteria must include observed (dependent) and arbitrary (independent) variables of the design. For dependent variables (observed) one can choose certain material properties and microstructural components(texture distribution, grain size and shape, etc.) as independent variables. Material microstructure should be identified at a certain level and scale (nano(A), micro(0.1μ), meso(μm) or macro(m)) since homogenization length scale should be selected for the optimization criteria. A representative material scan size **(RSS)** should be obtained as an accurate input of the model and should be consistent with the optimization scheme. RSS can than be used as an etalon microstructure for the designed representative volume element **(RVE)** and should be identified as a building block for the design space. Valid microstructural norms should be studied and optimized for the problem of RSS-RVE construction (orientation functions, 2-point correlation functions). Design optimization space should be obtained based on the material RVE. Note, that the design space is a space representative of all the possible independent variables (microstructures) of the design. The optimization design space is usually called a microstructure hull. The next step is to find the limits of the design problem based on the material of interest. A limited set of design properties or property closures should be associated with the proper norms defined in the optimization space as well as techniques for the construction of the property closures (optimization algorithms). Each topic mentioned above is a separate material characterization, design and theoretical problem.

1.2 Microstructure characterization

The analysis of the crystallographic orientation space is usually associated with a large amount of data as well as significant complexity caused by grain morphologies. Analysis of the data collected by Scanning Electron Microscopy (SEM) or EBSD is generally problematic due to the large amount of information. Precise data analysis of the microstructure in a sense of data mining can provide more information about

data dependencies in the material and can assist in the development of material models with precise microstructural information for engineering applications. EBSD data is a perfect candidate for the microstructure data research because of the amount of information it contains. To address this complicated problem, correlation functions have been employed to characterize complex heterogeneous media. Historically, the correlation functions in solid state physics were implied in the work by Cosserat [13]. This work presented a description of the stress with micro rotations, which introduces the length scale effects in classical elasticity. In the discussion of the correlation functions, it is important to mention the work of Beran and McCoy [14], where the authors presented strain gradient analysis of random media showing the effects of fluctuations in the constants of elasticity on the force field in a statistically homogeneous medium. The authors presented the dependence of the solution on the length (a distance from the point of the field to the applied force) introduced in the gradient theory. Considerable amount of research was performed in the field of application of the n-point correlation statistics to the problems of three-dimensional microstructure reconstructions [15, 16, 17, 18, 19, 20, 21, 22, 23]. A variety of research methodologies were proposed in these works, namely, Monte-Carlo stochastic optimization, simulated annealing, Fourier space analysis, etc. In this approach, the main idea is to reconstruct the full microstructure medium from the n-point correlation statistics using different optimization and homogenization techniques. The correlation between particle interactions and the length scale effect were investigated by Glicksman et al. [24] and Wang et al. [25, 26] where studies of spatial and nearest-neighbor correlations in the polydispersed particle systems were presented.

Recently, Jiao et al.[27] demonstrated the application of n-point correlation, S_n, and in particular, S_2 (two point correlation) to various practical problems including microstructural analysis for the real engineering materials, while Neizgoda et al. and Qidwai et al. [28, 29] in their recent works have shown the application of the 2-point statistics to the analysis of the representative volume element(RVE). They highlighted the importance of the analytical estimators of the 2-point correlation statistics (see Fig. 1.3) found for the real microstructure. Also, the gap in the field of obtaining a universal solution for the statistical descriptors was discussed. It should be mentioned that, statistical analysis of the two-point correlation function was initially proposed by Corson [30], who used the exponential model ($\mathbf{P_{ij}} = \alpha_{\mathbf{ij}} + \beta_{\mathbf{ij}} \exp(-\mathbf{c_{ij}}\mathbf{R}^{\mathbf{n_{ij}}})$), where P_{ij} is the two-point correlation function, R is the distance vector separating the two phases i and j, and α, β, c and n are the coefficients obtained by curve fitting to the experimental data of interest. However, the obtained coefficients have no physical meaning and have to be evaluated for different material data sets. A significant work in the analytical approximation of n-point correlation statistics was performed by Torquato et al. [31, 32]. As pointed out by Sundararaghavan and Kumar[33], there is no connection between microstructure related parameters and those, estimated from the correlation analysis of a given microstructure. Garmestani et al.[34] presented an analytical approximation, which takes into account the volume fractions V_j of grains with specific discrete set of orientations g:

$$P(g_j|(g_i, R)) = V_j + (1 - V_j \exp(-c_{ij} R^{n_{ij}})) \tag{1.2}$$

The parameters presented in their work are the same curve fitting parameters of initial conditional orientation correlation function (COCF)[30]. This solution improves the fitting procedure but still is a global approximation, and hence, is not applicable to the real material modeling problems and solutions. An experimental work to obtain the precise microstructural correlation distribution function descriptor was presented by Tewari et al.[35]. In this work, they highlighted the complexity of obtaining the two-point correlation descriptor for measured EBSD data sample and proposed a procedure that can improve the computational time. They concluded that the observer needs, as a minimum, the 10^{13} measurements of the Cartesian distances for a $500 \times 500 \mu m$ material sample. The proposed procedure was based on

the usage of the dynamic lookup tables (**LUTs**) for computing distances and angles. Two-point correlation function was also used for probabilistic modeling of microstructure evolution using Finite Element Modeling (FEM) in the work of Sundararaghavan et al.[33]. The authors showed the applicability of the conditional orientation correlation function (**COCF**), defined as the probability density of occurrence of a crystal orientation g' at a distance r from a given orientation g, to their FEM model. A Lagrangian approach was used to obtain the normalization constraints. However, the major problem with the analysis based on FEM probabilistic modeling of the microstructure evolution is the computational complexity of obtaining the COCF for each numerical integration point in the model. The analytical study of the two point correlation function based on the so-called texture functions in the Fourier space approximations can be found in the works of Adams et al.[36]. The Fourier space solutions are neither problem specific nor flexible to the real changes in the material specific microstructures [33]. The analytical solutions for the cross-correlation texture functions can be employed in a large variety of applications (see Fullwood et al.[12]), such as long range ordering of texture, two point correlation function construction, representative scan size (RSS), microstructure based finite element method (FEM) modeling, micro-polar elasticity, etc.

This thesis will present a new theoretical model to determine a functional form for the distance-disorientation distribution (DDF) (Fig. 1.3). The DDF can be treated as a generalized two-point correlation function. To obtain the DDF, one needs information on both the distance between any two given pair of points in the microstructure and the disorientation between them is necessary. However, this cal-

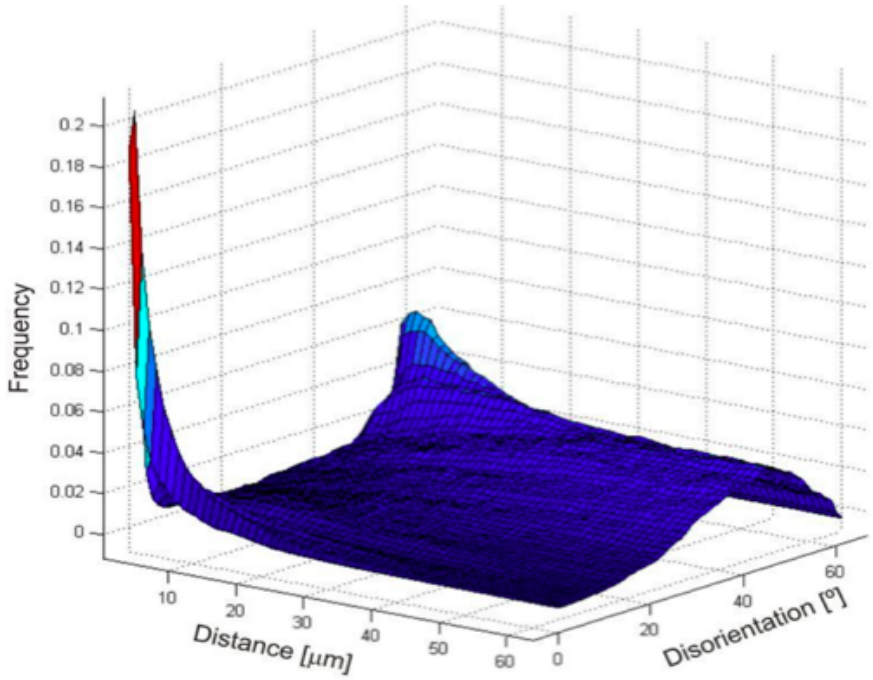

Figure 1.3: 3D representation of the distance-disorientation cross correlation function

culation, or any calculation of a two-point correlation function, is very time consuming. To address this problem, this research proposes to calculate the DDF in two parts. First, one must obtain an analytical

solution for the geometrical domain (grain morphology and grain distribution) and then combine it with the crystallographic domain (grain orientation) to aid efficient quantification of the microstructure for implementation in engineering analyses of material behavior. After the analytical solution of the DDF function is obtained, its application will be introduced to the problem of the representative volume element construction. The next sections will give a brief overview on the problem of the reconstruction methods widely used in the microstructure design.

1.3 Microstructure reconstruction

Unfortunately, a clear definition, so far, for the RVE in the scientific community [12] does not exist. The main concept of RVE is to provide the statistically representative domain of the whole media, which can be representative in the terms of its properties. The latest concepts of the statistical representation were formulated in the work of Neizgoda et al.[28] and Qidwai et al.[29]. The statistically representative element in the authors' formulation is an element, which can be randomly cropped from the material sample and represent certain properties (for example stress-strain response). This formulation is widely used, although it is not necessarily enough for defining the RVE. Furthermore, this definition is weak in terms of capturing localization effects of the material microstructure. It should be mentioned that Shan and Gokhale [40] also studied the distance disorientation function (DDF) for the nearest neighbors to construct a microstructural representative volume element (RVE) (1.4).

The problem of the reconstruction of 3D microstructures from stereographically projected EBSD data is one of the most difficult ones and, unfortunately, it has not yet been studied in depth. The novel concept of RVE, presented in this thesis, proposes to treat RVE as a representative of the material (in our case microstructure), and mechanical response is only a part of the problem of the material representation. This concept will be introduced in the Chap.4.3.3. Furthermore, the proposed work presents a technique for the construction of such synthetic RVEs in a 3D space. There is significant motivation to get a 3D representation of the data observed from a microscope. It is obvious that material characterization and its anisotropic behavior has to be three dimensional by its nature. Reducing the space of the material data leads to the loss of the existing correlations. The first important question is to determine which characteristics can be obtained from the 2D EBSD data, and how they could be quantified. In-depth study of the EBSD data can be found in the works of Humphreys et al.[41], where the author described, in detail, the qualitative characteristics of the data that is obtained from a microscope. He describes such characteristics of material as nearest neighbors grain orientations, average volume fraction of the grain, texture and its correlation with grain or sub-grain size, the spatial distribution of stored energy in a sample and the amount of recrystallized grain in the material sample. The work of Humpryes et al. [41] was systematized later on by Groebert et al. [42]. Groebert gave a list of the main material characteristics, obtained from the EBSD, in the well-defined list of statistical descriptors measured during the analyses of the material. Moreover, his work presented the general framework of the synthetic microstructure builder, based on this descriptors, which is commonly used nowadays. The initial work was proposed by Rollet and is discussed in his papers [43, 11, 10]. While the global approach can slightly vary, it can still be divided into three main categories as follows:

1. Generation of the distribution of the initial grains: Create grain distributions within the microstructure with realistic prediction of grain shapes, sizes and location in the microstructure.

2. Distribution of the grains inside the material microstructure: Construct grain distribution and their neighborhood, which are similar to the real material grain structure.

3. Crystallographic orientation assignment: Assignment of the orientations for the grains, which will minimize the gap between local neighboring misorientation distribution function (MDF) and the global orientation distribution function(ODF)

The above described framework is the most widely employed tool for the material 3D representation. Over the past years, significant research was performed in the field of the microstructure reconstruction from the correlation functions [15, 16, 17, 20, 21, 22]. The main idea is to reconstruct the full microstructure media, from the n-point (2-point) correlation statistics using different optimization and homogenization techniques. The proposed method is a new technique, which combines the reconstruction of the RVE using the simulated annealing method with the new solution of the 2-point correlation statistic reconstruction in the 3D microstructure. Note that the method of serial sectioning (SS method) [44] is another approach of the generation of the material microstructures. However, this method is not applicable so far due to its high computational cost, and the obtaining the final dimensions of the 3D sample is time consuming. Another weak point of this method is the non-parametric solution, which the SS method provides due to the fact that it calculates a new 3D microstructure by stitching the parts of different EBSD sections and cannot be recognized as a numerical tool. Discussed 3D microstructure generation techniques will be used in the presented work as the basis for the future improvement and construction of the new 3D microstructure. This microstructure will be able to account not only for already existing measurements obtained from the EBSD, but also a new cross-correlation proposed in this research.

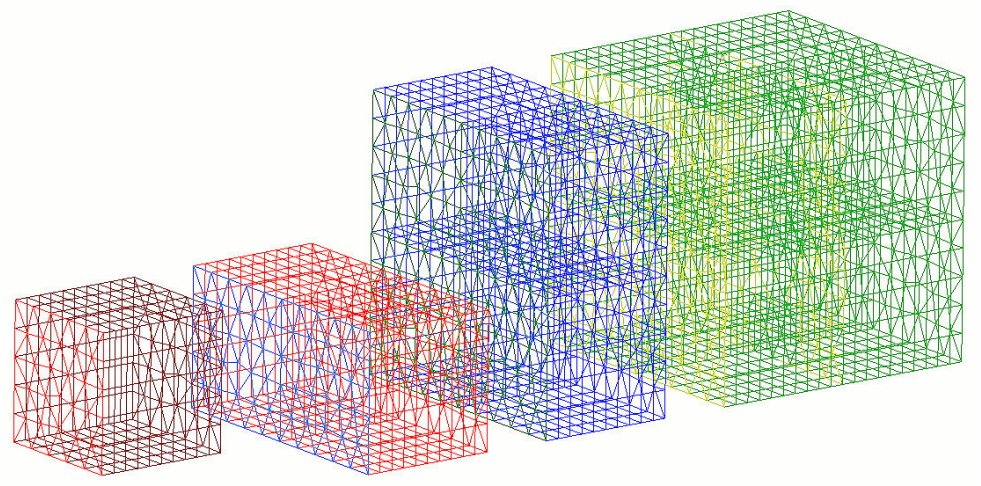

Figure 1.4: General representation of the concept of the representative volume element reconstruction

1.4 Objetives of the research

The proposed research work will investigate only part of the microstructure design problem due to its complexity. The general scope of this research is illustrated in the Fig. 1.6. The first block represents the statistical characterization techniques and new functions, which were developed and implemented in the numerical framework. One of the major problems that the research presented in this thesis addresses on the characterization level is: (i) how much data should experimentalists consider while extracting the EBSD data on the meso scale(μm) and, (ii) what methodology can be applied for that particular problem. Once the above are addressed, a new question arises; how can this knowledge about representative material and long range microstructural correlation be used further for the material design and characterization. For example, if you have a crop of the abstract measured data (black window), what are the minimal limits of the sub-crop (red window) required for the data being representative of the whole media (1.5)? It should be mentioned that the research presented in this thesis will not include the construction of the

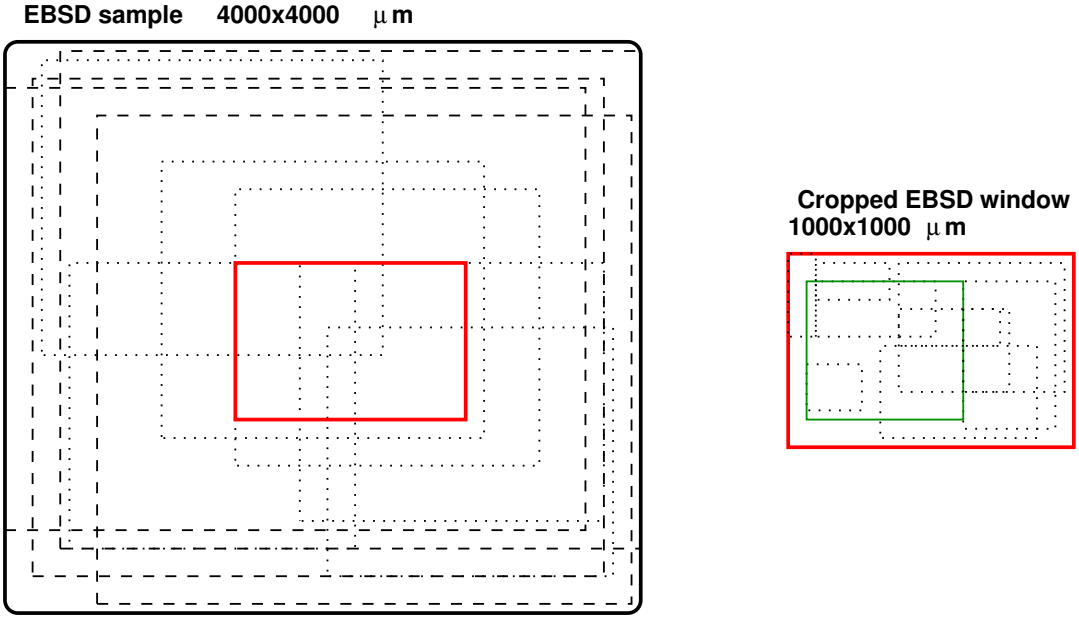

Figure 1.5: General representation of the RSS concept procedure.

optimal microstructure hull and material properties closure, leaving it for future work. Accordingly, the study presented could be divided into two major research topics:

1. *Microstructure characterization*
   (a) How much material needs to be obtained to be representative for further micro-macro mechanical analyses?
   (b) Does the processing of the material effect the representative dimensions?
   (c) Are the existing material analyses techniques is enough for material comparative analyses and characterization?

(d) How many grain representations in 3D are required for them to be representative ?

(e) Two examples of microstructure sensitive analyses; failure and recrystallization

2. *Microstructure reconstruction and numerical optimization*

(a) Integration of the microstructure characterization techniques with existing material-behavior computational methods

(b) Creation of a precise material microstructure reconstruction in 3D with the new DDF term

(c) Implementation and improvement of the existing material reconstruction optimization schemas

(d) Comparative analyses between different 3D material microstructures for understanding of the various material phenomenon

After the development of novel microstructure characterization techniques, the next part of the research corresponds to the numerical modeling procedures. The new methods of correlation functions analyses will be discussed with some applications. This part of the work will create the mathematical basis for the next layer of the research -microstructure reconstruction.

In this thesis, first, a new mathematical framework and a quantitative measure for obtaining the representative scan size will be presented. The framework for obtaining the representative scan is based on the DDF function and its analysis using information theory norms. A new functional form of DDF statistics is inherited from the ideas of the population model construction. Next, the parameters for the analytical solution (logistic distribution curve), which is based on the microstructure morphology, will be estimated. Instead of the evaluating the exact DDF correlation statistics, the proposed method treats disorientation as a known fixed parameter (measured from the crystallographic Euler space of the microstructure), and then, estimates the distance function. The application of the constructed DDF solution based on the grain morphology is applied to the large EBSD scans of Aluminum and Magnesium samples, and the results are compared with measured DDF data to validate a new model. After the analytical solution is obtained, the next chapters will present the application of the new solution to the problem of the 3D microstructure reconstruction. Different microstructures, obtained from the new 3D microstructure building procedure, will be used as a tool to investigate the effects of the representative texture on localization phenomena. The last chapter of this thesis investigates the techniques of studying incompatibilities, rather than attempting to explain and validate the results with experiments. The incompatibilities are carefully defined through the extreme value statistics problem. Different aspects such as grain boundaries analysis, triaxiality tensor analysis, the effects of the microstructure sampling on the results of the failure initiation, incompatibilities are discussed.

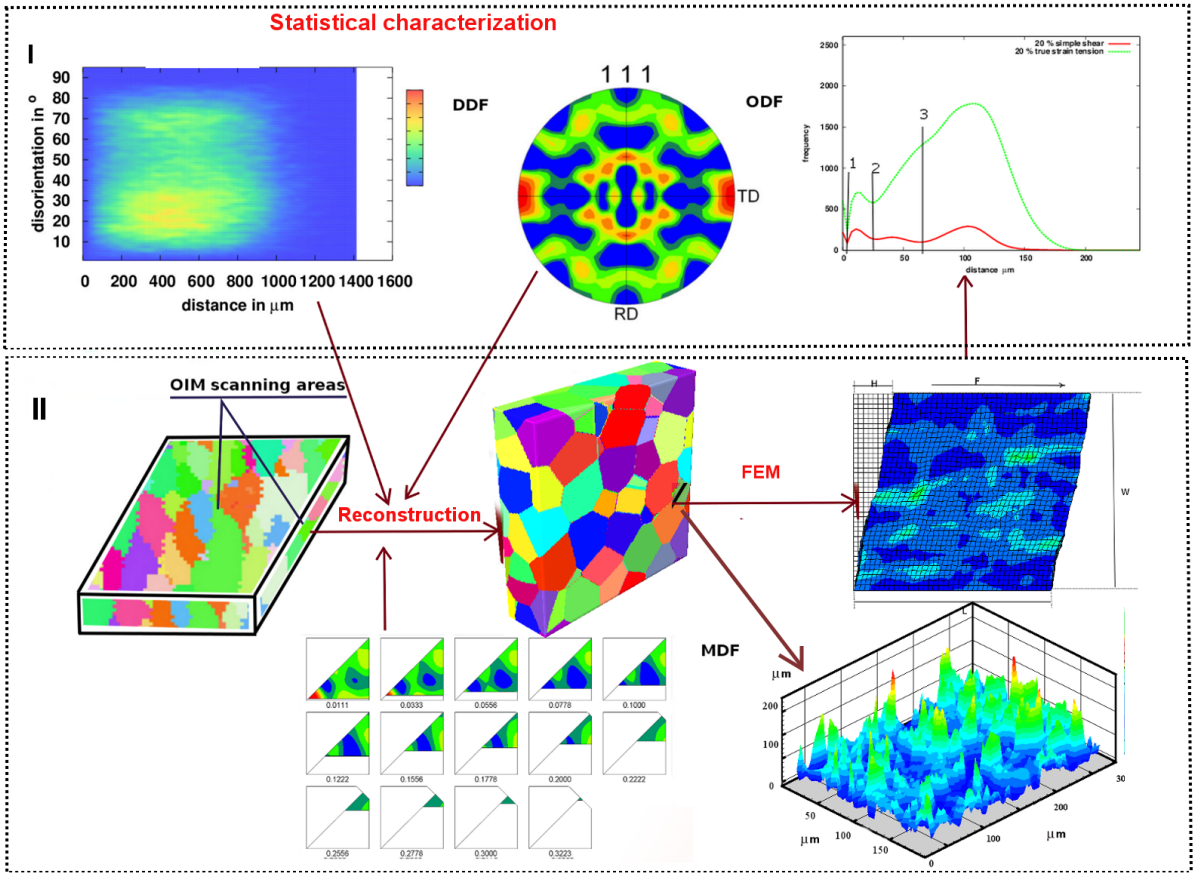

Figure 1.6: General representation of the microstructure design process.

Chapter 2

On the Determination of the Minimum Scan Size to Obtain Representative Textures by Electron Backscatter Diffraction

A new method for analyzing microstructure is proposed to evaluate the long range dependence of texture. The proposed method calculates the average disorientation as a function of distance between data points as measured by electron backscatter diffraction patterns. This method gives a measure of clustering of texture and is used to accurately evaluate the effective grain size. This procedure in conjunction with Information theory is used to estimate a representative scan size for various materials. Analyses show that the optimal scan size depends on grain morphology and crystallographic texture. The results also indicate that on an average the optimal scan size needs to be ar least 10 times the effective grain size in each direction in length.

2.1 Introduction

Since the introduction of **E**lectron **B**acks**c**atter **D**iffraction (EBSD) patterns four decades ago [45] they have been used increasingly in materials characterization. Adams and coworkers [46][47] proposed a fast automated indexing of the EBSD patterns (based on Hough transforms) and increased the data collection speed. Today EBSD has become an indispensable tool for quantifying microstructure related parameters like grain morphology, crystallographic texture etc. The increased speed for data acquisition and processing has led to the ability to gather and analyze enormous amount of data in record time. The technique has a wide variety of uses spanning over several length scales with step sizes (distance between two observation points on the scan surface) ranging from few nano-meters [48] to many micrometers. Experimental data obtained from EBSD has been used in modeling material behavior. Experimentally measured EBSD maps have been directly employed for modeling recrystallization (3D Monte-Carlo based models [49][50], Cellular

Automaton based models [51]) as well as deformation using Finite Element Analysis [52][53][54][55] and Fast Fourier Transforms [56] to name a few.

The resolution at which the data is obtained from the EBSD measurements and the size of the scan area are determined by the problem at hand. Despite the amount of recent work in the field when it comes to determining the scan size, Optimal Design of Experiment (ODE) ([57, see]) is lacking. An ideal scan should contain all the relevant information like grain size, shape and size distribution, micro as well as macro texture. Schuh et al. [58], for example, while studying grain boundary networks observed that the measured mass distribution of grain boundary clusters depended on the size of EBSD scan. A small scan can be obtained at very high resolution but might not be representative of the macro-texture and grain size/shape distribution. A large high resolution scan on the other hand will contain all the relevant information but can be wasteful. The goal is to obtain a scan which is representative but is not too large. Humphreys [59] in his work on quantitative metallography with EBSD gave an estimation on the amount of data points needed in an EBSD scan for various problems of interest based on speed of data acquisition and angular and spatial resolution. Wright et al. [60] showed that to have a truly representative texture, comparable to X-ray diffraction measurements then one needs observations from 1000 to 10,000 grains. While Baudin [61] concluded one needs about 1000 orientations for the EBSD texture measurements to be representative. For phase fraction determination in multiphase materials, Davut and Zaefferer [62] showed that to obtain representative measurements one needs to scan at-least 0.275 mm^2 with 30,000 points. When the EBSD data is employed as an input to numerical models for deformation and annealing studies, selecting data which is representative of the bulk material (representative volume element - RVE) is of prime importance. In this case using an ODE for obtaining the EBSD is essential. For example in extruded AZ31 samples the crystallographic texture is strong with most normals having basal texture as can be seen in Fig. 2.1. The scan size which would be representative of the bulk would be smaller than a sample which has a weaker texture.

Plastic deformation of materials is generally accompanied by crystallographic rotation. The rotation of one grain has to be correlated to the rotation of its immediate neighbors. The rotation of the neighbors is in turn tied with the rotation of their neighbors and so on. One has to then go a certain distance from the first grain so that its influence is not felt. This should lead to some sort of a clustering. In the context of this work *clustering* means an ordered distribution (in a Cartesian distance space) of crystallographic orientation in each grain beyond the nearest neighbors. The amount of such clusters will effectively determine the amount of area that needs to be scanned to be sure that the data collected by EBSD is representative to study plastic deformation. For example, as a first approximation, if the cluster size is 5 grains then the EBSD scan should be bigger by a factor greater than 5 times grain radius. One of the aims of this work is to identify if such a "typical" cluster (orientation cluster) size exists. If it does then how can it be quantified.

One of the reasons ODE is not used for EBSD acquisition is the nonexistence of a framework to evaluate the optimization. The objective of this work is to establish such a framework and obtain an optimal scan size. This will be done by recasting the problem in terms of information theory (details are discussed in Sec. 2.5).

The main aim of the work presented here is to outline a procedure to obtain a representative scan size such that it can be applicable to a wide variety of materials. For this purpose in Section 6.2 the experimental data used in this analysis is presented. The statistic used to obtain the representative scan size, as a correlation between the distance and disorientation, is described in Section 3.5 and is applied to the materials presented in Section 6.2. The preliminary results and a qualitative measure to obtain the

representative scan size are given in Section 2.4. The mathematical framework and a quantitative measure for obtaining the representative scan size are presented in Section 2.5. The results and analysis obtained from using the above on the experimental data are presented in Sections 2.4 and 2.6 respectively.

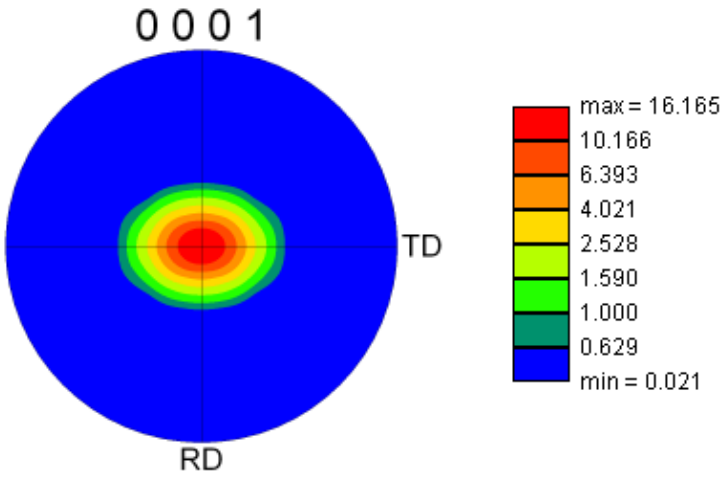

Figure 2.1: 0001 Pole figure of extruded AZ31 sample showing strong basal texture, highest intensity being 16 times random.

2.2 Experimental data

In Table 2.1 experimental data used in the analysis is presented. The experimental data is for FCC and HCP materials for various loading conditions. For FCC materials two different AA5754 aluminum sheet samples (direct chill-cast and continuous cast, referred to as DC and CC sheets respectively) are considered. For HCP materials the data from extruded samples of pure Magnesium, Mg+0.5%Ce and AZ31 are chosen. The data sets encompass a wide range of grain sizes from $\sim 14\mu m$ (AZ31) to $\sim 50\mu m$ (pure Mg). The texture strength[1] also shows a wide range from 1.775 for CC sheets to 16.16 for AZ31. This allows one the opportunity to determine the effects of both grain size and texture strength on the representative scan size. The EBSD scans for all the samples were obtained using LEO 1450 scanning electron microscope (SEM) fitted with a TSL EBSD camera. The scan size selected was $1000 \times 1000\ \mu m$, apart from AA5754 samples and AZ31 where the scan size was $2000 \times 2000\ \mu m$. The maximum step size, in the case of Mg+0.5%Ce, of 4.0 μm giving the minimum scan data with $>$ 70000 data points. This is higher than the 20000 data points recommended by Humphreys [59].

The EBSD data was analyzed using the TSL^{TM}OIM software (Ver. 4.6). The data was cleaned to remove the bad data points and only data points having a confidence index (CI) above 0.2 were retained for the analysis. Cleanup was performed using the TSL **Grain Dilation** feature by setting the *grain tolerance angle* to 5° and the *minimum grain size* to 10 data pixels. Also TSL **Neighbour CI Correlation** with *minimum confidence index* set to 0.2 was employed to remove bad data points. Grains were identified

[1]defined here as the maximum intensity in pole figures

with a misorientation tolerance of 10°, using the TSL **Single Orientation per Grain** set to 10°. That is all the pixels having a misorientation of less than 10° were grouped together and identified as a grain. For the analysis, grains with less than 10 data points were excluded. Once grains were identified all the pixels in the grain were assigned average orientation of the grain. As a result, the misorientation of any two pixels within a grain is zero. The number of grains in the scans varied from ∼500 for pure Magnesium samples to ∼8500 for DC sheet sample.

Table 2.1: Experimental data.

Material		Grain size (μm) using intercept method		Texture strength	EBSD scan size (μm)	
Type	Condition	X	Y		along X	along Y
AA5754	CC	24.77	25.52	1.775	2000	2000
AA5754	DC	21.38	23.94	3.4	2000	2000
Pure Magnesium	Tension 0%	45.46	48.67	5.84	1000	1000
	Tension 10%	36.30	37.91	5.892	1000	1000
	Compression 0%	43.17	48.02	5.411	1000	1000
	Compression 20%	32.09	41.48	9.088	1000	1000
Mg+0.5%Ce	Compression 0%	20.96	22.78	3.347	1000	1000
	Compression 27%	15.88	17.49	5.078	1000	1000
AZ31	extruded	14.59	14.34	16.16	2000	2000

2.3 Distance-disorientation function

Each of the EBSD scans contains a lot of information in it including, but not limited to, overall texture, grain boundary misorientation, amount and orientation of twins etc. The data can also be further analyzed to give an indication of the amount of stored energy, lattice strain etc. Each of the subsequent analysis presented in this work focuses on a particular aspect of the data while ignoring other aspects. The purpose of this work is to determine the representative scan size (**RSS**) for that aspect of the data. The term representative is used to signify a scan size that gives full texture information (not just the micro/macro texture, but also long range ordering) for the given material, which can be used for future analyses and processing. With this aim we will present a method to analyze the EBSD data. The input to this method is the EBSD data set and the output is a *statistic* that will be later used in conjunction with information theory to give the desired RSS. We will call this statistic the distance-disorientation function of texture (**DDF** for short).

Distance-disorientation function (DDF) gives complete description of distance between any two points in the EBSD scan and the average disorientation between them. It gives the average disorientation (m_d) for all pairs of pixels separated by a distance d. This definition goes beyond the misorientation distribution

function (MDF) [7] and the misorientation correlation function (MCF) as defined by Beausir et al. [63]. The MDF considers only nearest neighboring pixels in the analysis. The MCF proposed by Beausir et al. gives the probability density for occurrence of a certain misorientation between pairs of grains at a certain distance. Beausir et al. limited their analysis to nearest neighbors and hence the analysis is not suited to obtain "true" distance-disorientation function. It is similar to the orientation correlation function (OCF) as proposed by Adams et al. [64]. OCF is defined as the joint probability of orientation g occurring at a point P and orientation g' occurring at point P' such that P and P' are separated by a vector $\mathbf{r}$. The major difference is that DDF definition ignores the specific orientation g and g' and calculates the distance-disorientation correlation without directional dependency. Barton and Dawson [65] defined an *intra-granular* misorientation tensor by taking the dyadic product of misorientation between two points and the vector joining them. It is important to mention, that just the disorientation angle alone is not sufficient to characterize the complexity of the space. However, a quantitative measure of comparison requires the definition a proper norm. For example, even if the method presented by Barton and Dawson (using dyadic product would give matrix space) is employed, there is still a need for a proper norm on the complex matrix space. It should be highlighted that the definition of the distance-disorientation is a definition of the cross norm [66]. This approach is adopted from functional analyses and is the meaningful approach to deal with the complexity of the full crystallographic space. In this research work, the cross norm $\|r\|\|\Omega\|$ of the tensor product $r \otimes \Omega$ is employed . In this approach, r is the vector connecting two points in the microstructure and is the misorientation. For $\|r\|$ we use the L_2 norm, i.e $\|r\| = d$, the distance, and for $\|\Omega\|$ we use the disorientation angle [67]. The method of obtaining the crystallographic description of grain boundary orientations from the Euler space (phi1, Phi, phi2) to the axis-angle representation is well known and could be found, for example, in the early works of Heinz and Neumann [67]. This approach is based on finding the minimum rotation angle between two lattices with the misorientation axis located in the standard stereographic triangle (accordingly to the specific symmetry group).

Vorhauer et al. [68] have presented a similar analysis by analyzing the disorientation as a function of distance within a ring, determined arbitrarily. Their work used the maximum ring size of $\sim 5\mu m$, which is smaller than their average grain size of $\sim 250\mu m$. The procedure adopted in this work to obtain DDF is depicted in Fig. 2.2. A distance d_1 is chosen such that $d_1 < d_{max}$, where d_{max} is the maximum distance between the two pixels in the scan. The average disorientation between all pairs of pixels having a distance d_1 is calculated. A new length d_2 is picked and this procedure is repeated for all possible distances. Thus $m(d)$, the average disorientation between two pixels at a distance d, is given by:

$$m(d) = \frac{\sum_i^{\text{all pairs}} (\theta_i)}{N_l} \tag{2.1}$$

where, N_l is the number of pairs at distance d and θ_i is the disorientation of the i^{th} pair. The procedure used in this work uses an alternate method to arrive at the same DDF.

First step in calculating the DDF is to obtain a joint distribution function correlating the distance between a pair of pixels in the scan and the disorientation $N(d, \theta)$ given by:

$$N_{ij} = \text{ number of pairs having a distance } d_i \text{ and disorientation } \theta_j \tag{2.2}$$

An example of such a distribution is shown in Fig. 2.3[2]. Once a joint distribution is calculated the DDF

[2]the details in this are fascinating but will not be discussed here to avoid diversion from the main thrust of this work

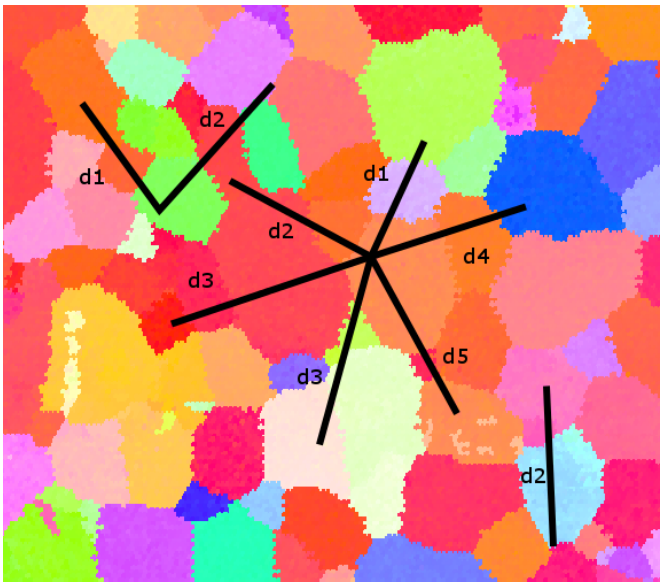

Figure 2.2: Obtaining long-range ordering using EBSD maps.

is obtained by averaging the disorientation for each distance. The DDF $m(d)$ is then given by:

$$m_i = \frac{\sum_j N_{ij}\theta_j}{\sum_j N_{ij}} \tag{2.3}$$

2.4 Preliminary results

Figure 2.4 shows the result of using the above procedure on the EBSD data obtained from the pure Magnesium sample with 0% tension. The DDF can be divided onto three parts:

1. The initial steep part for distances smaller than the effective grain size. The slope of this part is high; even though most sampling pairs are within the same grain, as the distance between sampling pairs increases the number fraction of pairs that are in different grains increases rapidly.

2. The tail for higher values of distance. This tail shows the effect of sampling pairs in opposite corners of the scan area and hence can be specific to the area where the scan is obtained from and may not be material specific.

3. The intermediate part. This part shows clustering of orientations, if any exists. If the texture distribution is random then the DDF curve will be very noisy and two DDF curves from scans with same dimensions will not be identical. This is the part of the DDF curve used to determine the RSS as it stores the inter-granular ordering information. The RSS is obtained by minimizing the information mismatch between an ideal (or full) scan and a scan with RSS.

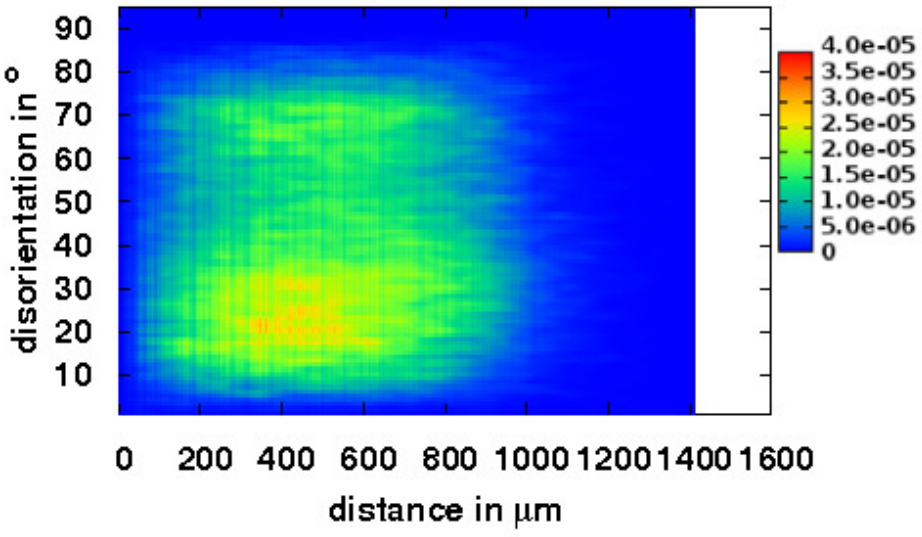

Figure 2.3: Distribution of distance and disorientation between any two pixels (EBSD data points). The color is indicative of the number of such pixel pairs having the same distance and same disorientation.

The point on the curve where there is a transition from the steep initial slope can be used as an indicator of the effective grain size (diameter). To obtain the grain size, the slope of the DDF curve is calculated at each point. The distance for which the slope of the DDF curve first approaches to its minimum value is taken as the effective grain size. This particular curve gives the grain diameter of the pure Mg sample of ∼120 which is approximately the grain diameter by the intercept method which according to Table 2.1[3] is ∼100. The effect of corners of the scan are felt when the $dim_{min} < d < d_{diag}$ where, dim_{min} is the minimum dimension of the scan (or sub-scan) and d_{diag} is the diagonal distance of the scan. As the distance between pixels increases beyond dim_{min} the number of pairs drops exponentially as a result the calculated average is susceptible to the local texture. As an extreme case for $d = d_{diag}$ there are two pairs of pixels with this distance, one pair at each corner and its opposite corner. Thus the average disorientation for this distance is the average of two numbers and hence can be different in different scans (or sub-scans). This does not imply that these pixels in the corner are completely ignored. As they are part of a lot of pairs with distance less than dim_{min} in the local neighborhood. In the intermediate part the curve shows first a slight positive slope with a maximum at around $500\mu m$ and then a small negative slope.

Figure 2.5 shows the DDF for some of the materials listed in Table 2.1 with particular emphasis on the region near the transition. The inset shows the entire DDF excluding the tail. Comparison between the transition points and the grain sizes from Table 2.1 shows a good correlation between the grain sizes from DDF and the ones calculated using intercept method. The DDF of a small cropped portion of the entire

[3]grain size reported in Tab. 2.1 is grain radius.

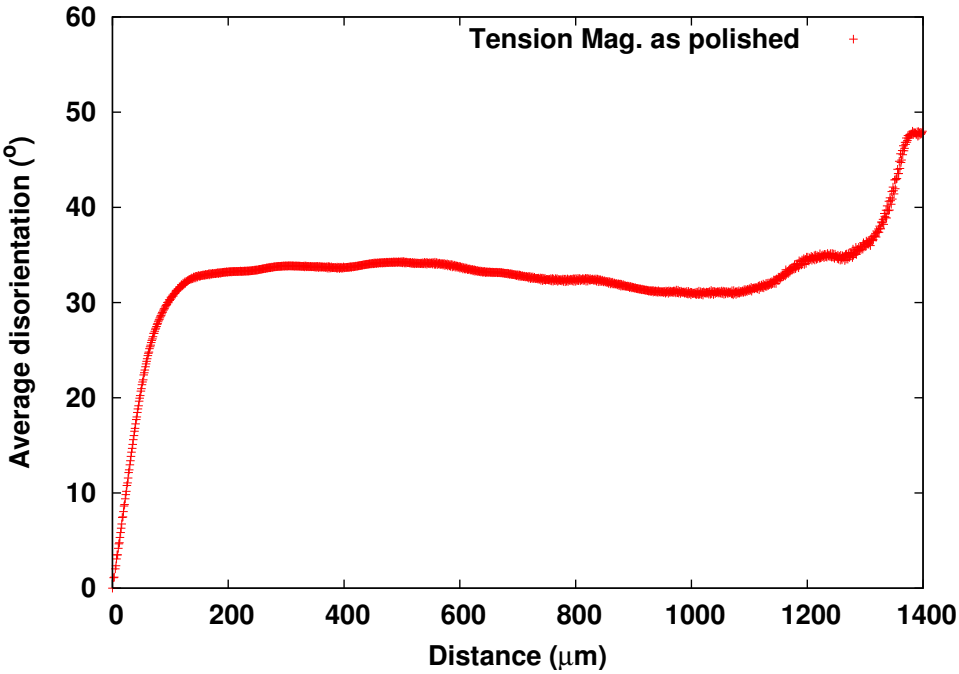

Figure 2.4: Average disorientation as a function of distance for pure Magnesium extruded rod. Initial steep part of the DDF is due to sampling inside the grain.

data set shows a more pronounced effect of local clustering. To illustrate this point the EBSD scan obtained from the sample of pure Mg (0% compression) was subsampled. Two cropped areas of $300 \times 300\mu m$ and two cropped areas of $500 \times 500\mu m$ were selected from random location in the full scan. The DDF for these 4 sub-scans was obtained. Figure 2.6 shows DDF of the 4 scans along with the DDF for the full sample. For all the sub-scans the transition point (from steep slope) is the same within acceptable error implying that the average grain size is similar in all the sub-scans. The two different $300 \times 300\mu m$ scans have different functional forms of the DDF as compared to each other as well as the full scan. For example at a distance $300\mu m$ between two pixels in the sample 300–II has a higher value of disorientation than the sample 300–I showing the influence of the local clustering on DDF. At $300\mu m$ there are more pairs with higher misorientation for 300–I sample as compared to the sample 300–II. The DDFs of samples 500–I and 500–II are closer to each other than those of samples 300–I and 300–II. Neither of these DDFs is close to the DDF of the full scan. Thus the data in the sub-scans (shown in Fig. 2.6) is not representative of the entire scan. In other words the RSS for pure Mg sample before deformation is larger than $500 \times 500\mu m$. The procedure to obtain the RSS using a qualitative method is outlined below.

2.4.1 Heuristic algorithm to obtain RSS

To obtain RSS the following algorithm is used:

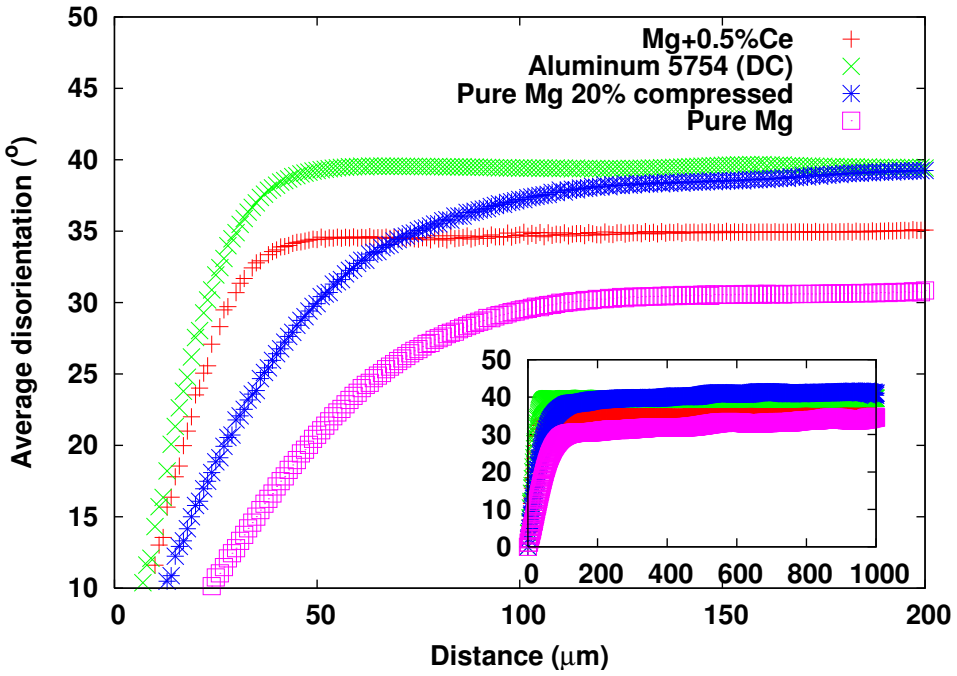

Figure 2.5: Effective grain size from DDF for different materials. Effective grain size is obtained when the slope of the DDF curve changes. Inset: DDF for the entire scan.

1. Crop subsets of the EBSD data.
2. Obtain DDF for the cropped scans.
3. Compare the stitched DDF with the DDF for entire sample (i.e. $1000 \times 1000 \mu m$ scan).
4. Repeat, increasing the subscan dimensions, till convergence is achieved. Convergence is evaluated by comparing the information mismatch with DDF for entire sample.

For each subset of the data multiple sub-scans, $DDF_{X_{dim}Y_{dim}}$, at random locations in the microstructure are cropped. The number of subscans (n) is chosen such that $n\times$(subscan size) is the same as the size of the entire scan. The initial part, sampling within the grain, and the tail of the DDF is removed. The DDFs are then stitched together. The stitching is done by concatenating the DDFs obtained from the subscans ($DDF_{X_{dim}Y_{dim}1}$, $DDF_{X_{dim}Y_{dim}2}$, ..., $DDF_{X_{dim}Y_{dim}n}$) by:

1. shifting the origin of each subsequent DDF ($DDF_{X_{dim}Y_{dim}2}$ etc) by the subscan size and
2. adjusting the DDF so that the combined DDF is continuous across boundaries.

This stitching is similar to microstructural stitching of a representative volume element (RVE). The stitched DDF is then compared to the DDF of the entire scan (entire scan is the $1000 \times 1000 \mu m$ scan). The

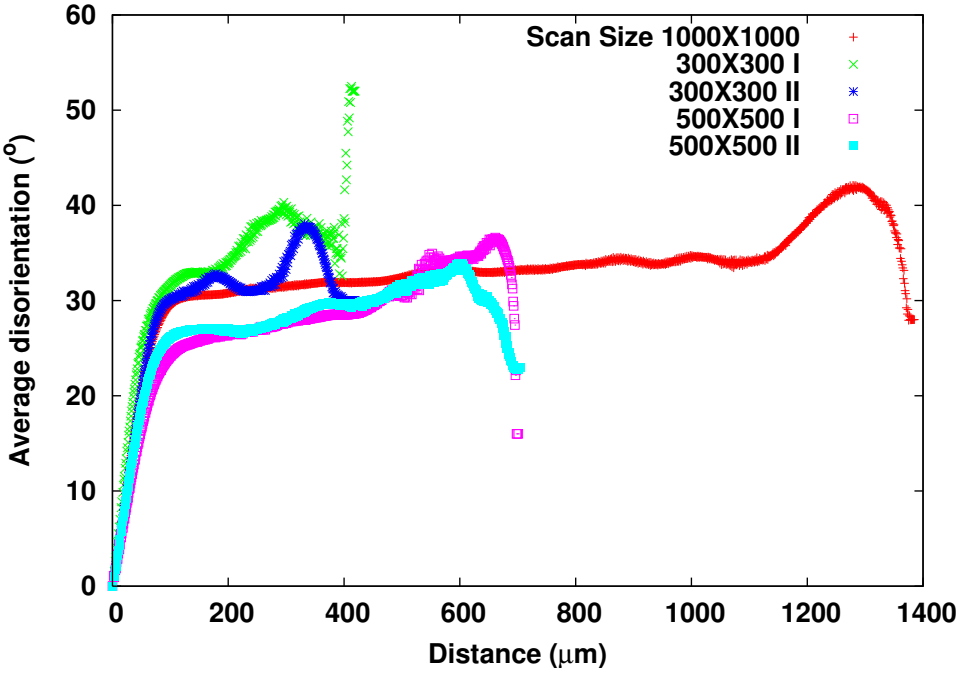

Figure 2.6: Effect of scan size on LRO for pure Magnesium (0% compression) sample.

motivation is to test if sub-scan can be used as basic building block to reconstruct the full data. This procedure is illustrated in Fig. 2.8.

As stated, only the intermediate part of DDF is considered in conjunction with information theory. The choice of maximum distance is taken to be dim_{min}. This denotes the distance between pairs of points/pixels in the sample. It should be mentioned that not all the pairs that are sampled by this method are close to the edge of the scan. For example in the extreme case of a square sample (where dim_{min} is the same as dim_{max}) the maximum distance is 1.414 dim_{min}. Thus the ratio of distance sampled to the maximum distance is 0.7. Figure 2.7 (below) demonstrates this phenomenon. The domain D is the original window while domain $C\{C_1, C_2, C_n\}$ is the cutoff distance. Domain C consists of a set of circles with diameters dim_{min}. The pairs are generated from intersections of domains D and C. As can be seen from Fig. 2.7, this procedure samples pairs that are also internal (i.e. not close to scan edges).

Comparing the DDFs of different scan sizes shows that the fitting, with full scan, improves as the sub-scan size is increased. The $900 \times 900 \mu m$ sub-scan is visibly the closest to the full scan DDF. This comparison gives a visual estimate of the RSS but is of a qualitative measure. A quantitative measure is needed to make a reliable comparison of RSS of different sub-scan sizes. For this the approach used here is to cast the problem in terms of information theory as explained in detail in section 2.5 below.

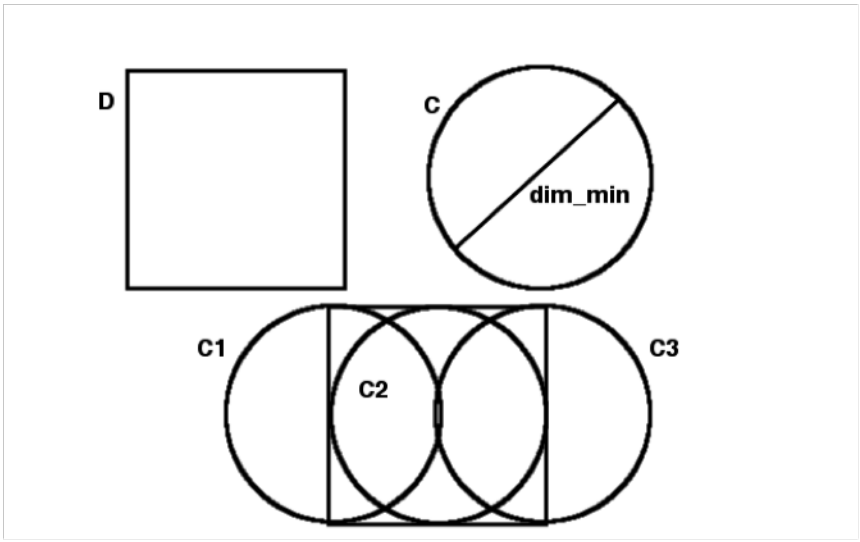

Figure 2.7: Procedure of sampling the EBSD data

2.5 Information Theory

This section presents a new mathematical framework to measure the information mismatch between different EBSD scans with the aim to obtain a quantitative measure to evaluate the RSS. The mathematical framework allows us to quantify the information stored in the DDF statistic. First DDF, obtained from the EBSD data, is treated as an information source. Then a proper norm is defined to measure the information mismatch between different DDFs. RSS is identified as the scan size which gives asymptotic convergence of the information norm.

For the purposes of this work the optimal representative scan size is determined using Fisher information and entropy norm ([69, see]). Fisher information function for regression model, as a conditional expectation of the likelihood function is given by:

$$I_{Fisher}(\theta) = E\left[\frac{\partial}{\partial\theta}\left(\log f(X,\theta)^2\right)|\theta\right] \tag{2.4}$$

Fishers information measures the amount of information that observed variable X carries about an unknown parameter θ. E on the right hand side of Eq. 2.4 denotes the expectation value of the terms enclosed in square brackets. To measure the Fisher information mismatch, or distance in general, in between data sources one should obtain a proper norm for such a measurement.

Kulback and Leibler [70] constructed a complete norm, KL norm, for the information measurement between information data sources using Radon-Nikodim theorem from functional analysis. In the discrete probability space KL norm could be assigned as non symmetric probability distance norm or gain between

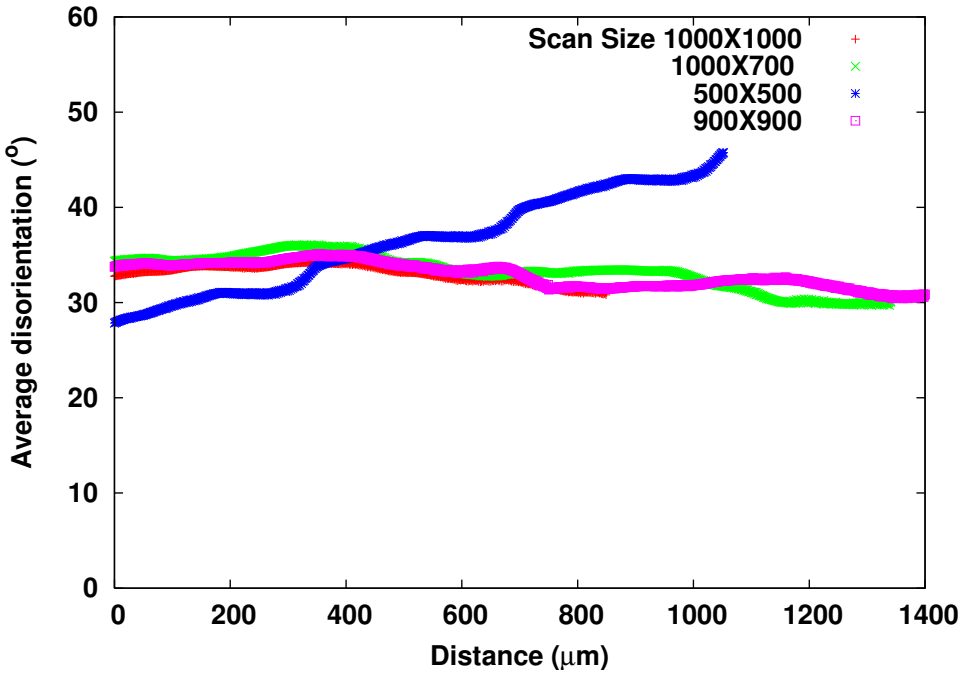

Figure 2.8: DDF for different scan sizes for pure Magnesium (0% compressed). The DDF curve for 900×900 (magenta) is visually the closest to the 1000 × 1000 DDF curve (red).

two information sources and takes the form:

$$KL(p(x_i), q(x_i)) = \sum_{i=1}^{n} p(x_i) \ln \frac{p(x_i)}{q(x_i)} \tag{2.5}$$

where $p(x)$ and $q(x)$ are probability density functions constructed for the each information source.

Let $< \Omega, B, F >$ be the probability space where Ω is the initial probability space constructed on the sample EBSD data (which includes crystallographic texture and spatial information), B is the event space (subset of collections of Ω, this event could be described as the probability of disorientation θ_{ij} for a particular distance d) and F is the probability measure with properties of non negativity, normalization and countable additivity. This probability measure reduces dimensionality of the problem and creates the possibility of general analysis of given data from the perspective of stochastic processes. It can be written as:

$$F_\Omega = I_\Omega = \frac{\sum_{j=1}^{n} \sum_{i=1}^{n} D_{ij}\theta_{ij}}{\sum_{j=1}^{n} \sum_{i=1}^{n} D_{ij}} \tag{2.6}$$

Thus F_Ω represents normalized DDF. D_{ij} is the distance between pixel i and pixel j, θ_{ij} is the disorientation between them and n is the total number of pixels in the scan area.

DDF statistics is extracted from the EBSD data. Using this we can calculate the KL divergence which in turn is used to determine the RSS by minimizing the KL divergence with "full information". Table 4.1 summarizes the various parameters and variables used in this section.

Another parameter T is added to the probability space, such that $\{\Omega^T\}$ is the set of sub-scans having same dimensions obtained from the full scan Ω. $\{\Omega^T\}$ is obtained by sampling the full data with "method of sliding windows" [71]. To generate a set of subscans with same dimensions (X_{dim}, Y_{dim}), first we choose a center (X_C, X_C) for the sub scan randomly such that $(X_C, Y_C) \in [X_{max} - X_{dim}/2, Y_{max} - Y_{dim}/2]$. The subscans are then stitched as discussed before in Sec. 2.4. Then information statistics (I_{Ω^T}) is calculated for the each Ω^T. Next step is to calculate information mismatch and if this is more than a threshold- we increase the scan dimensions by $100\mu m$ in either X–direction or Y–direction. Figure 2.9 illustrates this procedure pictorially.

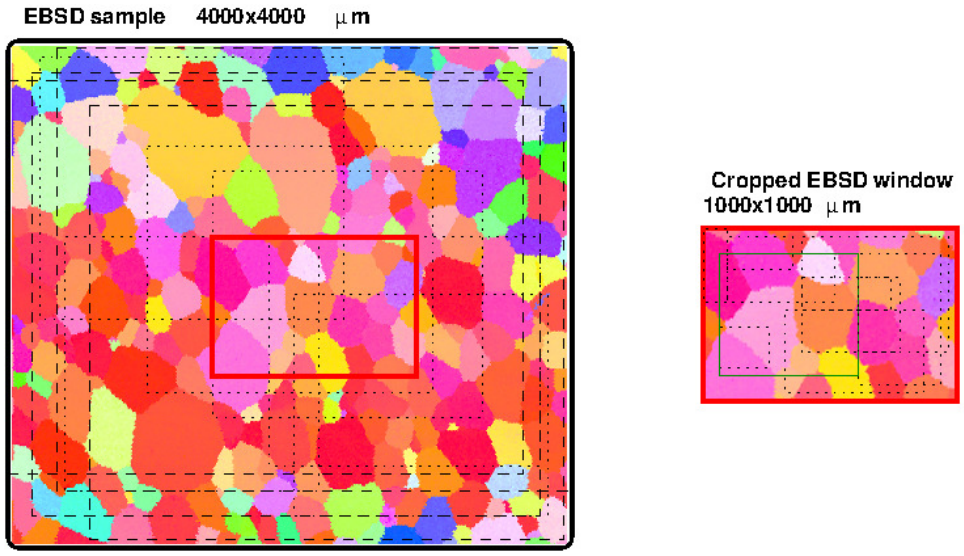

Figure 2.9: Process of sliding window and collecting information from the EBSD sample: Red window 1000×1000 μ m shows the constant KL norm through the initial sample 4000×4000 μ m. After selecting constant entropy window we continue windows analyses until KL norm is minimized with minimum dimensions (RSS) - green window

The next step is to define a norm between so-called full information distribution and local distribution (contained in the sub-scan). We would use Kullback -Leibler norm for the probability space that we define before:

$$D_{KL}\left(I_{\Omega_{full}}[i], I_{\Omega^T}[i]\right) = \sum_{i=1}^{n} I_{\Omega_{full}}[i] \ln \frac{I_{\Omega_{full}}[i]}{I_{\Omega^T}[i]} \tag{2.7}$$

I_{Ω^T} is the information statistics gathered from each stochastic process from the sub-scan. $I_{\Omega_{full}}$ is the information gained from the 1000×1000 scan size.

Using the KL divergence and limit theorem of divergence for the entropy we can now construct a complete mathematical model. For each information space we want to construct topologically optimal

dense subspace Ω_{opt}. Optimality is given by:

$$D_{KL}\left(I_{\Omega_{full}}, I_{\Omega_{opt}}\right) \rightarrow 0 \tag{2.8}$$

Thus $I_{\Omega_{opt}}$ represents the normalized DDF of the optimal scan. In the present work this information statistic is the DDF of the intermediate part. The underlying assumption is that EBSD scan of 1000×1000 (Ω_{full}) contains the full information. This was verified by asymptotic convergence to low value of KL norm for larger dimension scans (2000×2000 etc.). This procedure is highlighted in Fig. 2.9 using the method of sliding windows. The scan size with full information is chosen to be 1000×1000, because the KL norm for 1000×1000 sample chosen from a random location in the material (for all materials) is similar to the KL divergence of larger samples. The smaller size for full information makes the problem computationally tractable. Also, if 1000×1000 does not contain the full information then the KL norm will not show asymptotic convergence for scan sizes less than 1000×1000 like the one shown in Fig. 2.10.

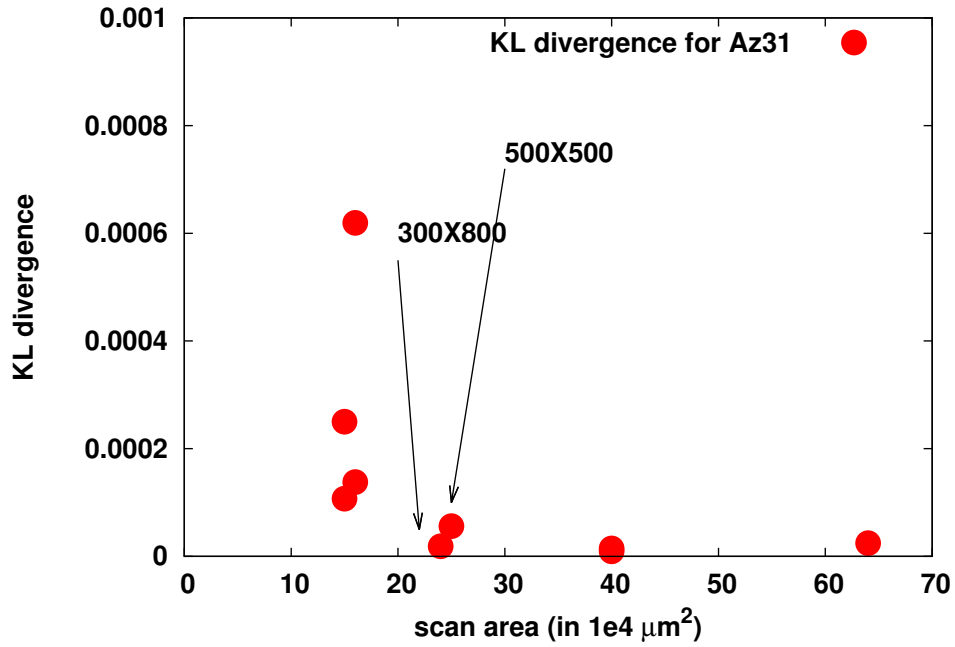

Figure 2.10: K-L divergence for AZ31. The divergence value asymptotically approaches 1e-6 with $300 \times 800 \mu m$ as the representative volume.

The solution in the discrete space could be represented as:

$$x_{min}, y_{min} \in \{x, y\} : D_{KL}\left(I_{\Omega_{full}}, I_{\Omega_{opt}(x,y)} < \epsilon\right) \tag{2.9}$$

ϵ is a parameter which determines the convergence. The ϵ value for convergence of KL divergence for each subscan is based on the full information sample (1000x1000) and is material dependent. This ϵ value

is the information mismatch between the full sample and any larger scan. From all the possible sample dimensions ($\{x, y\}$) one needs to find the minimum dimensions (x_{min}, y_{min}) such that it minimizes the KL entropy norm (KL divergence), corresponding to minimum values of the scan size along x and y respectively. Figure 2.10 shows the KL divergence calculated using Eq. 4.5 for various sub-scan sizes of the AZ31 data set. The quantities being plotted are the scan area (in μm^2) along the X–axis and the KL divergence along the Y–axis. Instead of using the X and dimensions separately the scan area is used as the independent variable but the KL divergence calculated for each scan depends on the scan dimensions and not scan area. KL divergence shows the information mismatch between the full information (1000×1000 scan) and the information contained in the sub-scan. Figure 2.10 shows that after a scan size of 2.4×10^4 μm^2 the divergence reaches the asymptotic value of 10^{-6}.

Thus the RSS for AZ31 is a scan size of 2.4×10^4 μm^2 which corresponds to a scan size of $300 \times 800 \mu m$. Note that the scan size of 2.5×10^4 μm^2 (500×500) has higher value of KL divergence. This shows that one needs more data along the sample Y direction than the sample X direction (800 vs. 300). Obtaining the optimal solution for RSS was done by creating an automated framework based on parallel codes and optimization algorithms.

2.6 Discussions

As noted earlier DDF gives complete description of distance between any two points in the EBSD scan and the average disorientation between them. Minimizing the KL divergence, which is calculated using the intermediate part of the DDF, maximizes texture information as well as spread of texture throughout the microstructure. Using DDF with KL divergence gives a mathematical tool to quantitatively determine when a sub-scan is representative of the full scan. In simple terms the sub-scan is representative of the full scan when the information contained in the sub-scan is identical to the information contained in the full scan within accepted error of ϵ.

This procedure is repeated for all the materials listed in Table 2.1. The updated table with the RSS is presented in Table 2.2. Table 2.2 shows that there is a correlation between the grain size and RSS. A first valuable observation could be made based on the amount of grains in RSS for different materials and processes. As it can be seen in Fig. 2.11, the processing of the material changes significantly the amount of grains required for the RSS. For small grained material the RSS is smaller. However, the amount of grains will be significant fot some fine grains materials due to their texture strength and processing anisotropy.

To investigate, this RSS is plotted as a function of grain size and is presented in Fig. 2.12 which shows a linear correlation between RSS and average grain size. The slope of the linear best fit is 14.10.

The DDF can be used to calculate the effective grain size. The value of effective grain size (r_{DDF}) is defined as the distance between two pixels at which the slope of DDF changes significantly from a high value, corresponding to sampling within the grain, to a lower value. The r_{DDF} is obtained by calculating the slope of the DDF curve and the point where the slope first approaches 0 is taken as the grain size. r_{DDF} for all the materials presented in Table 2.1 are calculated from their respective DDFs and presented in Table 2.3. The r_{DDF} is greater than the average grain size measured by the intercept method. The Fig. 2.12 can be redrawn showing the optimal scan size as a function of r_{DDF} (Fig. 2.13).

The discussion presented above provides a framework for choosing the size of the EBSD scan based on morphology and size of the grains as well as their relative orientations.

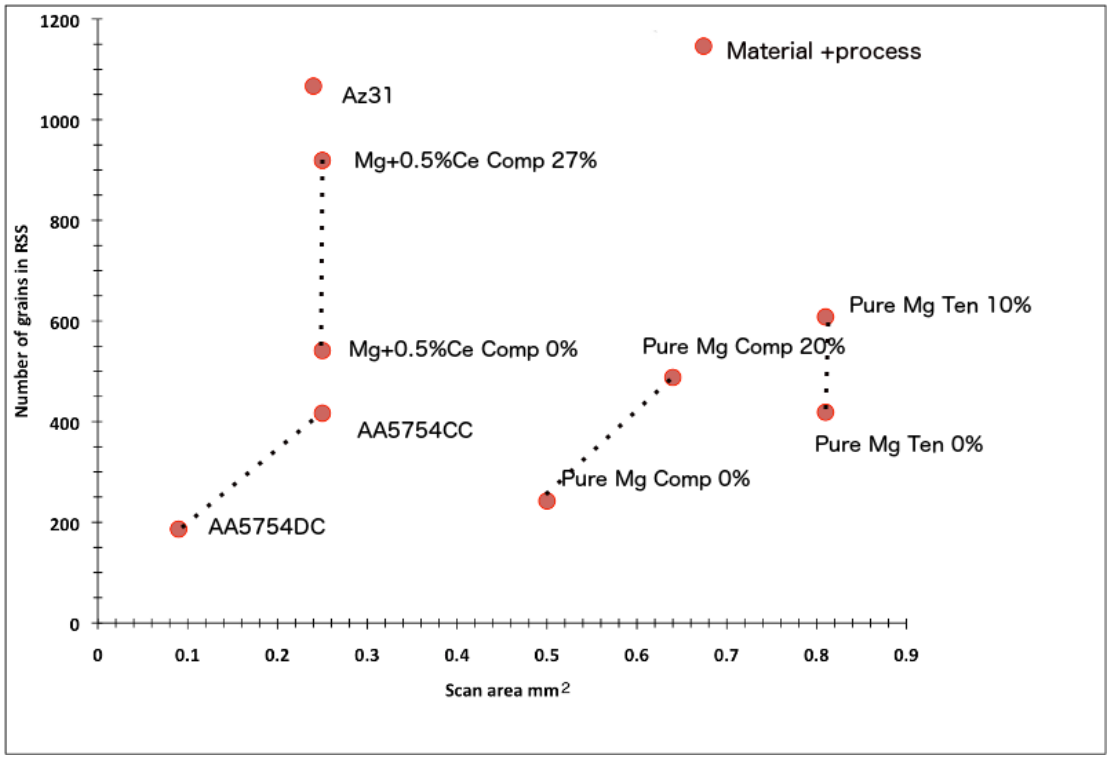

Figure 2.11: Number of grains in RSS as a function of a scan size.

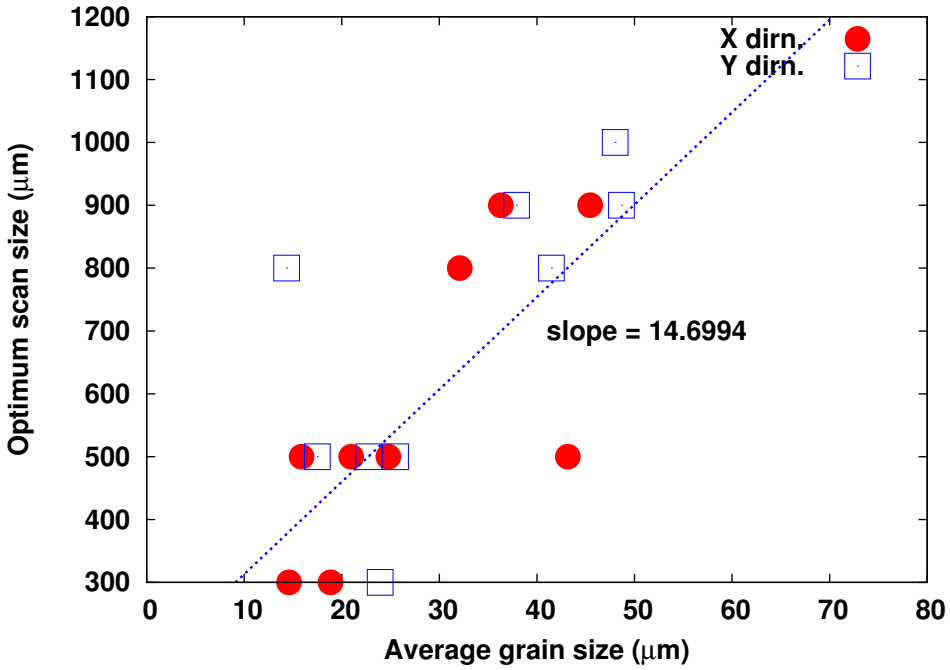

Figure 2.12: Optimal scan size as a function of average grain size.

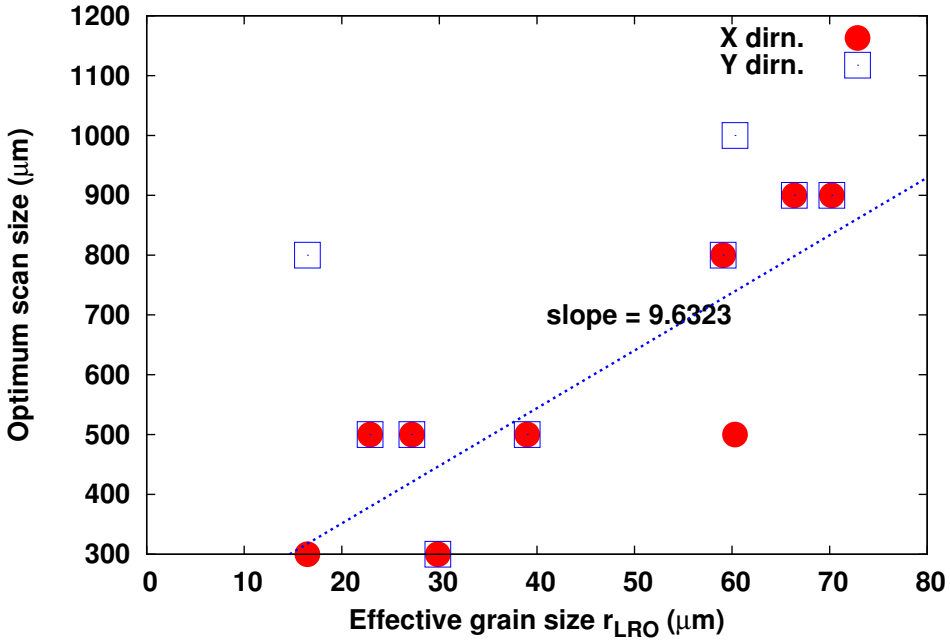

Figure 2.13: Optimal scan size as a function of r_{DDF}. The data points labeled X–dirn (in red) and Y–dirn are the dimensions along X–axis and Y–axis respectively of the optimal scan.

Table 2.2: Experimental data.

Material		Grain size (μm) using intercept method		Texture strength	representative scan size (RS	
Type	Condition	X	Y		along X	along Y
AA5754	CC	24.77	25.52	1.775	500	500
AA5754	DC	21.38	23.94	3.4	300	300
Pure Magnesium	Tension 0%	45.46	48.67	5.84	900	900
	Tension 10%	36.30	37.91	5.892	900	900
	Compression 0%	43.17	48.02	5.411	500	1000
	Compression 20%	32.09	41.48	9.088	800	800
Mg+0.5%Ce	Compression 0%	20.96	22.78	3.347	500	500
	Compression 27%	15.88	17.49	5.078	500	500
AZ31	extruded	14.59	14.34	16.16	300	800

The effect of texture is more complicated to be discerned from the current data. Though the general trend seems to be that stronger the texture smaller the RSS. The grain size for the two aluminum samples in Table 2.1 is very similar but the texture of the DC sample is about twice as strong as that of the CC sample. The RSS for DC is smaller than the RSS of CC. One can be tempted to say that the proportionality factor of RSS and 1/(texture strength) is close to unity from the aluminum but one has to be cautious as the texture strength, even though reported as a single number here, has a lot of complexity. The pure Mg compression data shows another level of complexity when the textures are widely different. The texture strength increases when the sample is compressed and the RSS, instead of decreasing, increases (along the X direction). The pole figures for the 0% compression and 20% compression Mg samples are shown in Fig. 2.14. The texture plots for both the samples are very different from each other and texture strength alone is only one factor to represent the overall texture of the samples.

Figure 2.15 shows the combined effect of average grain size and texture strength on optimal scan size. It shows the RSS on Y–axis plotted against (average grain size)/(texture strength) along the X–axis. The blue dotted line, used as a guide for the eye, shows that the slope of the best fit line is ∼37.45. Giving the following form for evaluating the RSS:

$$RSS = 37.45 * \frac{\text{grain size}}{\text{texture strength}} + C_1 \tag{2.10}$$

A 3D plot showing the dependence of RSS on average grain size and texture is included in the supplementary material as a movie.

These observations are consistent with what can be expected from an information flow point of view. If two scans have the same size (dimensions) but the grain size of one is smaller than the other then the amount of information (in terms of discrete orientations) will be higher for the small grained sample. As a

Material		Average grain size intercept method		Grain size from DDF
		X (r_x)	Y (r_y)	
AA5754	CC	24.773	25.513	39.00
	DC	21.84	23.936	29.85
pure Magnesium	Tension 0%	45.459	48.671	70.23
	Tension 10%	36.302	37.913	66.38
	Compression 0%	43.171	48.018	60.3
	Compression 10%	32.089	41.482	59.09
Mg+0.5%Ce	Compression 0%	20.957	22.781	27.18
	Compression 27%	15.882	17.493	22.90
AZ31	extruded	14.592	14.344	16.47

Table 2.3: Intercept grain size Vs. grain size from DDF

result a smaller RSS will be required for the sample having small grains. Similarly if a sample has stronger texture then the spread (variance) of orientation in the individual grains will be smaller. As a result a smaller subset can have the same amount of information as the bigger set, leading to a smaller RSS.

2.7 Conclusions

- The results presented in this study indicate that for accurate texture analyses, the orientation distribution function alone is insufficient. ODF does not include the entire statistical cross correlations that exist in the data, such as short and long range ordering of texture. Thus, these cross correlations can only be obtained by employing both ODF and DDF.
- DDF in conjunction with information theory (and in particular KL divergence) can be used to give a representative scan size for a given EBSD data. This RSS can be used to construct an optimal design of experiment (ODE) to get the most optimal scan size without collecting excessive amount of data. DDF data, for the materials studied in this work, suggests that the scan size depends on average grain size and texture strength. The proportionality is of the following form:

$$\begin{aligned} RSS &\propto \text{grain size} \\ &\propto \frac{1}{\text{texture strength}} \end{aligned}$$

- To be truly free of the clustering effect and hence to obtain a RSS the scan size needs to be bigger than 10 times the grain size - RSS = 10 $\times$ grain size. This RSS may be related to long range stress fields.

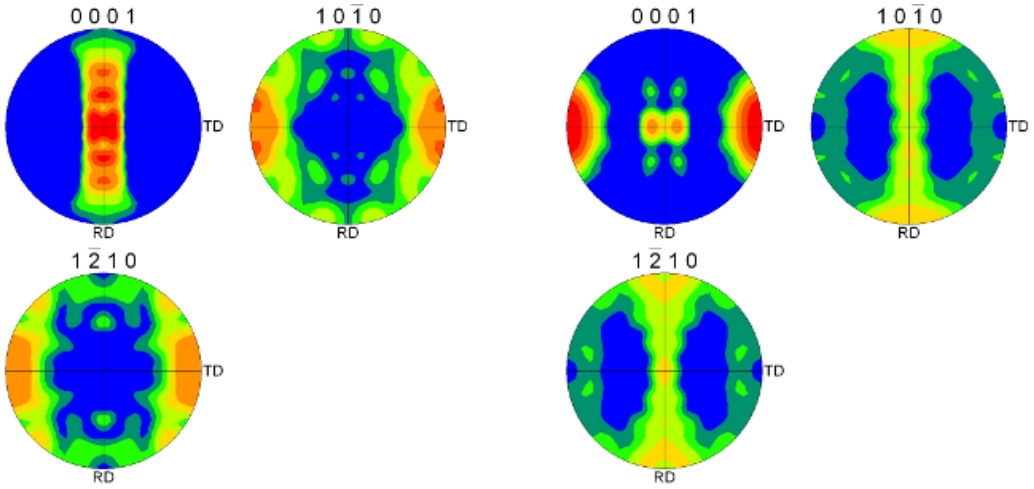

(a) 0% compressed (b) 20% compressed

Figure 2.14: Comparing the texture for the 0% compressed and 20% compressed pure Mg samples.

- Scan area alone is not a sufficient quantity to determine the RSS. Both the asymmetry in the grain size and texture give rise to asymmetry in the RSS. Thus by extension RSS along RD-TD cross section is not enough to determine the RSS for RD-ND cross section.
- The RSS obtained from such an analyses should be used as an input to generate 3D microstructures as well as modeling (crystal plasticity, recrystallization etc.). The RSS can also be used as building blocks of much larger samples.

This work was supported by the Natural Sciences and Engineering Research Council of Canada (NSERC) and General Motors of Canada. The authors also great-fully acknowledge the High Performance Computing Center at the University of Sherbrooke (RQCHP).

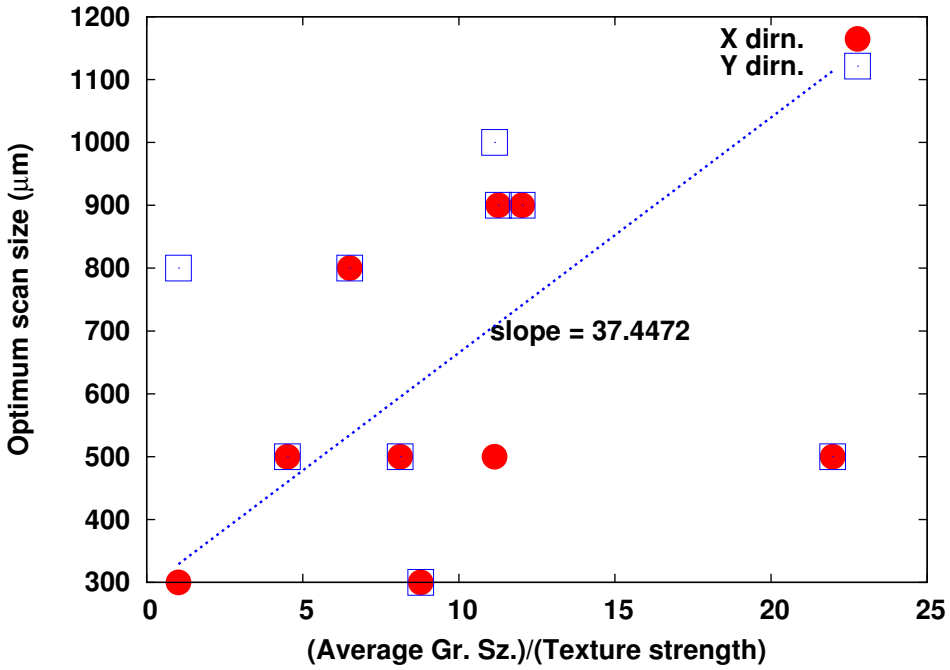

Figure 2.15: Combined effect of average grain size and texture strength on optimal scan size

Chapter 3

Analytical estimation of distance–disorientation function of the material microstructure

This work presents a new functional approach to estimate the distance-disorientation correlation function of a given microstructure. The proposed approach separates the crystallographic domain into texture defined by its Euler angles (ϕ_1, Φ, ϕ_2) and geometrical domain defined by distance distribution function D_{ij} The crystallographic domain is treated as independent (known) variable and an analytical estimate for the Euclidian distance distribution function (D_{ij}) is obtained. The proposed analytical solution for the estimation of D_{ij} is based on existing statistical growth models and the logistic probability distribution function (PDF). The solution is optimized for the measured experimental data and takes into account morphological features of the microstructure such as grain volume, grain radii, grain size as well as their distribution inside the material. An analytical model is proposed for constructing the distance-disorientation function (DDF) using the estimated Euclidian distance between pixel pairs. The new functional solution is a highly efficient way to calculate DDF values, making it suitable for application to the real microstructure optimization problems. The DDF obtained by using the results of probabilistic solution are validated by comparing them with the DDF obtained from experimental electron back-scatter diffraction (EBSD) data.

3.1 Introduction

Increasing need for numerical modelling of material behavior for engineering applications has been accompanied by the development of the electron backscatter diffraction (EBSD) as an indispensable tool for implementing quantitative microstructure related parameters like grain morphology, crystallographic texture etc. into the model. Experimental EBSD maps have been directly employed for modeling recrystallization, cellular automaton based models as well as deformation using finite element analysis and fast Fourier transforms to name a few. In such studies, selecting data which is representative of the bulk material (representative volume element - RVE) is of prime importance. In modeling evolution of material

behavior of metallic materials undergoing mechanical or thermal treatments, evolution of morphological and crystallographic features of the grains need to be captured accurately. The changes in one grain have to be correlated to the changes in its immediate neighbors. The required distances over which input data has to be implemented in the model effectively determine the amount of area that needs to be scanned by EBSD measurement to be sure that the data is representative to study the metal behavior. In the early experimental work of Shechtman et al. [72] it was observed that the orientation ordering is far more than the grain size. Two-point correlation functions, especially distance disorientation functions (DDF), have been shown to provide a framework for implementation of quantified microstructural information into mathematical models. However constructing DDF from EBSD data and implementing them in numerical models in a computationally tractable manner has been a challenge, limiting the utilization of advanced experiemntal methods to develop accurate microstructure-based models.

Correlation functions have been used in various fields from early works on scattering theory[73] to more recent works like the reconstruction of three-phase microstructures[23], where large amounts of experimental data need quantification in a manner that is amenable to model development. { Historically the correlation functions in the solid state physics were implied in the work by Cosserat [13]. They presented description of the stress with micro rotations which introduces length scale effects in classical elasticity. The Cosserat theory applied for size effects of polycrystals related to their mechanical behavior is discussed in details in the work of Forrest et.al. [74]. In discussion of the correlation functions it is important to mention the works of Beran et.al. [75, 14, 76] where authors introduced and developed a statistical theory of heterogeneous materials. The later implications of statistical theory and specifically correlation functions were developed and discussed in details for measuring mechanical responce of the microstructures in the works of McCoy et.al. [77] and Beran et.al.[78].

Considerable research was performed in the field of application of n-point correlation statistics to the problems of three-phase microstructure reconstructions [15, 16, 17, 18, 19, 20, 21, 22, 23]. The main idea is to reconstruct the full microstructure media from the n-point correlation statistics using different optimization and homogenization techniques. Various research studies of correlation between particle interactions with the length scale effect were studied and discussed in the experimental and modeling works of Glicksman et. al. [24] and Wang et.al. [25, 26] . In their research, the authors presented the study of spatial and nerest-neighboor correlations in a polydispersed particle systems.

The analysis of crystallographic orientation space, measured by electron backscatter diffraction (EBSD) technique, is associated with large amount of data on orientation and grain morphologies. Precise analysis of such microstructure data from the perspective of data mining could provide useful quantitate information and aid in developing material model with precise microstructural information for engineering applications. Recently, Jiao *et al.*[27] showed the application of n-point correlation, S_n, and in particular S_2 (two point correlation) to various practical problems including microstructural analyses for the real engineering materials. Neizgoda et al. [28] and Qidwai et.al. [29] in their recent works have shown application of 2-point statistics to the analyses of representative volume element (RVE). They highlight the importance of analitical estimators of 2-point correlation statistics found for the real microstructures and also discuss the gap in the field of obtaining an universal solution for the statistical descriptors. Torquato et. al [31, 32] have made some valubale contributions in the analitical approximations of n-point correlation statistics.

Analytical modeling of the two point correlation function was initially proposed by Corson[30] who used an exponential model:

$$P_{ij} = \alpha_{ij} + \beta_{ij} \exp(-c_{ij} R^{n_{ij}}) \tag{3.1}$$

where P_{ij} is the two point correlation function, R is the distance vector separating the two phases i and j,

and α, β, c and n are coefficients obtained by curve fitting to the experimental data of interest. However, the obtained coefficients have no physical meaning and have to be evaluated for different material data sets. As pointed out by Sundararaghavan and Kumar[33] there is no clear connection between microstructure related parameters and those estimated from correlation analysis of that microstructure.

Garmestani *et al.*[34] gave analytical approximation which takes into account volume fractions V_j for grains with specific discrete set of orientations g:

$$P(g_j|(g_i, R)) = V_j + (1 - V_j \exp(-c_{ij} R^{n_{ij}})) \tag{3.2}$$

The parameters presented in their work are the same curve fitting parameters of initial conditional orientation correlation function (COCF)[30]. This solution improves the fitting procedure but still requires a significant effort for fit all of the coefficients of the particular model for a particular problem.

Experimental work to obtain precise microstructural correlation distribution function descriptor was presented by Tewari *et al.*[35]. The authors presented results and analysis for collecting a two-point correlation data for an Al–Si alloy with different material extrusion patterns. They highlighted the complexity of obtaining the two point correlation descriptor for measured EBSD data sample and proposed a procedure that can improve the computational time. They concluded that the observer needs at least 28×10^{12} measurements of the Cartesian distances measurements for a $500\mu m \times 500\mu m$ material sample. The proposed procedure is based on the usage of the dynamic lookup tables (**LUTs**) for computing distances and angles.

Two-point correlation function was also used for probabilistic modeling of microstructure evolution during Finite Element Modeling (FEM) in the work of Sundararaghavan et al.[33]. Authors show the applicability of the COCF, defined as the probability density of occurrence of a crystal orientation g' at a distance r from a given orientation g, to their FEM model. A Lagrangian approach was used to obtain the normalization constraints. However a major problem with analyses based on FEM probabilistic modeling of the microstructure evolution is the computational complexity of obtaining the COCF for each numerical integration point in the model.

Shan and Gokhale[40] studied distance disorientation function (DDF) for the nearest neighbors to construct microstructural representative volume element (RVE). DDF is defined as a function which correlates two pixels in the microstructure at the same distance from each other to the average disorientation between all such pairs. They measured different mechanical responses of the fibre material based on the different DDF patterns. DDF is concieved as a for of the the two-point correlation function. DDF calculates the average disorientation between two points while two-point correlation function correlates average probability for both points being in the same phase. DDF has also been studied as part of the distance-disorientation statistics on the experimental level by Beausir et al.[63].

The analytical study of the two point correlation function based on so-called texture functions in the Fourier space approximations could be found in the works of Adams et al.[36]. The Fourier space solutions are neither problem specific nor flexible to the real changes in the material specific microstructures[33].

The analytical solutions for the cross-correlations texture functions can be employed in a large variety of applications (see Fullwood et al. [12]) such as, long range ordering of texture, two point correlation function construction, representative scan size (RSS), microstructure based finite element method (FEM) modeling, micro-polar elasticity etc.

The process of obtaining the representative scan size using the optimization of the DDF was presented in the resent work of Brahme et.al.[79]. Using the information theory norms and optimization algorithms,

they presented a methodology to measure the information mismatch between two scans with different sizes. Furthermore, the authors demonstrated that, for different materials, orientation and misorientation distribution functions are not enough to describe the short and long ordering cross-correlation within the texture in order to obtain a representative scan.

Hence it is of practical interest to obtain the functional form for DDF as a form of the cross-correlation function of the COCF and two-points correlation function as they can be applied to modeling of the precise material microstructure evolution.

This work presents a new theoretical model to determine a functional form for distance-disorientation distribution (DDF). To obtain the DDF, one needs information on both the distance between any two given pair of points in the microstructure and the disorientation between them. This calculation, or any calculation of a two-point correlation function, is very time consuming. To address this problem research proposes to calculate the DDF in two parts; first obtaining an analytical solution for the geometrical domain (grain morphology and grain distribution) and then combining it with the crystallographic domain (grain orientation) to aid efficient quantification of the microstructure for implementation in engineering analysis of material behavior.

The first part of the work focuses on EBSD DDF analysis and statistical tests for the proposed solution (logistic distribution). The new functional form of DDF statistics is inherited from the ideas of the population model construction (Sec.3.3 and 3.3.2).

Next, the method to estimate the parameters for the analytical solution (logistic distribution curve) which is based on the microstructure morphology is presented. Instead of evaluating the exact DDF correlation statistics, the proposed method treats disorientation as a known fixed parameter (measured from the crystallographical Euler space of the microstructure and provided with the disorientation as a proper norm) and then estimates the distance function. The microstructure morphology analysis is used to obtain the estimators for standard deviation (σ) and mean (μ) required for the logistic curve for modelling distance distribution separately from the disorientation function (Sec. 3.4). Finally, the application of the constructed DDF solution based on the grain morphology is applied to large EBSD scans from Al and Mg samples and results are compared with measured DDF data to validate the new model (Sec. 3.5).

3.2 Experimental data

The EBSD data used in this study was acquired from magnesium and AA5754 aluminum sheet samples, using a LEO 1450 scanning electron microscope (SEM) fitted with a TSL EBSD camera. The EBSD data was analyzed using the TSL^{TM}OIM software (Ver. 4.6). The data was cleaned, {using grain dilation method with single iteration, neighbor CI correlation and single orientation per grain, to remove the bad data points and only data points having a confidence index (CI) above 0.2 were retained for the analyses. Grains were identified with a disorientation tolerance of 10°. Thus, the pixels having a disorientation of less that 10° were grouped together and identified as a grain. For the analyses, grains with less than 10 data points were excluded. Once grains were identified all the pixels in the grain were assigned average orientation of the grain. As a result, the disorientation of any two pixels within a grain is zero. The two materials, Mg and aluminum, with there different crystallographic systems (FCC and HCP respectively) were used to test the applicability of the functional form. The aluminum data was obtained from a direct chill cast and rolled aluminum sheet with grain size of $21 : 38\mu m$ and $23 : 94\mu m$ along the X and Y

direction respectively. For this sample, the step size for the EBSD map was $5\mu m$ and the texture strength was 3.4. The magnesium data was for an extruded pure magnesium rod with grain size of $45:46\mu m$ and $48:67\mu m$ along X and Y directions respectively. A step size of $2\mu m$ was employed for the EBSD map and the texture strength was 5:84. The number of grains in the scans varied from ∼500 for pure Magnesium samples to ∼8500 for the Aluminum sheet sample. Data analyses were done using the IBM SPSS Statistics (version 20.0) packages.

3.3 Analytical model construction

3.3.1 Distance-disorientation function

Distance-disorientation function[79] statistics (Eq. 3.3) provides full information about the dependency of the **distance between any two points** (Δ_{ij}) in the EBSD scan and as well as the average disorientation (Θ_{ij}) between them. In its discrete form the DDF function could be re-written as:

$$DDF = \frac{\sum_{i=1}^{n}\sum_{j=1}^{n}\Delta_{ij}\Theta_{ij}}{\sum_{i=1}^{n}\sum_{j=1}^{n}\Delta_{ij}} \tag{3.3}$$

DDF represents the full correlation information between the distance (Δ_{ij}) and the disorientation (Θ_{ij}). The average disorientation for all pairs of pixels, i and j, separated by a distance Δ_{ij} where the sum is over all grains and all pixels within each grain is given by equation 3.3. The procedure employed in this study to obtain the DDF (exact DDF from experimental measurements) is shown schematically in Fig. 3.1. A vector with distance, d_1, is chosen such that $d_1 < d_{max}$, where d_{max} is the maximum distance of vector connecting any two pixels in the scan. The average disorientation between all pairs of pixels having a distance d_1 is calculated. A new length d_2 is picked and this procedure is repeated for all possible distances.

It should be mentioned that, this definition of DDF goes beyond the misorientation distribution function (MDF)[7] and the misorientation correlation function (MCF) as presented by Beausir *et al.*[63]. The MDF considers only nearest neighboring pixels in the analysis while the MCF proposed by Beausir *et al.* gives the probability density for occurrence of a certain disorientation between pairs of grains at a certain distance. The DDF is similar to the orientation correlation function (OCF) as proposed by Adams *et al.* [64] where OCF is defined as the joint probability of orientation g occurring at a point P and orientation g' occurring at point P' such that P and P' are separated by a vector $\mathbf{r}$. However, the major difference between the two approaches is that, the DDF definition ignores the specific orientation g and g' and calculates the distance-disorientation correlation. Barton and Dawson[65] defined an *intra-granular* misorientation tensor by taking the dyadic product of misorientation between two points and the vector joining them. The DDF, as defined in this work, refers to a cross norm ([66]) of the misorientation tensor and is extended to any two points in the microstructure. Vorhauer *et al.*[68] have presented a similar definition of the DDF by investigating the disorientation as a function of distance within a ring, determined arbitrarily. Their work used the maximum ring size of $\sim 5\mu m$, which was smaller than their average grain size ($\sim 250\mu m$).

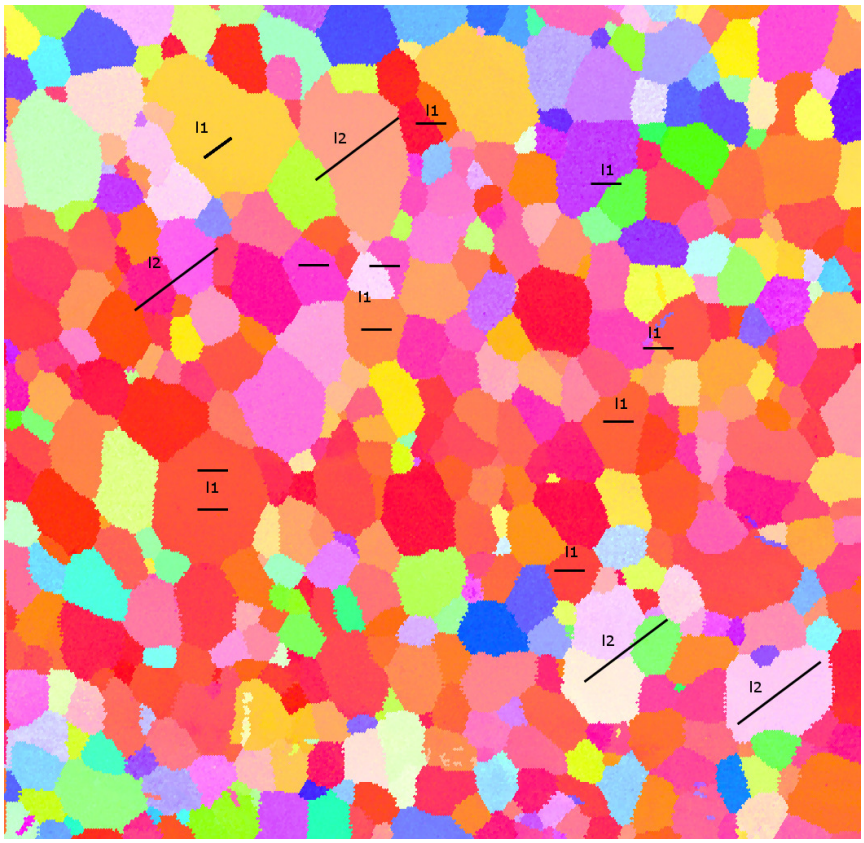

Figure 3.1: Procedure for determining DDF in Eq. 3.3

3.3.2 Obtaining Δ_{ij} based on the Population Model concept

Using the method discussed in previous section to calculate DDF is very time consuming. The method proposed in this section is to decouple the geometric domain and the crystallographic domain. i.e. recast the Eq. 3.3 in the following form:

$$DDF = \frac{\sum_{i=1}^{N}\sum_{j=1}^{N} D_{ij}\theta_{ij}}{\sum_{i=1}^{N}\sum_{j=1}^{N} D_{ij}} \tag{3.4}$$

where N is the **number of grains** in the geometric domain (microstructure). D_{ij} *now* refers to a **distribution of distances between a pair of pixels** belonging to grains i and j respectively, and θ_{ij} refers to the disorientation ([80]) between the average orientations of the two grains (as a result $\theta_{ii} = 0$). Once the functional form of D_{ij} is obtained then the DDF can be calculated using Eq. 4.3. It

Employing distance as the independent parameter requires the determination of a proper functional form of the clustering metric(D_{ij}). The population model is used to obtain functional description of the D_{ij} distribution, between any given pair of grains from the EBSD data. The population model was first proposed by Pierre Fran Verhulst in 1897 [81] who studied how fast population grows in a domain with respect to time. He proposed a relation between the growth (W), growth rate ($\dot{W}$), saturation limit (Ω) and time t. Verhulst considered a model of the population growth of the form:

$$\dot{W}(t) = \beta W(t)(\Omega - W(t)) \tag{3.5}$$

where Ω denotes the upper limit or saturation level of growth (W), as $t \longrightarrow \infty$, and β is the proportionality constant given by $\beta = \dot{W}(t)/W(t)$. Growth is proportional to both the population already attained, $W(t)$, and to the remaining room for further expansion, $\Omega - W(t)$. Verhulst has shown that, population $W(t)$ follows a logistic curve:

$$W(t)_{CDF} = \Omega\frac{exp(\alpha + \beta t)}{1 + exp(\alpha + \beta t)} \tag{3.6}$$

Further this function was re-derived and used in various statistical applications as logistic cumulative distribution function (CDF) [81]. The density of the logistic CDF through the parametrization and derivation of the equation 3.6 takes the form:

$$W(t, \mu, s)_{PDF} = \frac{e^{-(t-\mu)/s}}{s(1 + e^{-(t-\mu)/s})^2} = \frac{1}{4s}sech^2\left(\frac{t-\mu}{2s}\right) \tag{3.7}$$

where t is the sample variable, μ is mean and s is parameter proportional to standard deviation.

Proposed research is based on the well-known model of the population growth, providing completely new application to the Microstructure analyses field. In this study, $W(t)$ will represent the growth of distances between pairs of points $\in \{ij\}$ such that indices i and j represent a pair of grains in the microstructure. For any two given pair of grains in the entire sample, $W(t)$ increases from 1 to the saturation limit of Ω. The saturation limit in the proposed model is reached when all the possible pairs (of points) in those two grains are accounted for (Fig. 3.2). This growth, W, can be identified with D_{ij} (accumulated statistics for distance distribution between each pixel within the grain pair). In the Fig. 3.2, the sequence $G_{k1}..G_{kn} \rightarrow G_{k+1}$ represents the pixels inside the particular grain G_{k+1}. Thus, the D_{ij} between two grains 1 and 2, D_{12}, is obtained by taking all pairs $\{kl\}$ so that $k \in \{G_{01}..G_{0n} \rightarrow G1\}$ and $l \in \{G_{11}..G_{1n} \rightarrow G2\}$ ($G1$ is the first grain in a sequence etc..).

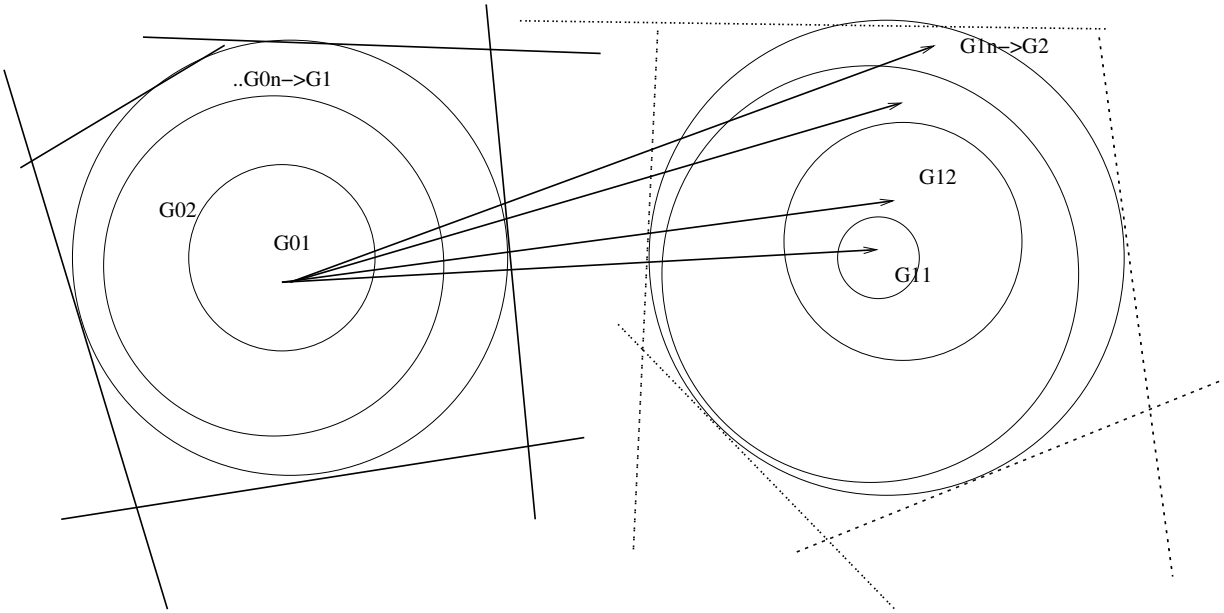

Figure 3.2: Visual representation of distance growth (population) within points growth in the grain G1 and G2.

The entire $\{D_{ij}|i,j \in N; i \neq j\}$ is a compilation of probability density functions (PDF's) between individual grain pairs (for fixed i and j). For Aluminium and Magnesium D_{ij} data for all pairs of grains has smooth tails and is symmetric around the mode. PDF (as a function of distance) derived from EBSD data for Aluminum and Magnesium data is shown in Figs. 3.3, 3.4. Each data distribution histogram is similar to both normal and logistic distributions PDFs. The tails of the distribution are heavier than those expected for a normal distribution. To examine the validity of the underlying hypothesis that D_{ij} between each grain pair is close to the logistic PDF statistical tests can be done.

Results for, D_{ij}, from experimental data can be analysed using statistical methods Kolmogorov-Smirnov (KS) tests. This is done to determine if the D_{ij}s calculated from EBSD data are distributed logistically. Q–Q (quantiles plots) and P–P (probabilities-probabilities) plots can be generated for the logistic distribution. The P–P plot shows the relationship between cumulative expected probability and cumulative measured probability and is a measure of how close two distribution functions are on the same axes[82]. If the plots follow linear behavior with slope = 1 then the distributions are close or almost identical. The Q–Q plot represents the quantiles (regular intervals of the distribution function) of two distributions on the same plot. The P-P probability plot is more sensitive to deviances near the mean of the distribution while the Q–Q plot is more sensitive to deviances in the tails of the distribution. The P–P and Q–Q plots for D_{ij} distribution data for Magnesium, are presented in Figs. 3.5 and 3.6 respectively. The outliers of the Q–Q plot for Magnesium data indicates the mismatch of the tails fit which is the most complicated part of any distribution as an extreme value data. The skewness of tails and mismatch of the fit is visually pronounced for Mg data in the plots (3.4,3.10) the distance distribution plots The P–P and Q–Q plots for Al data sets are similar to those for Magnesium.

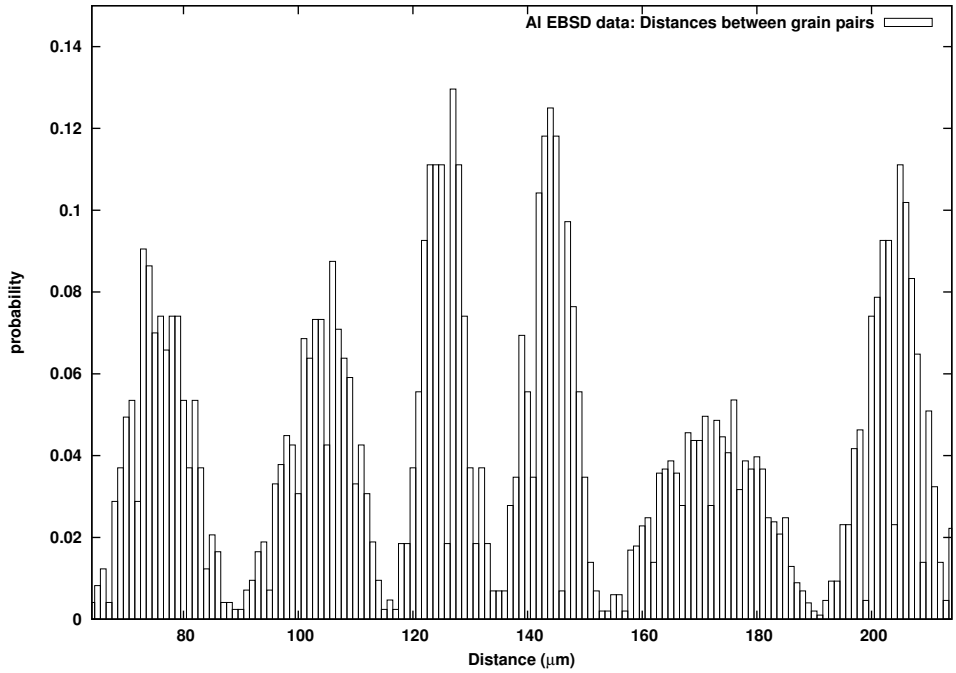

Figure 3.3: D_{ij} (μm) for random subset of grain pairs in Aluminum.

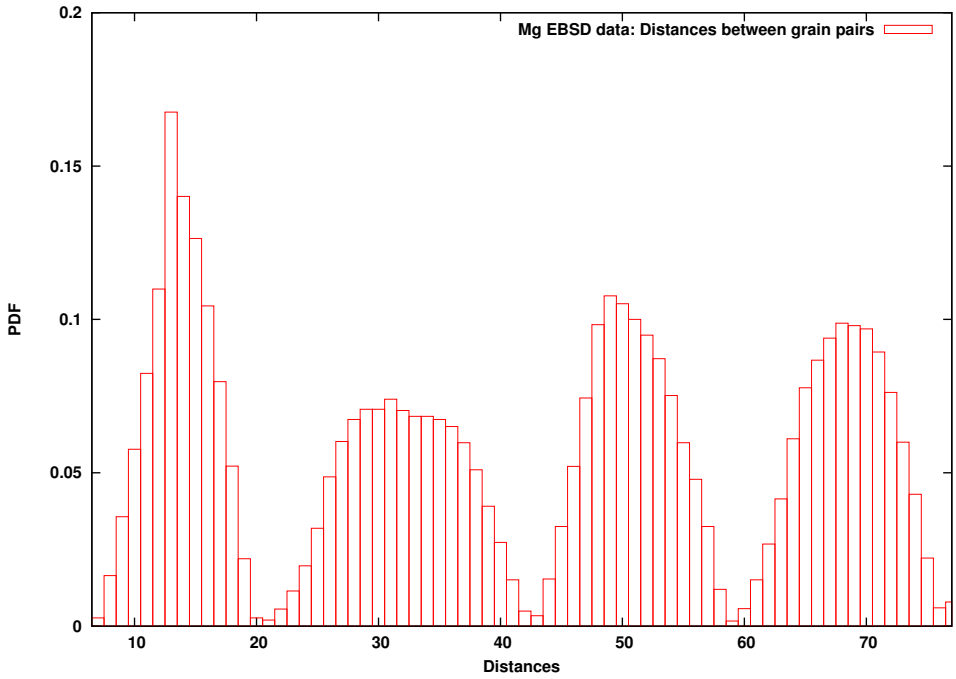

Figure 3.4: D_{ij} (μm) for random subset of grain pairs in Magnesium.

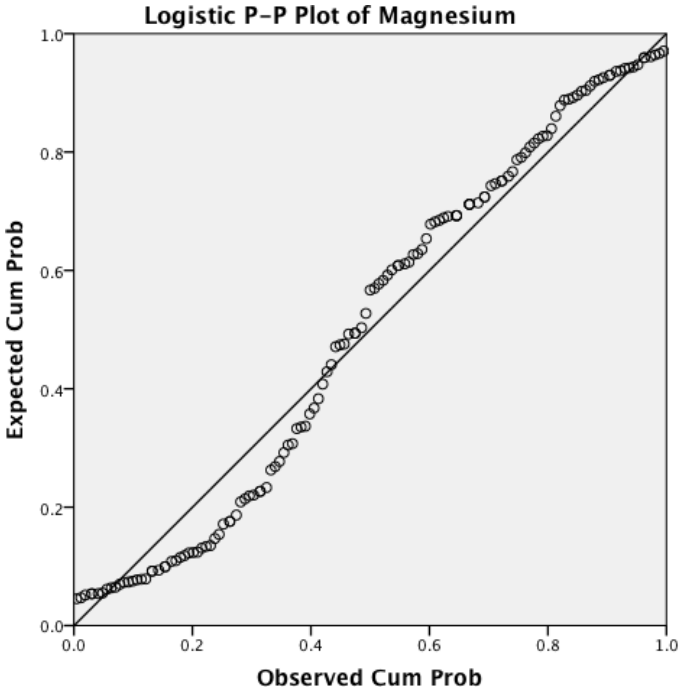

Figure 3.5: P–P Logistic plot for Magnesium sample

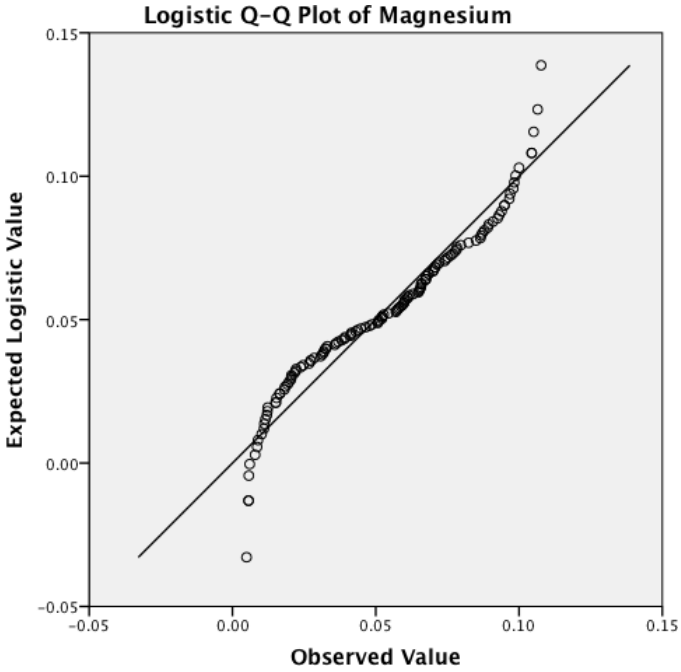

Figure 3.6: Q–Q Logistic plot for Magnesium sample

The visual data analyses (Fig. 3.3, Fig. 3.5, Fig. 3.6) shows good fit between the PDF values obtained from the experimental EBSD data and calculated logistic PDF values. The next step is to check the statistical reliability of the assumption that D_{ij} data is representative of the logistic curve PDF. The logistic density curve after re-parametrization of Eq. 3.7 is given by:

$$f(x;\mu,\sigma\sqrt{2}/\pi) = \frac{\pi}{\sigma 4\sqrt{2}} sech^2\left(\frac{\pi}{2\sqrt{3}}\frac{x-\mu}{\sigma}\right) \tag{3.8}$$

where, μ and σ are the mean and devitation of the data x[81]. To check that hypothesis we use Kolmogorov-Smirnof (**K-S**)[82] tests for the random D_{ij} sets from EBSD data. KS test shows how the two underlying probability distribution data sets differ. One set is the D_{ij} calculated from EBSD data and the second set is the D_{ij} obtained from logistic curve by using equation 3.8. The parameters μ and σ are calculated from the EBSD data and refer to mean distance and deviation in the distance. Measured D_{ij} data set is matched to the calculated logistic PDF dat set. This is followed by checking if D_{ij} data is logistically distributed. The significance of the K-S test for $\sim 10^3$ grain pairs for the different data collections (distance distributions between randomly chosen grain pairs) is that this permits the rejection of the null hypothesis that data sample is not logistically distributed. The complete analysis of full data collected from the EBSD scans with modeled data based on the proposed logistic solution is presented in section 3.5, which also includes the discussion on parameter estimate of the logistic curve solution for obtaining the D_{ij} function from microstructure.

3.4 Parameter Estimation

The major drawback of Corson's model 3.1 is the estimation process of the fitting parameters. As already pointed out, those parameters have no physical significance and have to be estimated for each new data set during regression analyses. The problem of fitting and estimating parameters is re-formulated here in the terms of the logistic model where the fitting parameters can be derived from microstructure morphology.

The presented logistic solution will be more natural than the one presented in the Corson's model if:

1. μ and σ can be fit to any microstructure based only on the material sample grain morphology,
2. μ and σ can then be re-used without any statistical pre-processing and parameter fitting for other samples and materials based on their grain morphology only. i.e. once the dependance of μ and σ on grain morphology is determined for one material then the form of the dependance can be used for any other material.

To illustrate how the statistical parameters μ and σ can be given a geometrical meaning based on the microstructure descriptors, the connection between grain morphology and parameters of the statistical functional model (Eq. 3.6) is examined below by treating the grains as the convex shapes with a log-normal distribution in the 2D space [83] and μ and σ representing the distance between grain centers of mass and average radius of each grain respectively.

Firstly, the distance statistics for each grain pair should be collected from the measured EBSD data. Magnesium and Aluminum data was randomly sampled by grain pairs and average distance was calculated for a different grain pairs (μ_t) as well as deviation from the average distance (σ_t- 'true'). After the a priori statistics for parameters is calculated, the a posterior estimates based on the grain morphologies was obtained and compared with a priory. Starting with a prior data, sample standard deviation(σ_t) was obtained from the measured data (σ_t) using:

$$\sigma_t = \sqrt{\left(\frac{1}{M_p}\sum_{i,j=1}^{M}(d_{ij}-\mu_d)^2\right)} \tag{3.9}$$

where μ_d is average distance between all the pixels pairs within fixed grain pair

$$\mu_d = \frac{1}{M_p}\sum_{i=1}^{M_p} d_{ij} \tag{3.10}$$

d_{ij} corresponds to the measured distance between each pair of points within a fixed grain pair, and M_p is the number of all pixel pairs within the particular fixed grain pair(in case if G_{p1} G_{p2} is the amount of pixels in grain G1 and G2 the M_p=$G_{p1} \times G_{p2}$). The calculated data for σ_t and μ_t - a prior measured estimates will be used next as major dependent regression variable, weather morphological estimates will be used as an independent ones.

For two, randomly chosen grains, it can be seen (Fig.3.7) that the variation in the distance between each pixel pair within two grains is related to variation of the distance between the grain centers. Figure 3.7 shows a schematic representation of the estimation process of μ and σ from the grain morphology.

Note, that centers of grains can be estimated, without any loss of information, by the geometrical center of mass of all coordinates with respect to the number of the points (EBSD pixels) inside the grain Eq. 3.11.

The center of the i^{th} grain is estimated as:

$$\langle C \rangle_i = \frac{1}{M} \sum x_k, k = 1..M \tag{3.11}$$

where x_k are the coordinates of the k^{th} point in the particular grain, and M is the number of points (EBSD pixels) within the grain. The deviation from the average distance μ can be expected to be a function of the individual radius of the two grains.

$$\mu_m = dist\left(\langle C \rangle_i, \langle C \rangle_j\right) \tag{3.12}$$

Standard deviation σ should depend logically on the grain shapes and average distance inside the grain (radius). Analyses of the data shows that σ is strongly dependent on the grain shape.

The first guess on σ estimation can be made that its linearly dependent on the grain radii for each of the particular grain pair. One can find linear coefficients to estimate σ based on this assumption using the linear regression model. From the experimental data σ_t can be found as the solution of the system of equations with unknown coefficients in the form:

$$\sigma_t = c_i r_i + c_j r_j + \epsilon_{ij} \tag{3.13}$$

where c_i are unknown coefficients, r_i, r_j are the radii of grains i, j, σ_t are the true deviation obtained from EBSD data (using Eq. 3.9), and ϵ_{ij} is an error term of the estimated solution. Radii (r_i and r_j) are calculated from the assumption that grains are orbicular so that:

$$r_i = \sqrt{\frac{sV_i}{\pi}} \tag{3.14}$$

where V_i is a the number of points inside the grain with index i and s is the EBSD step size. This approach has been found effective for a variety of grain sizes with microstructures having shape anisotropy up to 0.70 ($r_i min : r_i maj$). It should be mentioned that the analysis presented could easily be extended to grains having higher anisotropy by considering them as ellipses instead of spheres. This approach would require taking the radius of the grain as an average of each ellipsoidal major-minor axis (to take into account directional anisotropy of the microstructure). ($r_i = \frac{1}{2}(r_i maj + r_i min)$). The result for this type of anisotropic microstructure and morphological solution estimations will be shown in the next section.

Based on the grain structure the morphological deviation σ_m can be estimated using the coefficients $c_i = c_j = \frac{1}{2}$ with ϵ_{ij} (misfit between predicted on grain morphology and calculated from sample) being in admissible interval for approximation ($[0.1 : 7]$ %) for any grain pair. The radius for each grain can be calculated from the spherical equivalent radius of the grain with area V_i. Accordingly, the proposed relation to obtain σ_m is given by;

$$\sigma_m = \frac{1}{2}(r_i + r_j) = \sqrt{\frac{s}{4\pi}}(\sqrt{V_i} + \sqrt{V_j}) \tag{3.15}$$

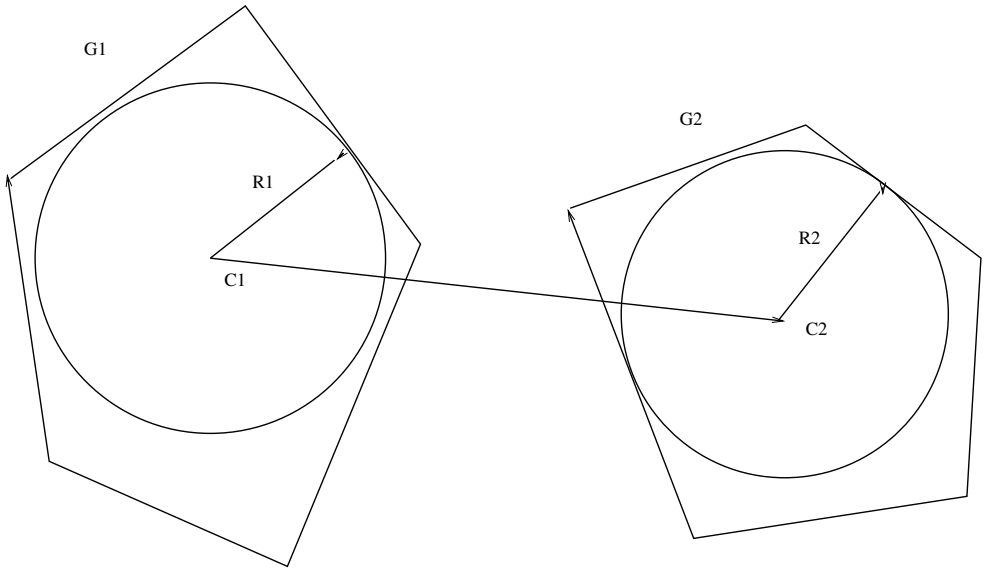

Figure 3.7: Visual representation of morphological estimations of the σ and μ between data pixel

where $\mathbf{V_{i,j}}$ represents the total amount of points in the grain with indices i, j and $\mathbf{s}$ is the EBSD step size. It is important to highlight the need of the morphological estimators for the proposed solution if one can calculate it out from the real data. To obtain morphological estimators you need to make 3 calculations - get the amount of point within each grain(V_i) - out of that you can directly calculate all the descriptors- average radii for each grain (r_i,r_j) and grain centers(C_{ij}). The differences between predicted and measured parameters (obtained from the EBSD data) for different grains are analyzed by constructing a linear regression model.

$$\sigma_t = \beta_1 \sigma_m + \epsilon_1 \tag{3.16}$$

$$\mu_t = \beta_2 \mu_m + \epsilon_2 \tag{3.17}$$

The regression model shows linear dependency between σ_t and σ_m as well as between μ_t and μ_m. Results of the regression model for the Magnesium sample ($1000 \times 1000 \mu m$) are presented in Figs. 3.8 and 3.9. The independent axes data for σ_t and μ_t obtained from the EBSD scan as a priory is showing a clear fit with estimated from the morphology (σ_m and μ_m). Aluminum data, not plotted for brevity, also showed similar results.

To give a quantitive data fit characterization the average error for the both fits was calculated. The resutls shown that the error for $\mu_m(\epsilon_1)$ is 0.5% and for $\sigma_m(\epsilon_2)$ is 7%, with linear fit coefficients (β_1 and β_2) close to 1. The error in σ_m measurement is higher due to the assumption that the grain shapes are spherical, as against having a random convex shape, while calculating the radii. The quality of the solution can be improved by improving mechanism to estimate the grain radii. Despite this, the proposed morphological estimators provides good prediction of the DDF curve as shown below. The comparison of D_{ij} obtained from the morphological parameters and the one calculated from EBSD data is presented in Fig. 3.10. The results show a very good match for a random grain pair selected from the micsostructure, proving the effectiveness of the new functional model.

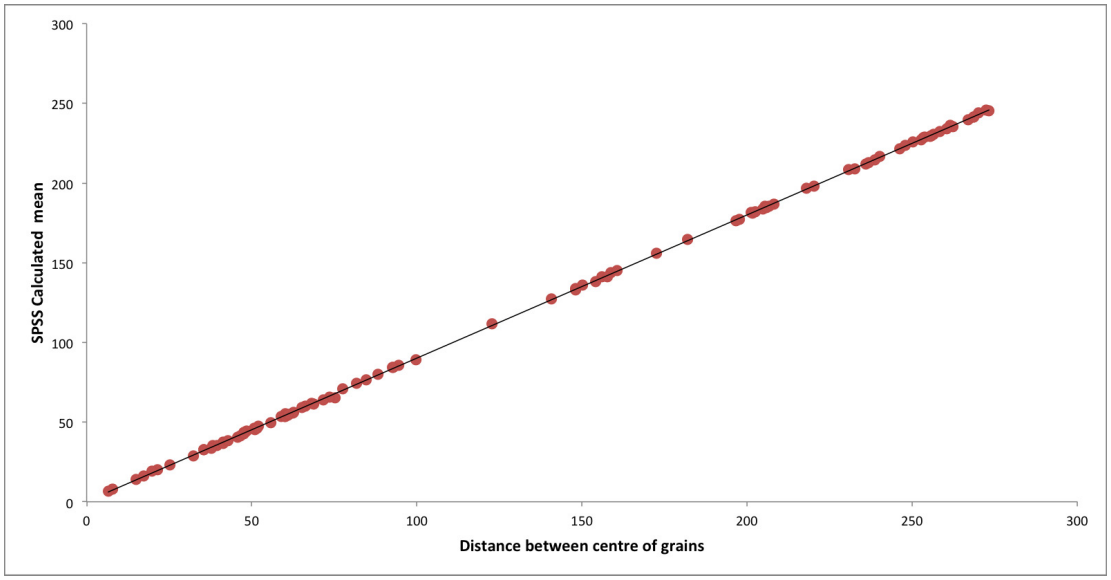

Figure 3.8: μ regression line fit plot for Mg data

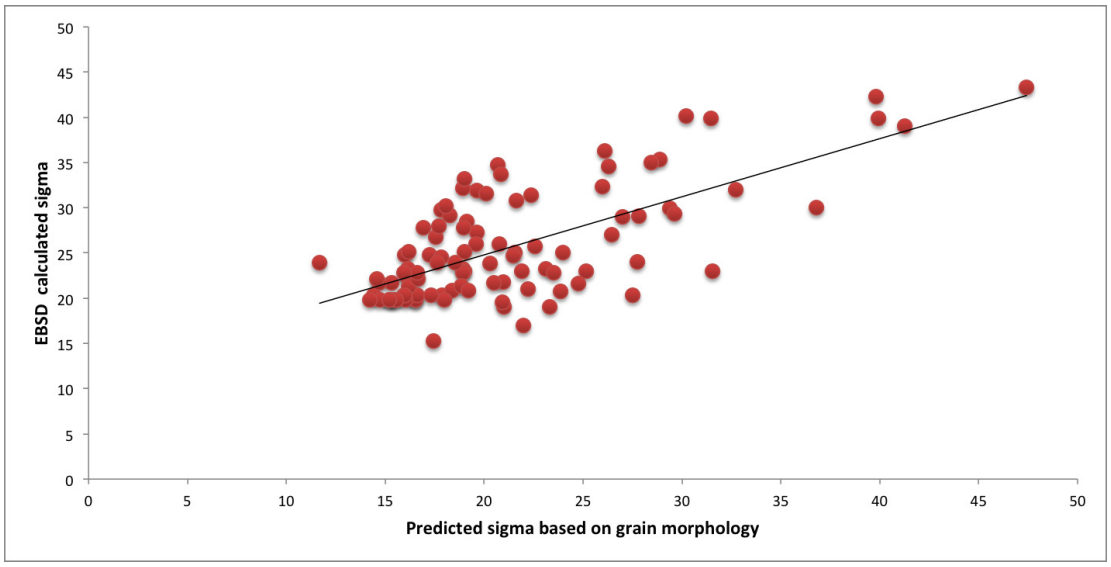

Figure 3.9: σ regression line fit plot for Mg data

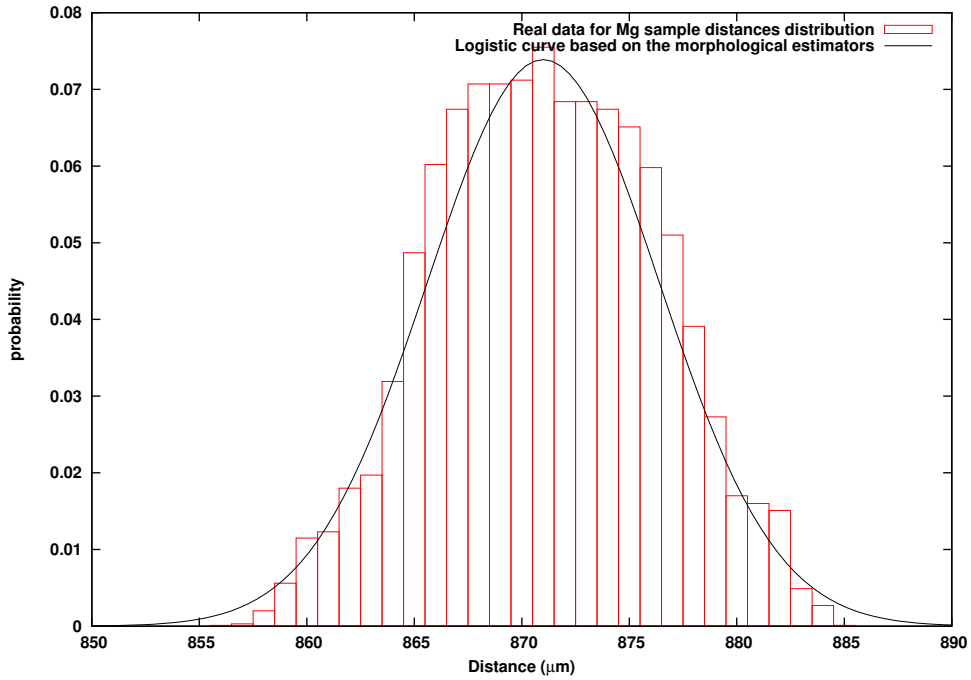

Figure 3.10: D_{ij} in micrometers constructed for the random grain pair in magnesium

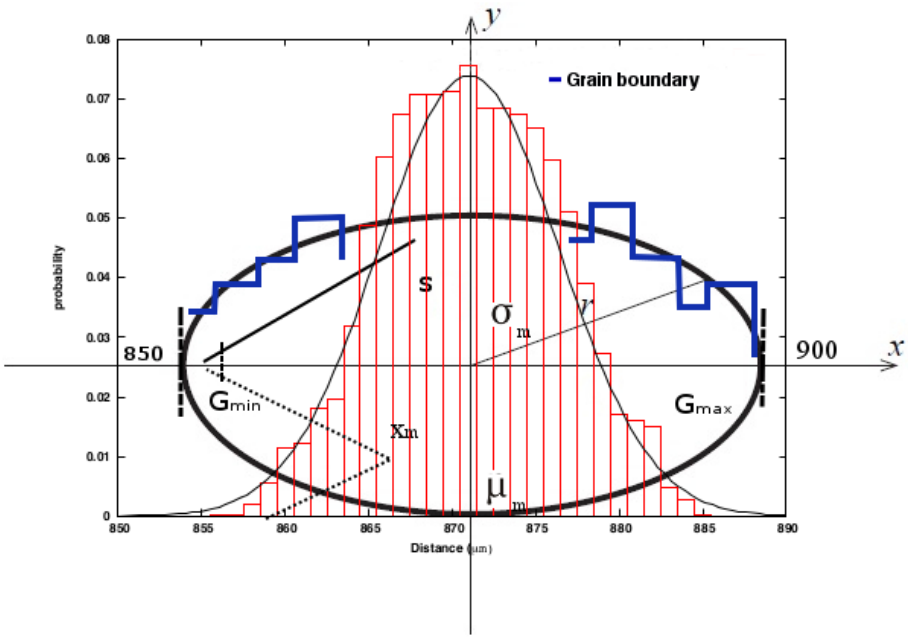

Figure 3.11: Morphological parameters of the analytical solution based on the single grain

When parameters σ and μ are estimated based on the grain morphology, the distance distribution function D_{ij} could be expressed, using Eqns. 3.8, 4.9 and 4.8, in the analytical form as:

$$D_{ij} = V_{ij} \frac{\pi s}{\sigma_m 4\sqrt{2}} sech^2 \left(\frac{\pi}{2\sqrt{3}} \frac{x_m - \mu_m}{\sigma_m} \right) \tag{3.18}$$

where μ_m and σ_m are the morphological estimators obtained above and x is the variable from the modelling interval. The set of distances x_m is populated from the any of two grains i and j as:
$x_m \in [G^i_{min} \dots G^i_{max}]$. The G^i_{min} corresponds to a left border of the principal axes of the elliptical grain estimation and G^i_{max} is a right border of the principal axes(G^i_{min},G^i_{max} are directly obtained from EBSD data) as shown in Fig. 3.11).

Each distribution generation point x_m in the discrete form is obtained as:

$$x^i_{m_{l+1}} = x^i_{m_l} + s \tag{3.19}$$

where l is a index set described as: $l = \{1..\frac{\lfloor G_{max} - G_{min} \rfloor}{s}\}$.

The proposed scheme for obtaining D_{ij} distribution based on the functional form in Eq. 3.18, besides being a mathematically compact representation of material characteristics, also gives a powerful tool for problems associated with microstructure modeling and characterization from the perspective of computational efficiency. The next section describes an application of the proposed model for obtaining

Distance-Disorientation Function [79].

3.5 Distance-Disorientation Function

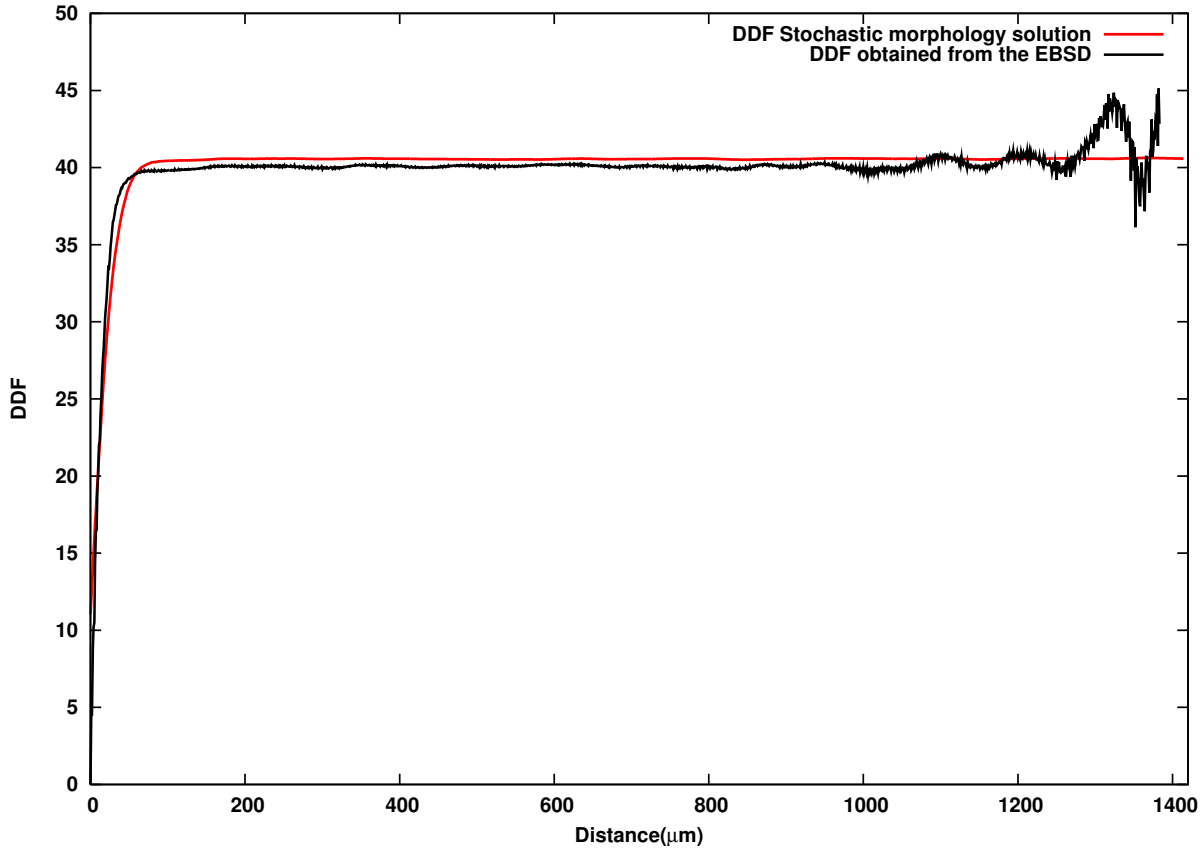

Figure 3.12: Aluminum DDF's for a $1000 \times 1000 \mu m$ sample

In this section, instead of calculating all distances within each cluster, the DDF is modelled by using the grain morphologies. Equation 4.3 is expressed as:

$$DDF = \frac{\sum_{j=1}^{N} \sum_{i=1}^{N} D^m \theta_{ij}}{\sum_{j=1}^{N} \sum_{i=1}^{N} D_{ij}^m} \tag{3.20}$$

D_{ij}^m is D_{ij} calculated by using the morphological parameters and is given by Eq. 3.18 as

$$D_{ij}^m = V_{ij} \frac{\pi s}{\sigma_m 4\sqrt{2}} sech^2 \left(\frac{\pi}{2\sqrt{3}} \frac{x_m - \mu_m}{\sigma_m} \right)$$

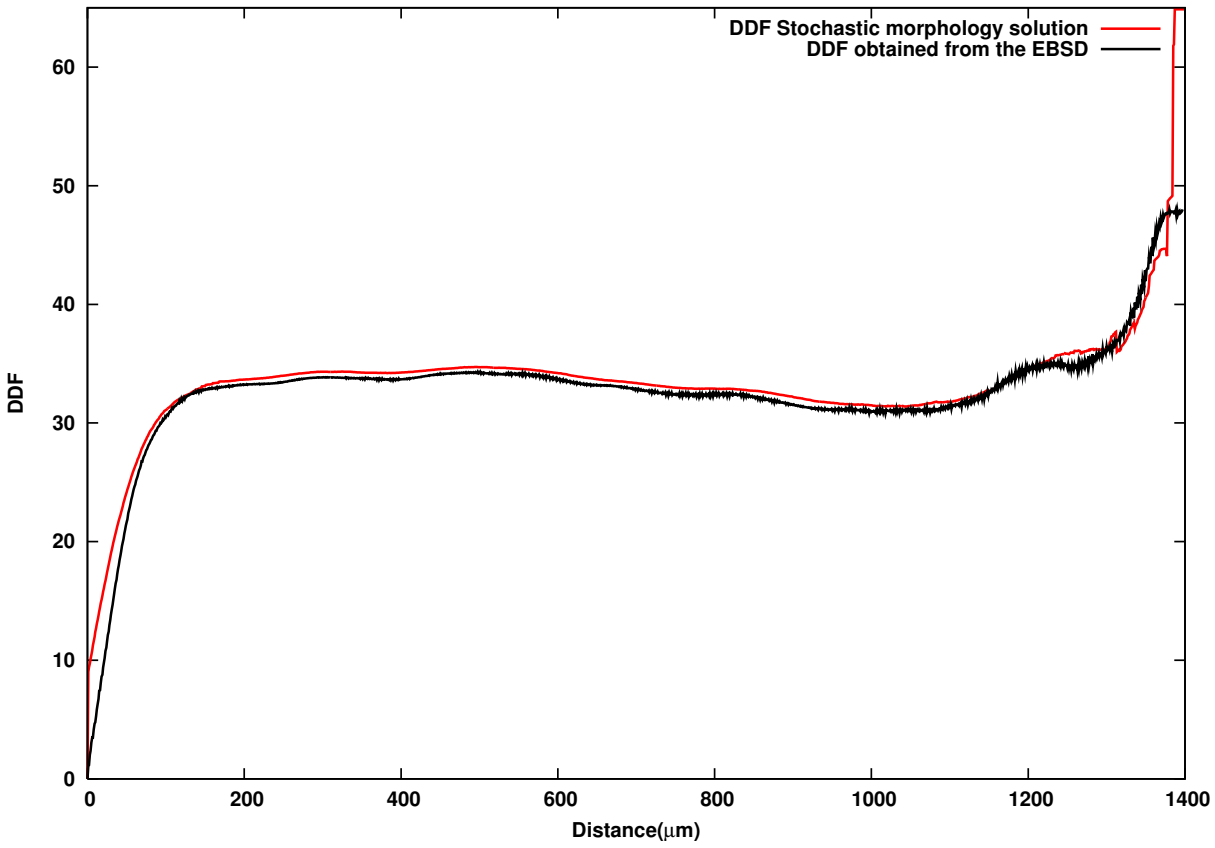

Figure 3.13: Magnesium DDF for a $1000 \times 1000 \mu m$ sample

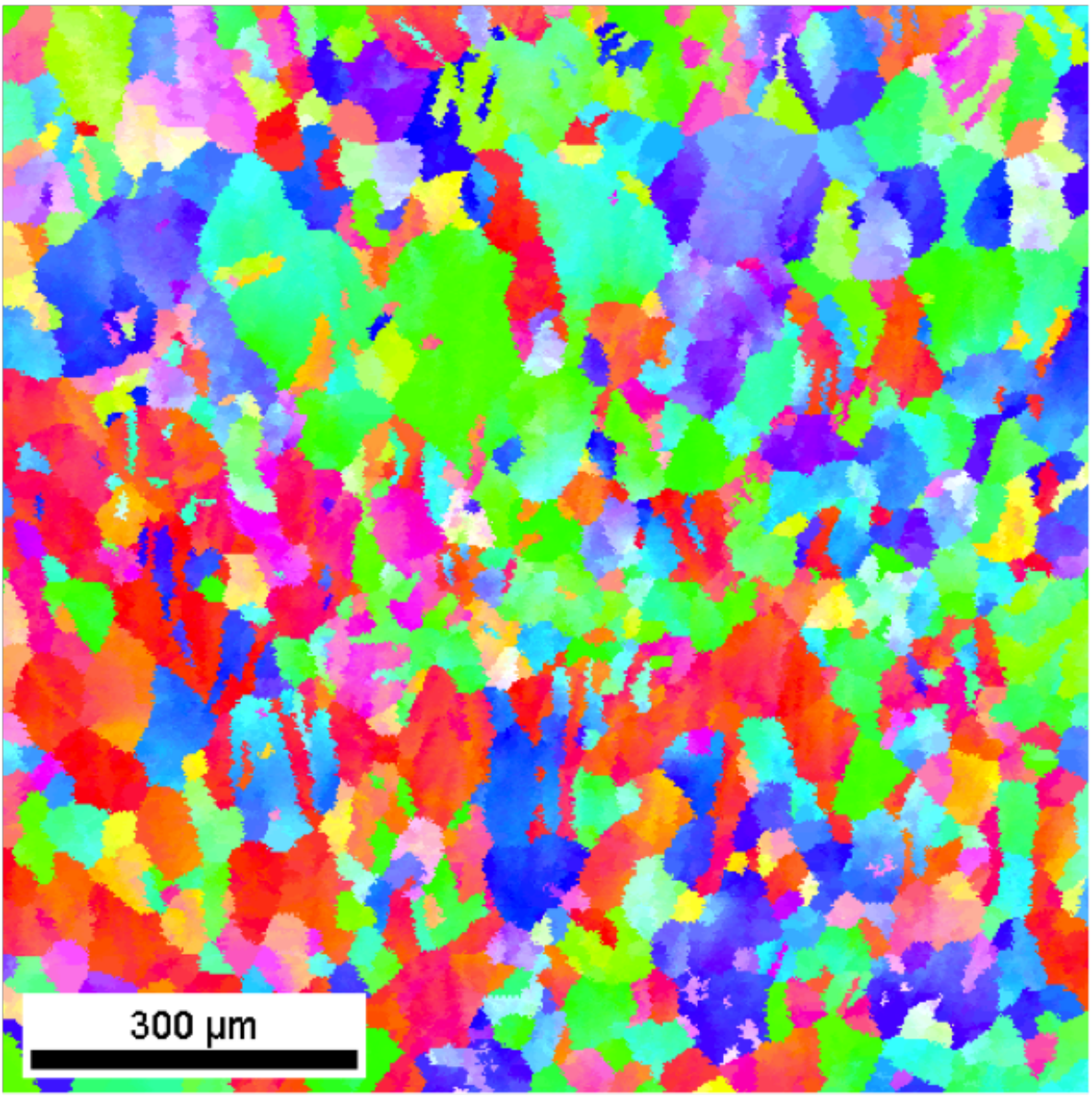

Figure 3.14: Magnesium 20% compression EBSD scan with high grain anisotropy in compression direction

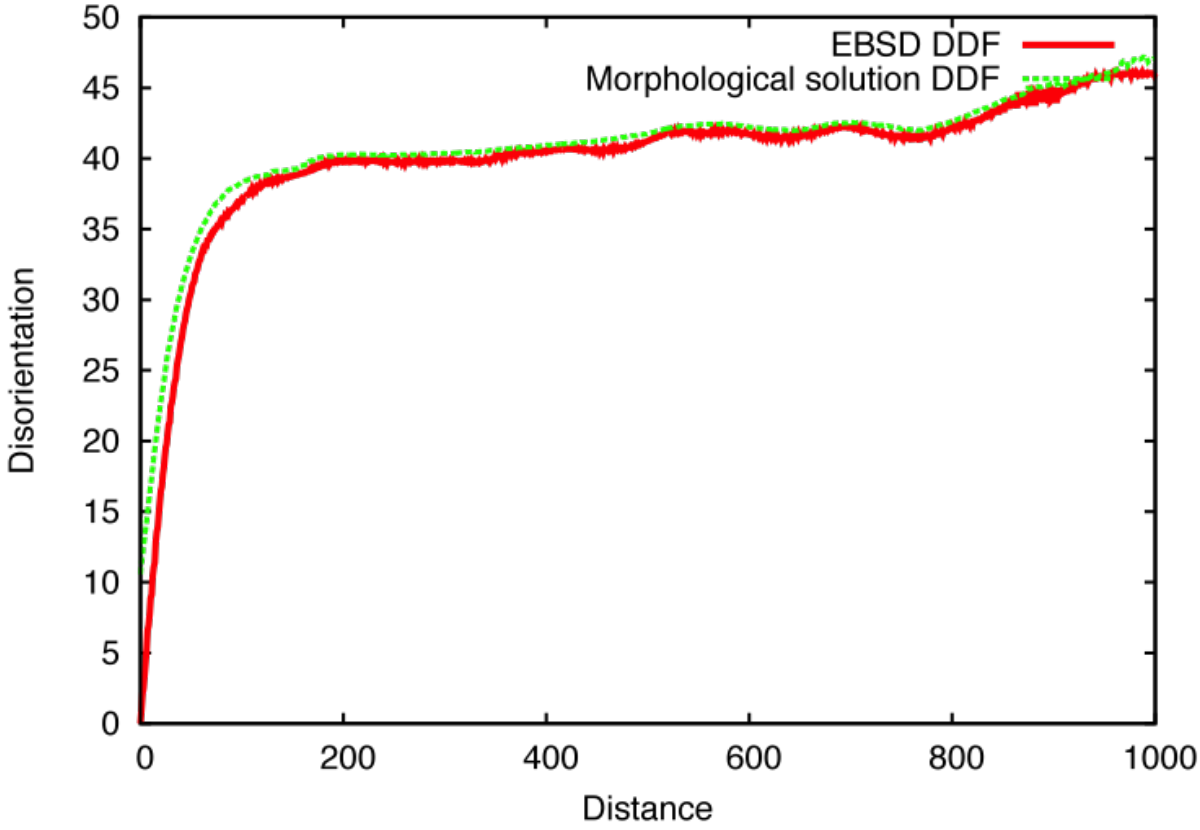

Figure 3.15: Magnesium DDF for a $1000 \times 1000 \mu m$ 20 % compression sample

D_{ij}^m is a logistically distributed random variable for a particular point x_m inside the grain, V_{ij} is the cross size of the grain pairs i and j and $V_{ij} = V_i \times V_j$. This product(V_{ij}) is the gain in efficiency for the each data cluster (grain) for distance calculation. Thus, instead of calculating the distances between each pixels within a given grain pair V_{ij} times, the logistic curve is modeled and then is only normalized for V_{ij}.

For the rest of the analysis in this work the normal curve will be used instead of the logistic curve to calculate the DDF for the EBSD to increase the computational efficiency[81]. In this study, instead of estimating the D_{ij} as a logistic curve, the same estimators used for logistic curve of σ and μ are employed:

$$D_{ij}^m = V_{ij} \frac{1}{\sigma_m \sqrt{(2\pi)}} exp\left(\frac{-(x-\mu_m)^2}{2\sigma_m^2}\right) \tag{3.21}$$

Eq. 3.18 is used to calculate the D_{ij} between a given pair of grains i and j. Similarly θ_{ij} can be obtained for the same pair. This procedure is repeated for all grain pairs in microstructure to obtain $\{D_{ij}\}$ and $\{\theta_{ij}\}$. Then using Eq. 4.3 the DDF for the entire microstructure is calculated. Figures 3.12 and 3.13 present the results of the DDF so calculated by using the parameters obtained from the morphology analysis. Both Magnesium and Aluminum data show good fit between calculated (using Eq. 4.3) and exact DDFs, using procedure outlined in section 3.3.1. The difference in the predicted and exact DDFs in the tail of the data on the right side is an artifact due to the corner and edge grains getting cut in the EBSD data. The step size (**s**) for Aluminum is $5\mu m$ while the average grain size (R) is around $25\mu m$. The step size for Magnesium is $2\mu m$ and the average grain size is $50\mu m$. Thus, for every pixel loss there is $\left(\frac{s}{R}\right)^2$ loss of information. For Aluminum this is $\frac{1}{25}$ while for Magnesium it is $\frac{1}{625}$. Thus, at the edges, there is more information loss in the Aluminum scan compared to the Magnesium scan. The DDF, calculated using the morphological parameters is comprised of $N \times N$ number of grain pairs. Each pair contributes a D_{ij}^m to DDF according to Eq. 3.20, and each D_m is logistically distributed. It is concluded since that DDF for the entire sample shows a good match with the exact DDF, the functional form proposed for D_{ij}^m (Eq. 3.18) is both robust and is statistically representative.

3.5.1 Computational efficiency

The proposed method significantly improves the computational efficiency to obtain the DDF. For example, for Mg data, the method provides a speed-up by a factor of 10^5 for the calculations of the distance between particular grain pairs (not including calculations of the grains morphologies). Thus for the entire sample, with the assumption of ~500 grains leading to 10^5 grain pairs, the speed-up would be a factor of 10^{10}. This speed-up in the estimate of the DDF enables integration of the DDF in modeling of microstructure, such as crystal plasticity finite element method (CPFEM)[33]. The proposed method takes less than a minute on an average (for $1000\mu m \times 1000\mu m$) sample on a personal computer (PC). The mismatch error between experimentally obtained (using EBSD) DDF and stochastically estimated DDF is less than 0.1% (estimated using the KL norm as described in [79]) which is significantly small compared to the errors presented in the work of Baniassadi *et al.*[23] who report the average error to be 8%.

3.6 Conclusions

In this research, a new functional form for the distance–disorientation distribution (DDF) is proposed and underlying theoretical considerations are discussed. The proposed framework is based on the de-coupling

of the crystallographic domain (treating it as an independent variable), and the geometrical domain for the two point correlation function. The crystallographic domain consists of the disorientations θ_{ij}, obtained from grain orientations $(\varphi_1, \phi, \varphi_2)$. The geometrical domain consists of grain morphologies and grain distributions inside the material. The analysis leads to the following conclusions:

(i) Statistical analyses show that data for D_{ij} is logistically distributed.

(ii) Logistic curve parameters were estimated based on the geometrical domain of the microstructure, obtained from EBSD, making this approach applicable to any material. The mean and deviation of the logistic distribution are the distance between grain centers d (Eq. 4.9), and average of the two grain radii $\frac{1}{2}(r_i + r_j)$ (Eq. 4.8), respectively.

(iii) For validation of the new theoretical model, the distance–disorientation function for Aluminum and Magnesium data were estimated using the new functional model. Comparisons between experimental (EBSD) DDF data and the DDF simulated from the probabilistic curve show good fit.

(iv) Functional solution based on the logistic curve and its morphological parameters reduces the computational complexity of obtaining the two-point correlation function and increases the efficiency by a factor of 10^{10}.

Chapter 4

On the reconstruction of the 3D representative volume element from the distance-disorientation correlation function

This chapter presents the application of 3D cross-correlation microstructure reconstruction implemented into a representative volume element (RVE) to facilitate microstructure engineering of materials. This has been accomplished by developing a new methodology for reconstructing three dimensional (3D) microstructure using experimental two dimensional (2D) electron backscatter diffraction (EBSD) data. The proposed methodology is based on the analytical representation of the generalized form of the two point correlation function – the distance disorientation function (DDF). The microstructure reconstruction is done by extending the simulated annealing techniques to perform a three term reconstruction with a minimization of the DDF. The new 3D microstructure reconstruction algorithm is employed to determine the 3D representative volume element (RVE) containing the relevant microstructure information for accurately computing the mechanical response of solids on the meso-scale(grain is a unit structure) level, especially when local microstructural variations influence global response of the material as in the case of fracture initiation.

4.1 Introduction

Solid state material behavior such as grain growth and recrystallization, fatigue and failure, etc [84, 85, 86] depend on the three dimensional microstructure characteristics. There is significant interest in obtaining accurate three-dimensional (3D) representation using experimentally measured data; however this is one of the most difficult material characterization problems. One of the important requirements for the reconstructed data is that it should be representative of the whole medium in so far as the physical properties of the material are concerned. The complexity comes from the problem of dimensionality of the reconstructed data and limitations of the experimental techniques for obtaining data.

Electron backscatter diffraction (EBSD) data provides a quantitative description of the microstructural features of solids with the limitation that most often the data is collected from two dimensional surfaces. New serial sectioning techniques and improvement of the computational resources have made it possible to obtain 3D EBSD data sets for certain materials. However, as it has been demonstrated in the works of [87, 79, 12, 28] that any 3D reconstruction must be based on in-depth studies of material properties and full understanding of the complexity of the existing cross-correlations in the material. [41] have described the qualitative characteristics of the data correlations obtained from the microscopy. They considered the nearest neighbor grain orientations, average volume fraction of the grain, texture and its correlation with grain or subgrain size, the spatial distribution of stored energy in a sample and the amount of recrystallized grains in the material for the 3D reconstruction. [42] work constitutes the general framework for the synthetic microstructure builder which was initially developed by [88] and discussed in details in ([43]). It is shown that there can be considerable differences in the results obtained from material modeling depending on what data is used and how the microstructure is reconstructed. Kanit et al. [89] have studied the effects of RVE size on the elastic and thermal material properties and shown that the variations in the RVE size can have significant effect on the computed properties. Finding the microstructure size that can accurately represent the mechanical response of the material is one of the important problems in the crystal plasticity finite element model (CPFEM) simulations [33] . Any realistic prediction with the CPFEM model requires accurate representation of the microstructure. There are various studies on the effects of microstructure representation on the micro and macro-mechanical predictions with CPFEM [90, 86, 85]. Significant amount of research has been reported on 3D microstructure reconstruction from correlation functions [15, 16, 17, 91, 20, 92, 21, 22]. A large variety of methodologies have been proposed, i.e., gaussian fields, cellular automata, simulated annealing, just to name a few. The main idea is to reconstruct the full microstructure from the n-point (or 2-point) correlation functions using different optimization and homogenization techniques. In the recent research works of Torquato group [37, 38, 39] the significant work was done in the field of the detailed characterization of the two point correlation function reconstruction mechanisms and its analyses. Torquato et al. in the latest studies [38, 39] highlighted the problem of the degeneracy associated with the two-point correlation statistics and shown valuable techniques for the solution of this complicated problem. Following Torquato et al. - degeneracy of the two point correlation statistics could be expressed in terms of the configuration entropy. As mention in the [38] all space transformations which keeps the distance constant such as translation and rigid rotation can provide the set of non unique microstructures with the almost identical two point correlation function measure. This types of the microstructures are called trivial. The focus of his particular research [38] was to classify and obtain a metric for the non trivial microstructures (could not be obtained from each other by any set of described transformations). The methodology of the solution for the non-triviality problems is based on the Monte-Carlo optimization techniques and minimization of the information content of the two-point correlation function statistics. The proposed study will focus on the

similar problems highlighted by Torquato et al. but from the different angle of view. Instead of analyzing the degeneracy of the two point correlation statistics for simplified two-phase systems, the problem of the non-trivial microstructure reconstruction will be treated as the problem of obtaining the microstructure with the representative volume which can be with a certain limitations accepted as the informatively full microstructure for the specific material. One of the established concepts of RVE is to provide the statistically representative domain of the whole microstructure which could be representative in the terms of specific properties according to the homogenization level and techniques. The latest concept of the weighted statistical representation of the microstructure (WSVEs) was formulated by [28] and [29]. The statistical representative element in the Niezgoda et al. formulation represents the element which could be randomly extracted from the material sample to represent certain properties, such as stress-strain response or specific elastic properties etc. The concept of RVE considered in this research represents the amount of grains, their cross-correlations and morphological features. The new method proposed below combines the known approaches of 2D image reconstruction based on the basic statistical descriptors with a new method for reconstructing the RVE from the 2-point correlation statistics ([87]). For the first time, the methods of functional form statistics is extended from the 2D EBSD case ([87]) to a 3D space using the same grain morphological analyses as for the 2D case. The optimization method developed by [43] as the basis to generate the 3D microstructure is followed. In ideal case, the representative volume element for a material depend upon the type of microstructure and material anisotropy (inhomogeneity in grain distribution and grains morphology, material imperfections, processing history etc.). A statistically homogenous material, with the grain size as a characteristic material unit, is assumed in this study. Representative scan size (RSS) of [79] is used for the two-dimensional experimental EBSD measurements. Once the 2D EBSD RSS is obtained, it is applied to the 3D reconstruction of an RVE. The improvement of the RVE reconstruction includes an additional effect due long range ordering (calculated through distance-disorientation function (DDF)). Using long range ordering in the calculation should reflect on the physical phenomena that are influenced by grain interactions (such as stress triaxiality). DDF is a generalized form of the two-point correlation function that includes already known and established nearest neighbor analyses statistics and misorientation distribution function statistics ([63]). DDF computes the average disorientation between two points while two-point correlation function correlates average probability for both points being in the same phase. DDF combines the misorientation distribution function (MDF)([93, 94]), orientation distribution function (ODF) ([95, 93]), statistical error minimization, and the cross-correlation effects of the distance-disorientation function statistics.

In this chapter, first the experimental EBSD data collected from the real material is presented. Then the DDF and analytical model implemented in the microstructure builder (m-builder) are discussed. The DDF minimization between real EBSD data and constructed 3D microstructure is the new optimization added to the existing simulated-annealing energy optimization model. This is followed by the construction of the mathematical model to improve the microstructure reconstruction algorithm.

4.2 Experimental data

The EBSD data used in this study was acquired from AA5754 aluminum sheet samples, using a LEO 1450 scanning electron microscope (SEM) fitted with a TSL EBSD camera. The EBSD data was analyzed using the TSL^{TM}OIM software (Ver. 4.6). The data was cleaned, using grain dilation method with single iteration, neighbor CI correlation and single orientation per grain, to remove the bad data points and only data points having a confidence index (CI) above 0.2 were retained for the analyses. Grains were

identified with a disorientation tolerance of 10°. Thus, the pixels having a disorientation of less that 10° were grouped together and identified as a grain. For the analyses, grains with less than 10 data points were excluded. Once grains were identified all the pixels in the grain were assigned average orientation of the grain. As a result, the disorientation of any two pixels within a grain is zero. The data was obtained from a direct chill cast and rolled aluminum sheet with grain size of $21.38\mu m$ and $23.94\mu m$ along the X and Y direction respectively. For this sample, the step size for the EBSD map was $5\mu m$ and the texture strength was 3.4. The number of grains in the scans was ∼8500 for the sample.

4.3 3D RVE reconstruction

The 3D RVE microstructure generation is broadly divided into two major components, grain structure generation and assignment of texture to the generated grain strain structure.

4.3.1 Grain structure generation

Crystal geometry was approximated based on the assumption that, for aluminum polycrystalline materials, grains shapes could be approximated by the ellipsoids [43]. Each ellipsoid could be completely defined by its semi axes:

$$\left(\frac{x}{a}\right)^2 + \left(\frac{y}{b}\right)^2 + \left(\frac{z}{c}\right)^2 \leq 1 \tag{4.1}$$

The procedure of grain structure genration inside the microstructure is based on the works of Saylor et. al[88] and Brahme et. al[43] and is based on the mechanism of fitting ellipsoids. Briefly, the procedure works by first generating a set of ellipsoids with given dimensions, which follows a set distribution. Out of these a subset is retained that gives the best volume filling and least overlap. Then using the centers of these ellipsoids as seeds the final grain structure is grown using a cellular automaton.

4.3.2 Texture assignment

Initial texture assignment to the generated microstructure is performed by assigning a random orientation to each grain. Using this texture assignment and experimental measurements for texture the ODF and MDF are calculated (f^m and $f^m(\Delta)$). The error term λ is calculated as the mismatch between the experimental data (f^e) and simulated (f^m) so that:

$$\begin{aligned} \lambda &= \sum_{i}^{i_{max}} \left(f^m(g)_i - f^e(g)_i\right)^2 + \\ &\quad \sum_{j}^{j_{max}} \left(f^m(\Delta g)_j - f^e(\Delta g)_j\right)^2 \end{aligned}$$

where i sums over the microstructure orientations and j sums over the misorientations. Note, that distribution function f is defined on g - a local state in a polycrystal (can be described in a Euler orientation space $\phi 1, Phi, \phi 2$) and Δg can be described for a neighboring crystals as a mismatch characteristics in a

Euler space(misorientation). This error term is usually associated with so called energy of the system for simulated-annealing [91] or Metropolis-Monte Carlo type optimization algorithms [96, 97] After the error λ or system energy is calculated, the next step is to minimize the mismatch between computed and experimental data. Metropolis-Monte Carlo approach for optimization is applied. An orientation change is employed randomly based on the given probability of success or failure of change of the error ($\Delta(\lambda) = \lambda^{i+1} - \lambda^{i}$) according to the given probability density function:

$$P = \begin{cases} 1 & \Delta\lambda \leq 0 \\ exp\left(\frac{-\Delta\lambda}{T}\right) & \Delta\lambda \geq 0 \end{cases} \tag{4.2}$$

where λ^{i} and λ^{i+1} are the errors calculated on the current (i) and next (i+1) iteration step and $\mathbf{T}$ is a temperature parameter controlled by the algorithm and usually described by the polynomial spline model. This optimization method, known as simulated annealing, is widely used in the problems of microstructure optimization [15, 16, 17, 20, 21, 22].

The microstructure reconstruction method proposed in this research is based on the distance-disorientation function analytical solution presented by [79] and [87]. Distance-disorientation function essentially provides a complete description of distance between any two points of microstructural data and the average disorientation between them [79]. The DDF represents the average disorientation (θ_{ij}) for all the pairs of pixels separated by a distance D_{ij}. This definition goes beyond the misorientation distribution function (MDF) [7] and the misorientation correlation function (MCF) as defined by [63]. The main concept of the analytical solution as mentioned before is to decouple the geometric domain and the crystallographic domain. in the following form:

$$f_{DDF} = \frac{\sum_{i=1}^{N}\sum_{j=1}^{N} D_{ij}\theta_{ij}}{\sum_{i=1}^{N}\sum_{j=1}^{N} D_{ij}} \tag{4.3}$$

where N is the number of grains in the geometric domain (microstructure). D_{ij} refers to a distribution of distances between a pair of pixels belonging to grains i and j respectively, and θ_{ij} refers to the disorientation between the average orientations of the two grains (i.e., $\theta_{ii} = 0$). Once the functional form of D_{ij} is obtained then the DDF can be calculated using Eq. 4.3.

The changes in proposed microstructure builder are based on the idea that grain morphologies and arrangement of the grains orientations in the polycrystalline material should be characterized not only by combination of the distribution of the volume fraction f(g) (ODF) and $f(\Delta g)$ (MDF) but also on the f_{DDF}. Using Information Theory and norms developed in the recent works of [79, 87] a new error term, λ^{DDF}, is introduced to the model of microstructure optimization. According to the results presented in the work of [79], to construct precise microstructure, instead of using EBSD scan of a random size representative scan size (RSS) data should be employed as initial input. Instead of calculating *ODF* and *MDF*; the mismatch between 3D reconstructed sample and EBSD the mismatch in the grain locations and their orientations (mismatch between *DDF* of 3D structure and *DDF* of RSS EBSD) are taken into account, so that;

$$\lambda^{DDF} = \sum_{k}^{\#pairs} \left|\left| f^{l}_{DDF}(g)_k - f^{RSS}_{DDF} \right|\right|_{KL} \tag{4.4}$$

where k is the sum over the all grains pairs. The new term f_{DDF} is a *DDF* correlation function for the 3D material microstructure and f^{RSS}_{DDF} is a DDF obtained for the material sample RSS. Figure 4.1 presents

a schematic representation of the 3D microstructure reconstruction with different statistical estimators collected from the EBSD data (*MDF*, *ODF* and *DDF*).

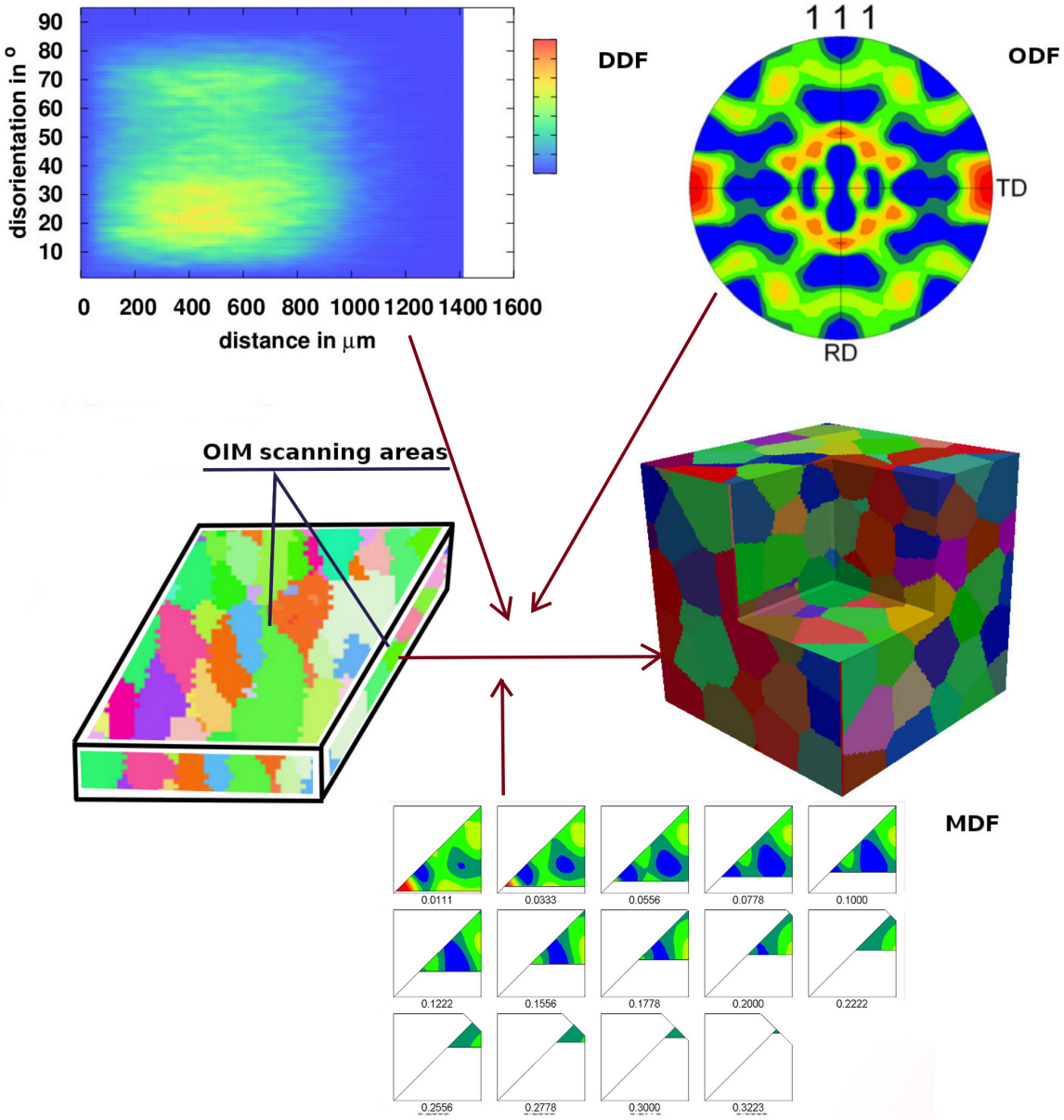

Figure 4.1: Global procedure of the 3D synthetic microstructure reconstruction. ODF, MDF and DDF are used as inputs to construct the 3D microstructure from the 2D scan area.

The comparison between the two *DDF's* - for the RSS of Aluminum (500× 500 μm) data and

(200×200× 50 μm) *DDF* 3D reconstructed without *DDF* optimization data are presented in the Fig. 4.2.

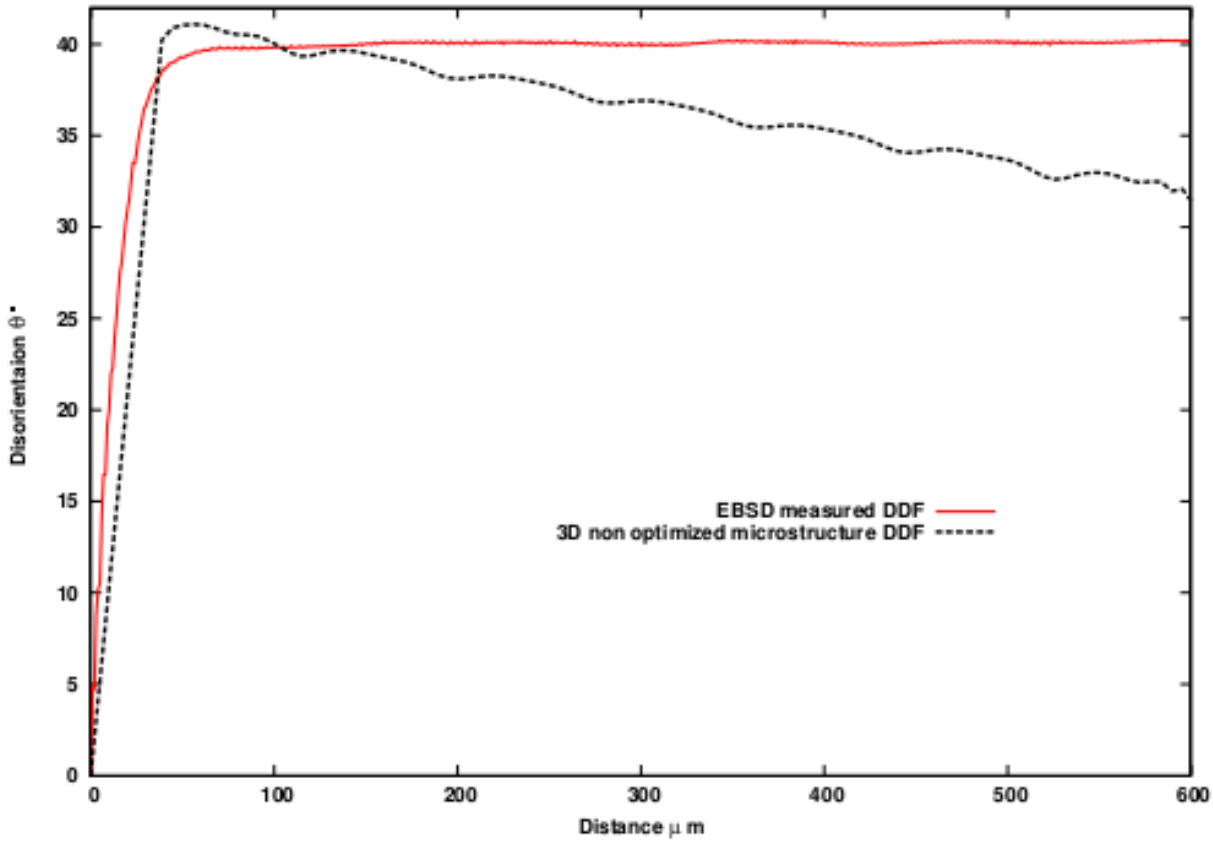

Figure 4.2: DDF's for the EBSD sample ($500 \times 500 \mu m$) and for non optimized 3D microstructure ($200 \times 200 \times 50 \mu m$)

As it can be seen from the Fig. 4.2 the non optimized microstructure shows deviations from the RSS EBSD *DDF*. The proposed solution for the 3D microstructure reconstruction is based on removing this gap. λ^{DDF} is the loss of information, in terms of the distance disorientation function, between measured EBSD and 3D reconstructed data. The norm for the error approximation that will be used in this work is a norm defined in the study of [79]:

$$D_{KL}\left(I_{\Omega_{EBSD}}[i], I_{\Omega^T}[i]\right) = \sum_{i=1}^{n} I_{\Omega_{EBSD}}[i] \ln \frac{I_{\Omega_{EBSD}}[i]}{I_{\Omega^T}[i]} \tag{4.5}$$

where $I_{\Omega^T}(f_{DDF}$ for the problem) is the information statistics gathered from each iteration of the 3D optimization algorithm. $I_{\Omega_{EBSD}}$ (f_{RSS} for the problem) is the cross-correlation information obtained from the representative scan size EBSD material sample. The is measuring statistical mismatched between the

2D and 3D data, however this is the valid statistically homogenized microstructure constraint commonly used in community. Each calculation of the *DDF* for the 3D microstructure requires calculations of more than 10^{15} distances. In case of the extreme ratio of data dimensions, the functional form of *DDF* should be used in order to calculate cross correlation function in 3D. After each step, when texture components are updated, the *DDF* mismatch between RSS and 3D sample needs to be recalculated using the functional form:

$$f_{DDF} = \frac{\sum_{j=1}^{m}\sum_{i=1}^{n} f_{mrph}^{ij}\theta_{ij}}{\sum_{j=1}^{m}\sum_{i=1}^{n} N_{ij}} \tag{4.6}$$

where

$$f_{mrph}^{ij} = V_{ij}\frac{1}{\sigma_m\sqrt{(2\pi)}}exp\left(\frac{-(x-\mu_m)^2}{2\sigma_m^2}\right) \tag{4.7}$$

In the given functional form, σ_m and μ_m are morphological estimators of the grains inside the microstructure. According to [87] the estimators for the σ_m can be obtained by:

$$\sigma_m = \frac{1}{2}(r_i + r_j) = (\frac{3s}{4\pi})^{\frac{1}{3}}(V_i{}^{\frac{1}{3}} + V_j{}^{\frac{1}{3}}) \tag{4.8}$$

where $V_{i,j}$ represents the amount of points in the grain with indices i,j and s is the EBSD step size. The deviation from the average distance μ_m was estimated accordingly to [87] without *DDF* optimization and can be extended to a 3D space as:

$$\mu_m = dist\left(\langle C\rangle_i, \langle C\rangle_j\right) \tag{4.9}$$

the center of the i^{th} grain (C_i) is estimated as:

$$\langle C\rangle_i = \frac{1}{m}\sum x_k, k = 1..m \tag{4.10}$$

where x_k are the coordinates of the k^{th} point in the particular grain, m is the number of points within the 3D grain, μ_m is a distance between ellipsoids centers and σ_m is an average of the ellipsoids radii. The visual representation of the morphological estimators of distance-disorientation function is presented in the Fig. 4.3. In this figure ellipsoids represents the two randomly picked grains with different orientation in the 3D microstructure. Now the λ_{DDF} term can be recalculated in the form of the new methodology as:

$$\lambda^{DDF} = \sum_{k}^{\#pairs} \left|\left|f_{DDF}^{l}(g)_k - f_{\Omega_{RSS}}\right|\right|_{KL} = \sum_{i=1}^{n} f_{\Omega_{RSS}} \ln\frac{f_{\Omega_{RSS}}}{f_{\Omega_{DDF}[i]}} \tag{4.11}$$

where is the $f_{\Omega_{RSS}}$ is the DDF information statistics gathered from the 2D representative scan size (500×500), and $f_{\Omega_{DDF}[i]}$ is the information statistics gathered from the 3D scan at the each algorithm iteration i.

The functional form of *DDF* captures various important microstructural characteristics that are intrinsic to the material. As discussed in [87] the functional solution is captures the morphological aspects of the grains within the structure:

1. local anisotropy of the grain morphology - the higher is a mismatch of the geometrical estimator - the more mismatch in the functional estimator.

2. anisotropy in the grain location in a 3D space (alignment of the grains in the space)
3. effects of the EBSD step size on the quality of the estimator(the smaller step size produces better estimators of the distance- disorientation function)

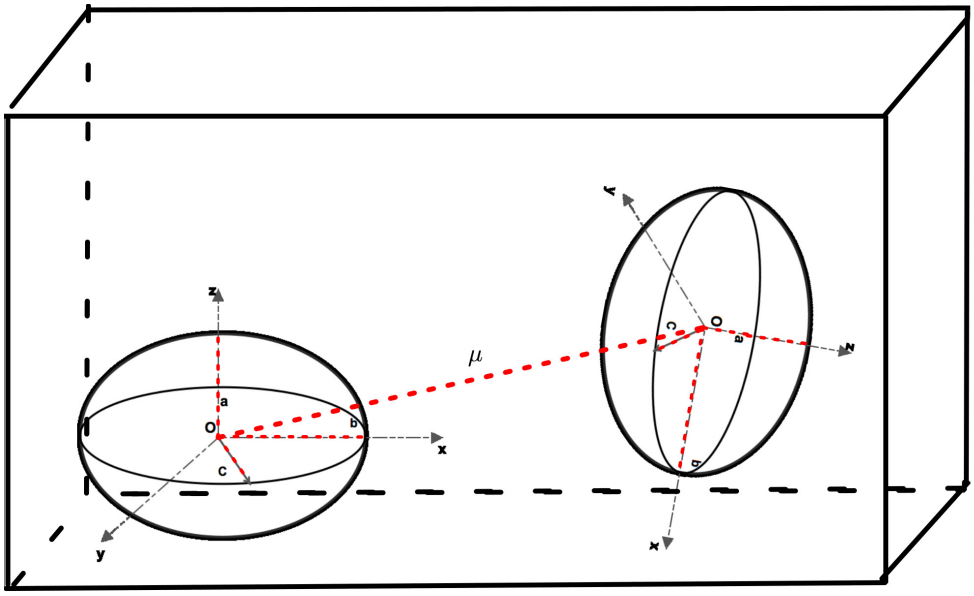

Figure 4.3: Visual representations of the morphological estimators (in red) of the distance-disorientation function in a 3D space

After the functional form and the new optimization term is defined, the total error of the system to be optimized through a simulated annealing algorithm takes the form:

$$\lambda_{total} = \sum_{i}^{i_{max}} \left(f^m(g)_i - f^e(g)_i\right)^2 + \tag{4.12}$$

$$\sum_{j}^{j_{max}} \left(f^m(\Delta g)_j - f^e(\Delta g)_j\right)^2 + \tag{4.13}$$

$$+ \sum_{i=1}^{n} f_{\Omega_{RSS}} \ln \frac{f_{\Omega_{RSS}}[i]}{f_{\Omega^T_{DDF}}[i]} \tag{4.14}$$

The error evolution according to the new optimization schema is shown in the Fig. 4.4. Note that the error optimization control mechanism for the new procedure provided a good convergence rate for both total amount of success steps and DDF optimization as well.

The procedure of *DDF* optimization while optimization step is presented in the Fig. 4.5. The convergence of the *DDF* is clearly seen for each optimization step. The successful step brings down the curve

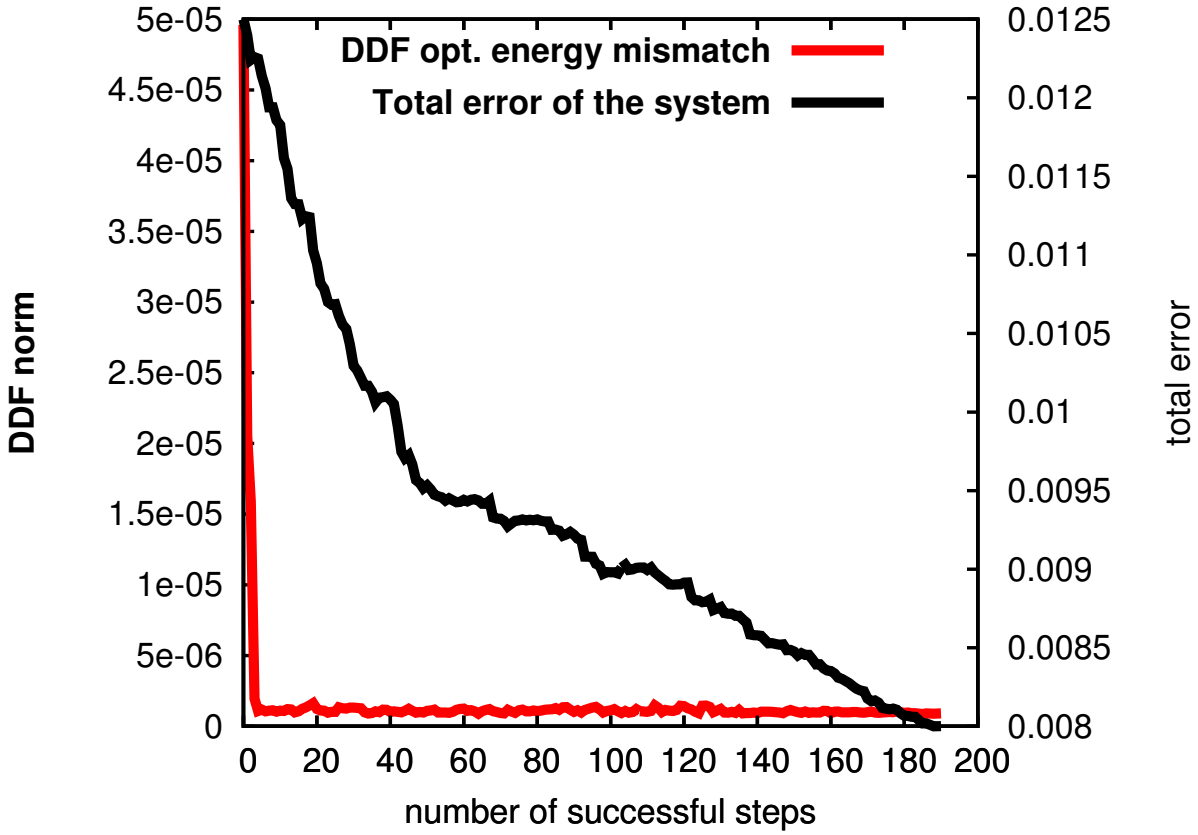

Figure 4.4: Error control with the new f_{DDF} term due to Monte Carlo optimization

from the initial value to the optimized value. Comparison of the results of the new 3D microstructure modeling (sample size $200 \times 200 \times 50 \mu m$) and old microstructure, for the aluminum DC sample procedure are presented in Fig. 4.6. It can be seen that, effect of the distance-disorientation minimization changes the texture. It was shown in the work of [79] that the *ODF* is not enough to describe all the texture cross correlations which exist inside the material sample. The algorithm of optimizing *DDF* in the 3D microstructure in the simple description is re-ordering grains inside the structure close to their location. This leads to optimized microstructure having relatively the same percentage of the main texture components (main orientations).

As it can be seen from Fig. 4.7, the locations of the grains (starting from the nearest neighbors and including long range correlation effects) are different. The differences in a neighbor grain locations are highlighted by the smaller arrows to show that grains with similar orientations and misorientations in both microstructures have switched their locations on the local scale. The global change (between two microstructures) in the orientations of the grains are highlighted by larger arrows. It can be seen that, statistically the same components are represented in both of the microstructures, which is logical due to *ODF* minimization with the same EBSD data, however there are variations in the grain locations inside the material and their local texture-component correlations as well.

4.3.3 RVE construction

In this section the problem of the RVE and application of RVE are discussed. Note that problem of constructing 3D microstructure that have always been linked with the number of crystallographic textures should be taken to obtain the optimal representative minimum volume element (that can store all relevant texture information within a certain domain of interest). If the minimum block can be constructed than it can be used to build a microstructure of any size with representative texture information. The scale where the representative texture will be searched is limited to the meso scale of the material microstructure. Thus the unit structure which represents the material is a grain. For the specific case presented in this research the range fot the grain size is $20-50 \mu m$ - the minimum and maximum grain size for the aluminum AA5754DC.

The procedure of reconstruction of the RVE (see Fig. 4.12) is based on finding optimal dimensions $(x_{opt}, y_{opt}, z_{opt})$ of the 3D building block which satisfies the minimization of the information norm mismatch between RSS and synthetic microstructures so that:

$$x_{opt}, y_{opt}, z_{opt} \in \{x, y, z\} : \lambda^{DDF} = \sum_{i=1}^{n} f_{\Omega_{RSS}} \ln \frac{f_{\Omega_{RSS}}}{f_{\Omega^{T}_{DDF}}[i]} < \epsilon \tag{4.15}$$

where ϵ is a parameter which determines the convergence of the minimization mismatch. The ϵ value for convergence of KL norm for each subscan is based on the full information sample of the particular material (in the present case $500x500 \mu m$ for Al 5754 RSS) and is material dependent. Table 4.1 summarizes all the terms and their definitions used to identify the RVE.

The ϵ value is the information mismatch (optimal $\epsilon = 5 \times 10^{-6}$ is chosen from the work of [79]) between the 3D microstructure with certain test dimensions(randomly chosen) and obtained representative scan size (RSS). Thus, obtaining an RVE is a two step procedure; (i) obtain an RSS for a given material (using Brahme et al methods) and then we extend them to a 3D case to obtain an RVE.

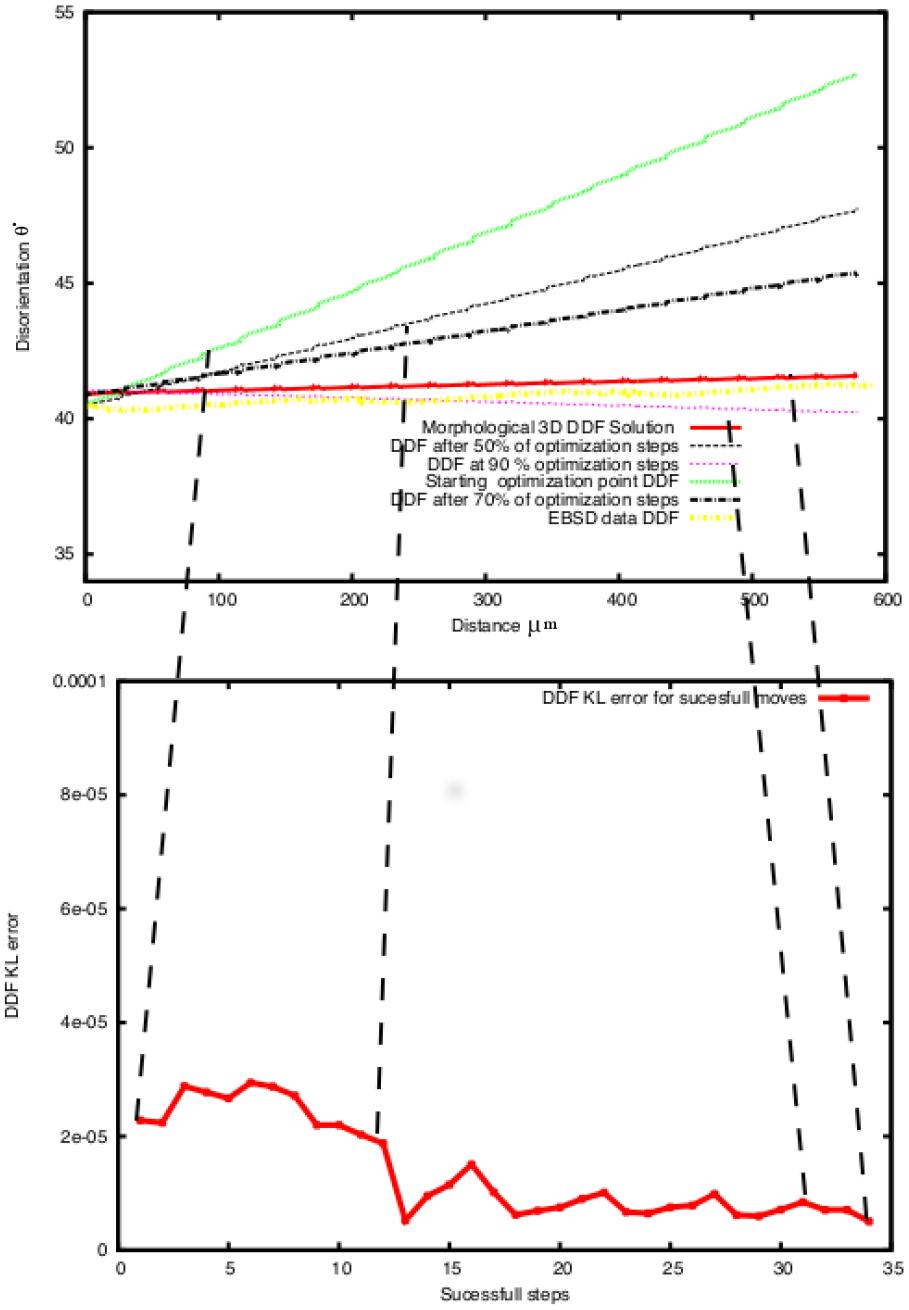

Figure 4.5: DDF curves behavior due to simulating annealing optimization $200 \times 200 \times 50 \mu m$ microstructure

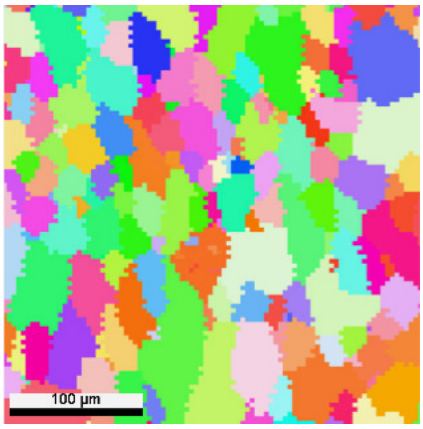

(a) initial microstructure

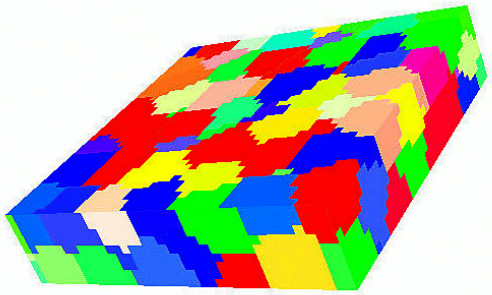

(b) DDF non optimized microstructure

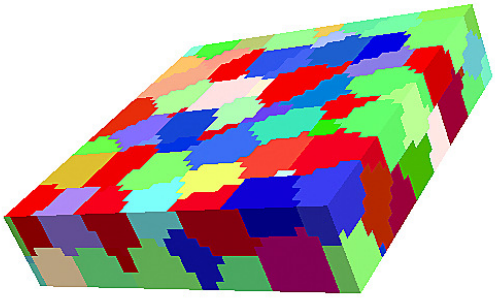

(c) DDF optimized microstructure

Figure 4.6: Comparing of the micro structures ($200x200x50\mu$ m) with and without DDF control.

Table 4.1: Terminology

Symbols	Significance	variables
θ_{ij}	Disorientation between pixel pair i and j	$(\text{Euler angles})_{i,j}$
D_{ij}	distance between the pixels	x_i and x_j
$f_{\Omega_{RSS}}$	EBSD DDF data for representative scan	$\{(\text{Euler angles})_i, x_i\}$
$f_{\Omega_{DDF}}$	DDF data for 3D microstructure	$\{(\text{Euler angles})_i, x_i\}$

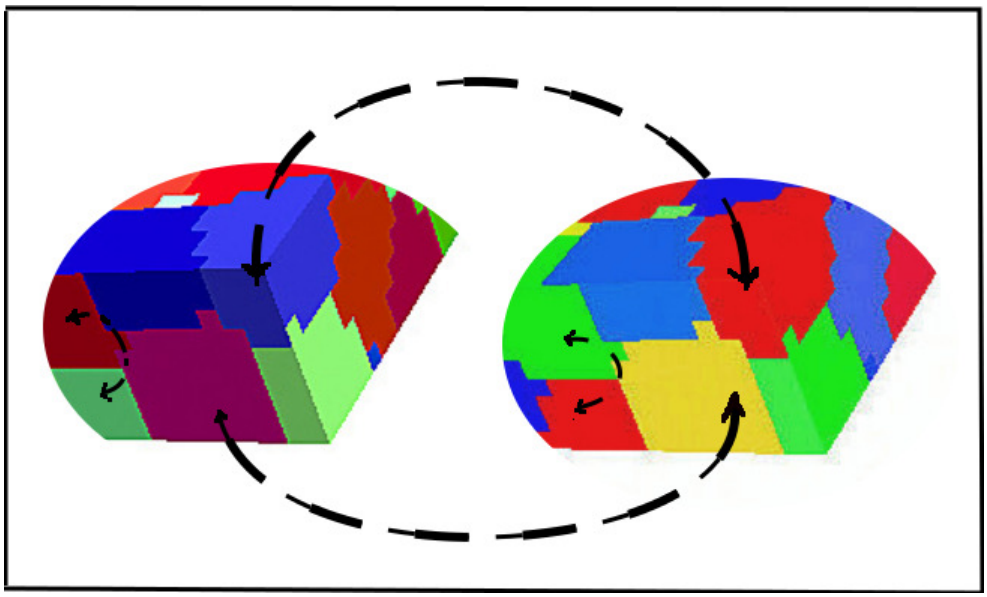

Figure 4.7: Changes in the two microstructures after optimization.

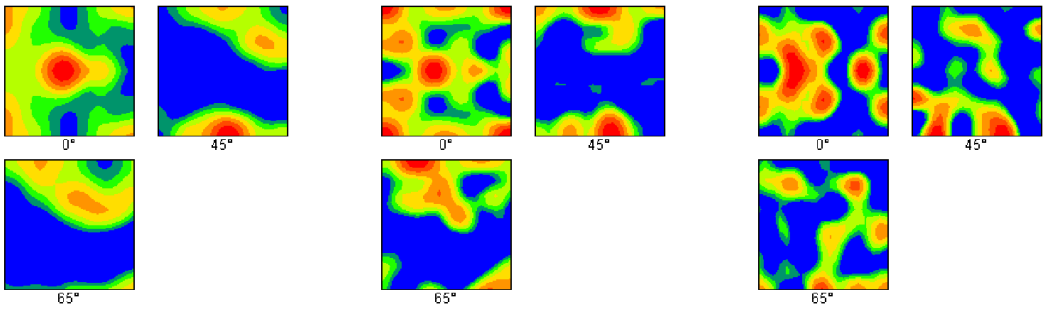

(a) initial EBSD microstructure *ODF*

(b) non optimized microstructure *ODF*

(c) optimized microstructure *ODF*

Figure 4.8: Comparing of the *ODF's* (200x200x50 μ m) with and without DDF control of initial microstructure *ODF*.

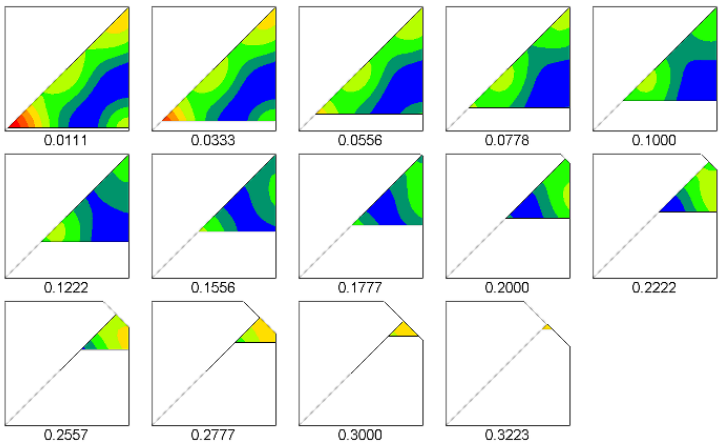

Figure 4.9: initial EBSD microstructure *MDF*

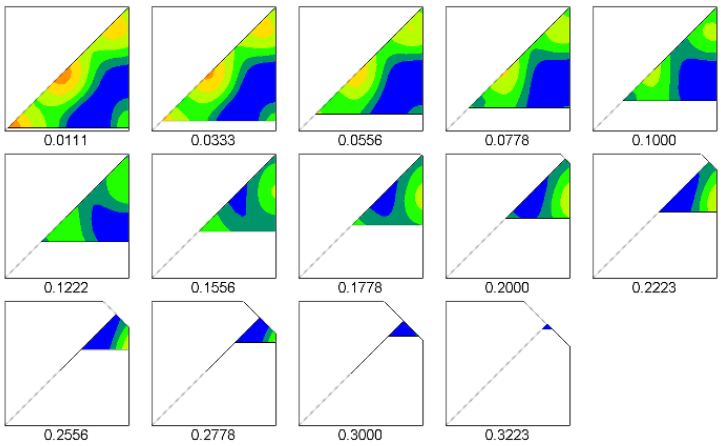

Figure 4.10: non optimized microstructure *MDF*

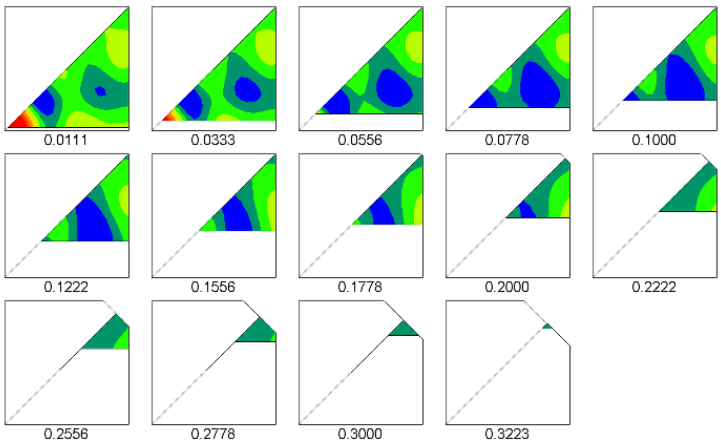

Figure 4.11: optimized microstructure *MDF*

Starting from an initial small box $20 \times 20 \times 20\mu m$ with a certain step, the optimal dimensions $(x_{opt}, y_{opt}, z_{opt})$ need to be determined that it minimizes the KL entropy norm between DDF of the RSS data and DDF of the 3D reconstructed data.

The cross-correlation statistics between the reconstructed microstructure and the measured EBSD data is compared until the acceptable convergence (5×10^{-6}) of the information norm is achieved. Then the obtained dimensions, which gives the same small constant KL entropy value are chosen to be a representative for a volume element. The procedure which is applied for validation of the RVE was initially presented by [79] for finding RSS and applied the original methodology to the third dimension.

4.3.4 RVE characterization

The characterization of the RVE was performed by analyses of the cross-correlation (DDF) between optimized and non optimized microstructures was done by separating them into different microstructural categories.

Table 4.2: Table of the base microstructures considered: representative scan size (RSS), RVE size optimized 3D: M^{per}, periodic non optimized 3D: M^{nper}, non optimized 3D microstructure: M^{pnopt}

Microstructure	Dimensions(μm)	Grains	Avg. Grain Size	Elements
RSS	500x500	513	25	250000
M^{opt}	200x200x50	215	23.1	16000
M^{per}	600x600x150	3200	23.1	432000
M^{nper}	600x600x150	3200	25.1	432000
M^{pnopt}	600x600x150	3200	23.1	432000

The table 4.2 shows the microstructures for the validation and RVE characterization (dimensions and numbers vary from material to material). These categories are formal and used in the research to

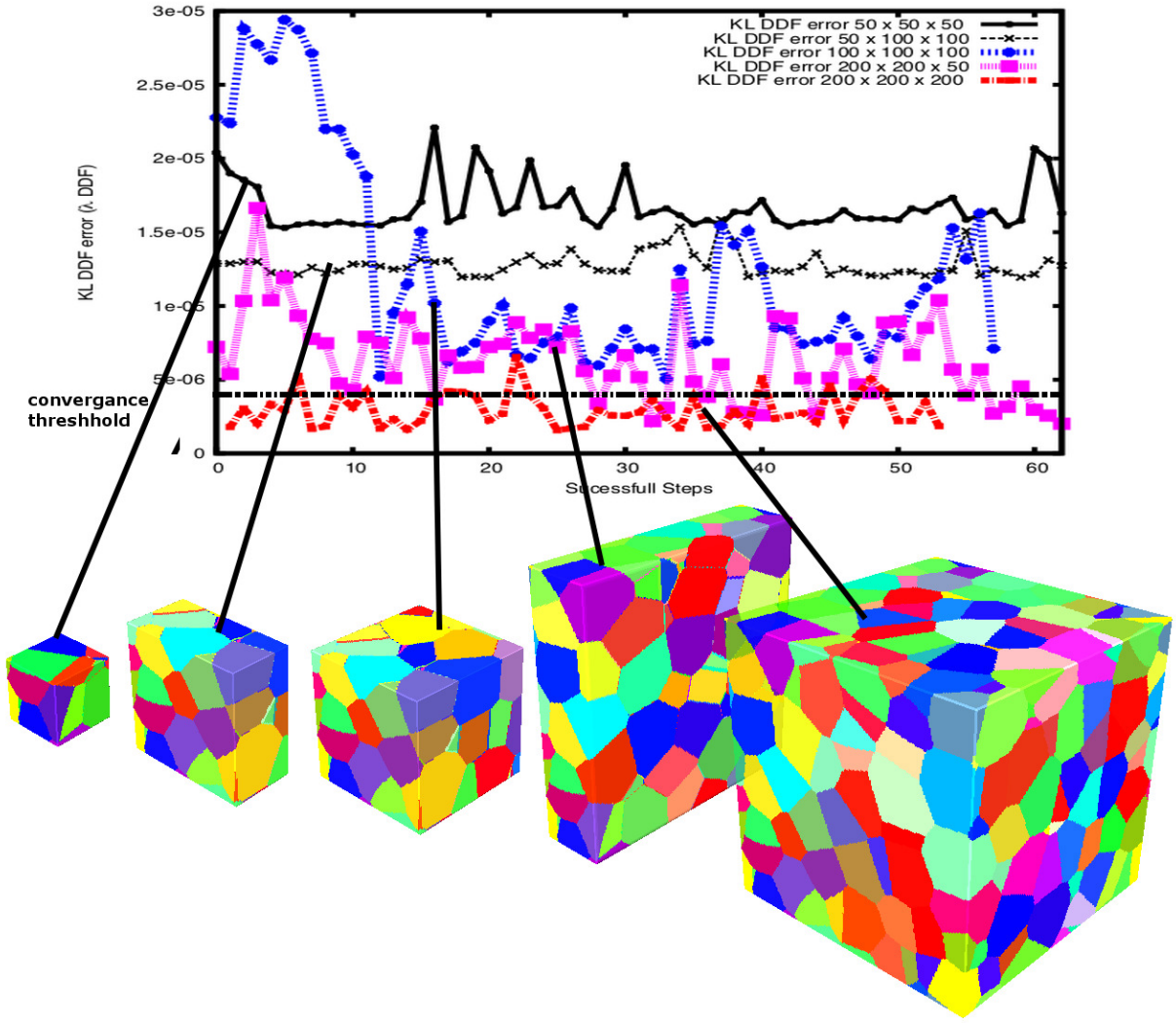

Figure 4.12: Procedure of obtaining optimal dimensions of the representative volume element

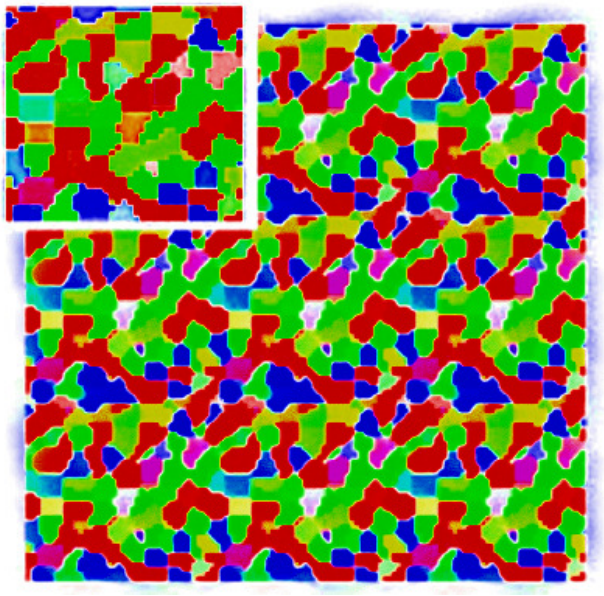

Figure 4.13: Construction of the periodic microstructure of any size based on the RVE building block.

show differences or similarities in the cross-correlations for optimized and non optimized microstructures. Periodic structures are suggested as a point of interest of reconstruction (from the RVE). The procedure of the microstructure characterization is based on the comparison of the RVE microstructure with the larger periodic microstructures and smaller microstructures that were not optimized. The main hypothesis of design is that the non-optimized 3D microstructure should show higher DDF information mismatch. The following key steps are proceeded to validate the different 3D microstructures.

1. Join microstructures periodically to build a relatively larger size periodic microstructure.
2. Obtain DDF statistic for different types of the microstructures.
3. Construct DDF statistics functions for the microstructure.
4. Check (for each microstructure) the DDF of the 3D microstructures from the stitched RVE's should match stitched microstructure that is not optimized should not match the experimental EBSD DDF curve as well as the RVE DDF.

The DDF curves obtained for the designed microstructure are presented in the Fig. 4.14. The results show that (Fig. 4.14) the optimized RVE microstructures consist the same amount of information as larger periodic microstructure and 3D microstructure from the non optimized building block does not capture all information.

The results show that DDF curves of the microstructure constructed from the RVE blocks match with the DDF of the experimental data and the large 3D microstructure that is not optimized(green, blue curves Fig. 4.14). The measured KL entropy norm between optimized 3D RVE blocks is the order of 10^{-6} [79]

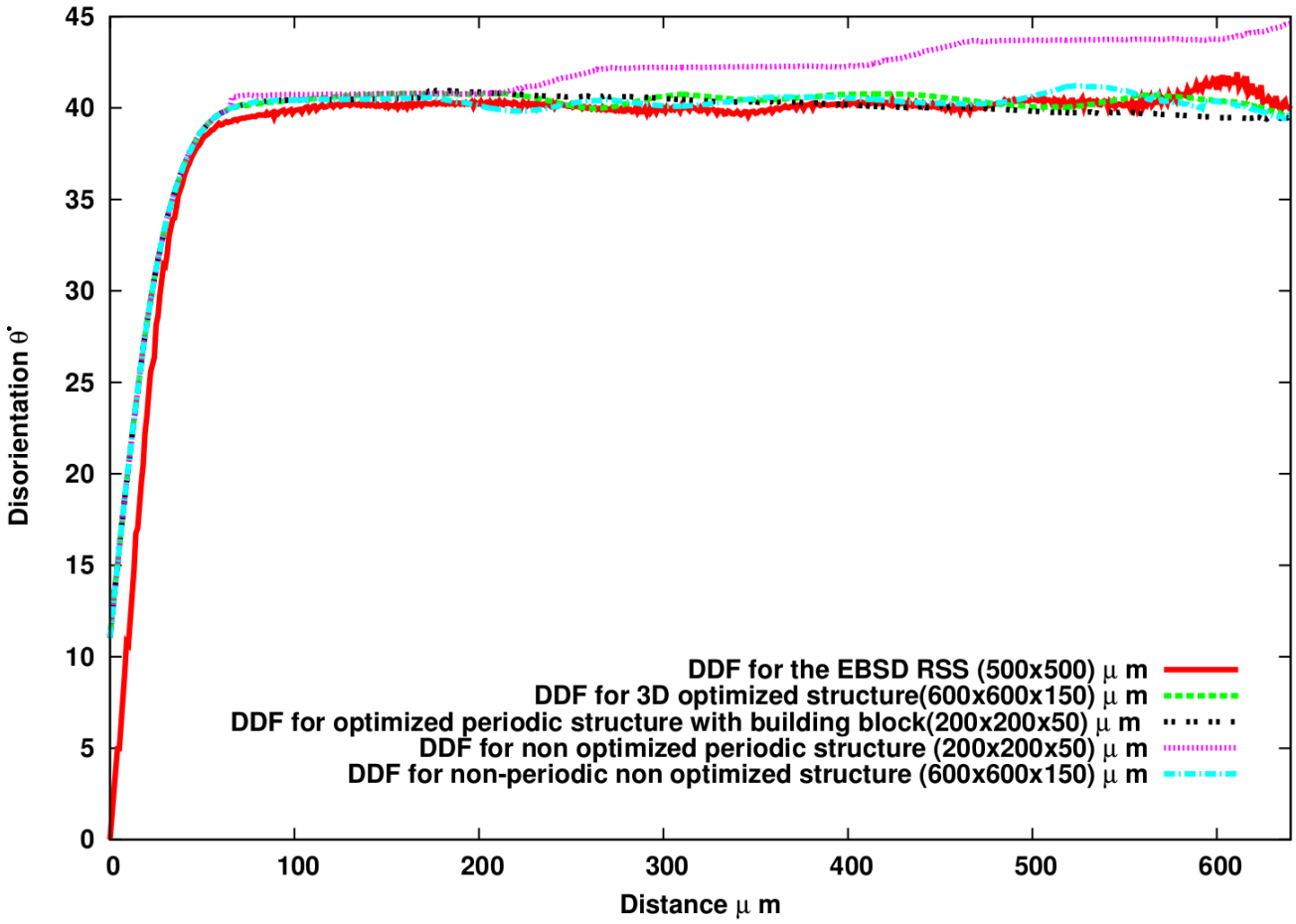

Figure 4.14: Comparative curve of the DDF functions for the RSS EBSD data and modelled 3d periodic (optimized and non optimized) microstructures with the RVE building block

while the microstructure built from the non RVE elements shows variations in the KL norm of the order of (10^{-4}). This results seems very interesting if coming back to the Torquato problem [38] of the degeneracy of the two-point correlation functions. The microstructure which consistent of this building blocks is showing an informational degeneracy in terms of the K-L norm. In other words, any sub crops with RVE sized out of this microstructure will show comparably insignificant information mismatch measured for a DDF statistics as a two-point correlation function.

4.3.5 Numerical Modelling with the RVE microstructure

In this section, the numerical model presented by [98] is employed in simulations of uniaxial tension with the RVE. They developed a user defined material subroutine (UMAT) based on elastic-viscoplastic crystal plasticity model. For brevity, details of this model will not be discussed in this section. Simulations of the uniaxial tension tests are performed on the aluminum ally(AA) alloy with optimized (RVE) and non-optimized (non-RVE) 3D microstructures. Optimized microstructure represents RVE with dimensions ($200 \times 200 \times 50\mu m$), while the non-RVE sample has bigger dimensions ($600 \times 600 \times 150\mu m$).

To further investigate the differences between the optimized and non-optimized microstructures, stress-triaxiality, a established measure commonly used to simulate fracture [99, 100] is calculated, so that:

$$\sigma_{tr} = -\frac{\sigma_{hydr}}{\sigma eq} \tag{4.16}$$

where σ_{hydr} is the hydrostatic stress and σ_{eff} is the Von Mises equivalent stress.

$$\sigma_{eff} = \sqrt{\frac{3}{2} s_{ij} s_{ij}} \tag{4.17}$$

where s_{ij} are the components of the stress deviator. The stress deviator, σ_{dev} can be written as:

$$\sigma_{dev} = \sigma_{ij} - \frac{1}{3}(tr\sigma)I \tag{4.18}$$

where the σ_{ij} is a Cauchy stress tensor and I is the identity matrix . Figures 4.16 - 4.15 represent the stress triaxiality distribution within the microstructure for the deformed material samples after 18% uniaxial tension. In these simulations the hot spots are identified as a elements which have higher stress triaxiality than average through the sample. Simulations show that the stress-triaxiality hot spots location on surface are different for the optimized and the non optimized microstructures. Furthermore, the surface hot spots distribution of the optimized microstructure which takes into account distance ordering of the texture initially observed to be closer than for non optimized generated microstructure. However there is no clear vision of the hot spots, particularly changes in the distance between localization clusters of the stress inhomogeneity. To further investigate, the stress triaxiality distribution is plotted and analyzed through the whole sample in the deformed structure (Figures 4.15 - 4.16).

Modelling show that the hot spots are much closer and packed for the case of optimized microstructure where the location of the grains are correlated to their orientation. It can be seen from the results, that optimal microstructure shows more concentration(localized) of the stress-triaxiality hot spots than the

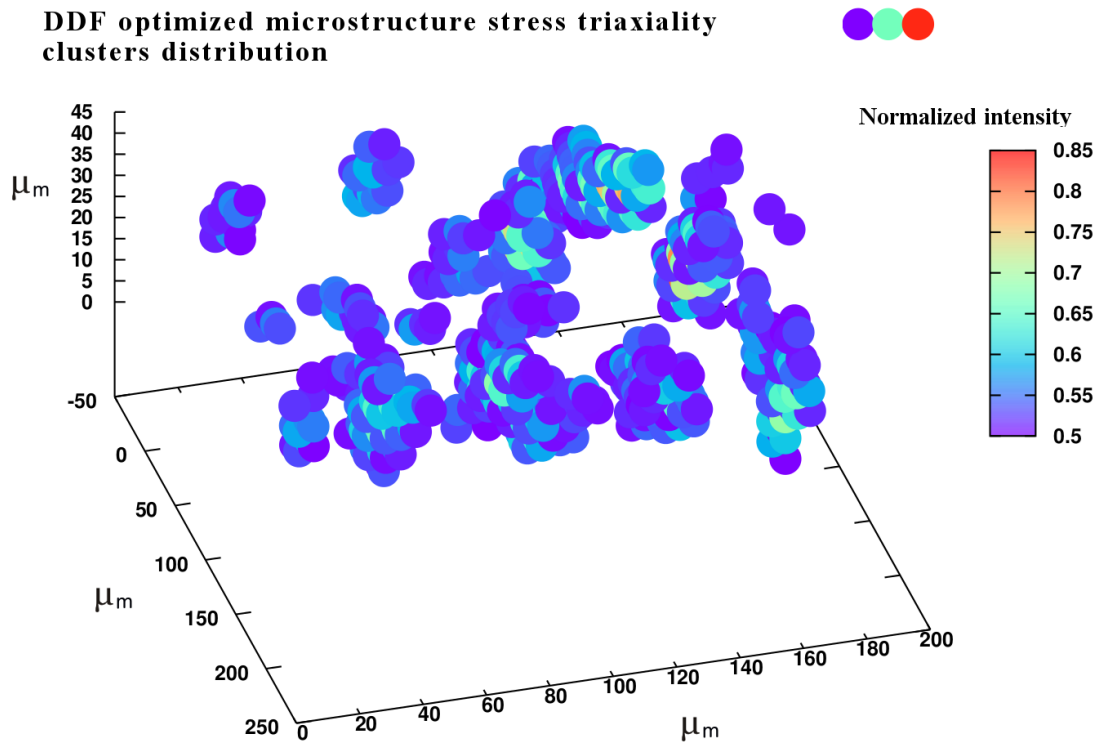

Figure 4.15: On surface stress triaxiality distribution based on the material tension FEM modelling for optimized microstructure

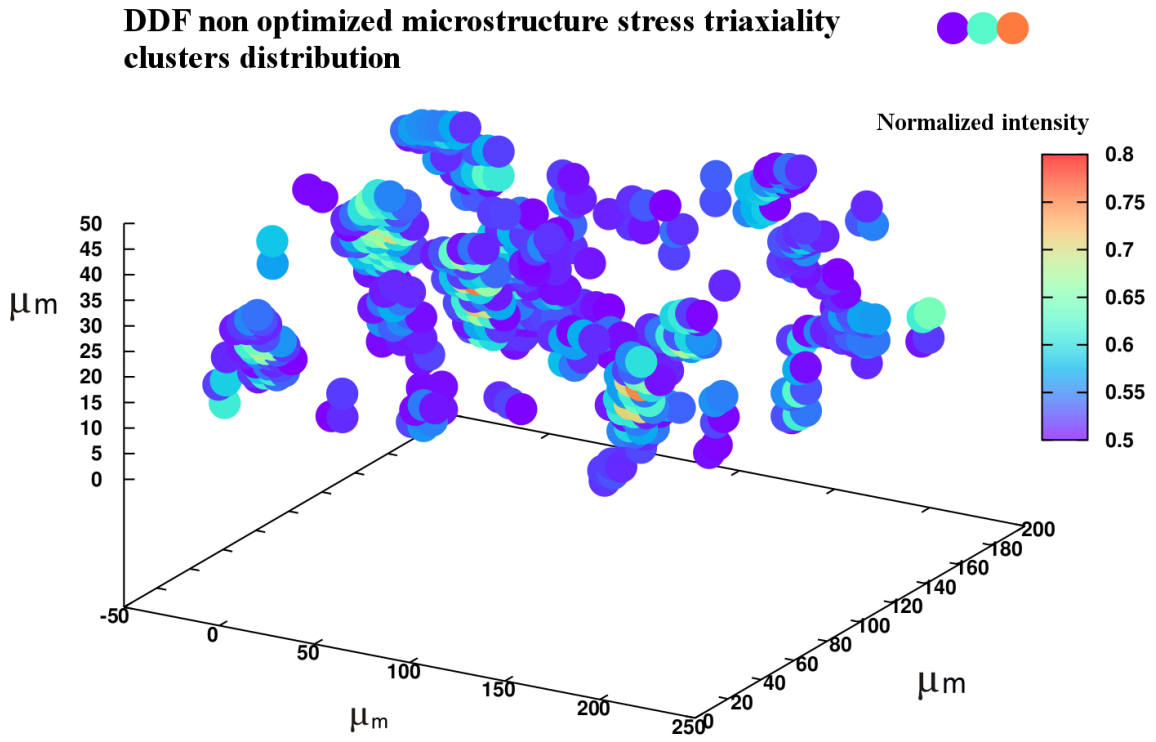

Figure 4.16: 3D map of the hot spots of stress triaxiality distribution inside the non optimized microstructure

non optimal microstructure. This is due due to the imposed texture ordering since the same boundary conditions are applied for the both models.

To quantify this behavior the distances between hot spots clusters are measured inside the material microstructure as a two point correlation function with respect of the stress-triaxiality function. In other words, the frequency of the higher stress triaxiality values, appearing in a particular fixed distance inside the material sample is estimated. The norm being introduced is similar to the DDF function but applied for the case of stress triaxiality between material points and the distance instead of disorientation θ_{ij}. Thus the maximum of the stress triaxiality value between any two points i and j can be rewritten as

$$\rho_{tr} = \frac{max_{i,j}(\sigma_{tr_{ij}})D^m_{ij}}{\sum D^m_{ij}} \tag{4.19}$$

where D_{ij} is the same distance-distribution function estimated between any two pixels within a grain pair as defined before (see 3.21). Using the same functional estimator for the D^m_{ij} function final correlation takes the form:

$$\rho_{tr} = \frac{max_{i,j}(\sigma_{tr_{ij}})V_{ij}\frac{1}{\sigma_m\sqrt{(2\pi)}}exp\left(\frac{-(x_m-\mu_m)^2}{2\sigma^2_m}\right)}{\sum V_{ij}\frac{1}{\sigma_m\sqrt{(2\pi)}}exp\left(\frac{-(x_m-\mu_m)^2}{2\sigma^2_m}\right)} \tag{4.20}$$

This functional form estimation of the D_{ij} function is critical in terms of computational complexity and makes this expensive calculation possible in general. After constructing the frequency function a measure of the frequencies of the hot spots inside the material sample can be obtained. This approach will provide some insight on the influence of the quality of the optimized microstructure on the frequency of the hot spots σ_{tr} occurring at the closest distance to each other. Accordingly, the following steps are performed to see if a correlation exists;

1. generate two different 3D microstructures with different DDF errors
2. calculate stress triaxiality frequency distribution function ρ_{tr}
3. check the hypothesis that smaller error between DDF leads to closest distribution of the frequencies of the stress-triaxiality hot spots inside the material.

The concept is the following: the more precise position of the grains should show more precise localization of the stress-triaxiality hot spots. The criteria can be rewritten as:

$$dist\rho_{tr}(max\rho_{tr}) \searrow \mid DDFerr \searrow \tag{4.21}$$

The result of modeling are presented in the Fig 4.17. The numerical analyses show that the location of the σ_{tr} hot spots are strongly dependent on the microstructures. As it can be seen from the Fig. 4.17 the minimum distance of the higher concentration of the hot spot frequencies (ρ_{tr}) is smaller(57 μm) for the microstructure with smaller DDF optimization threshold limit(DDF err=0.083 ($\times 10^{-5}$)). It can be seen that expected hypothesis is satisfied: the precision of the DDF optimization is in positive correlation with minimum distance of the hot spots location. Optimized RVE texture is actually minimizing mismatch between textural components locations inside the microstructure. This agrees well with the conclusions presented by [85] where it was demonstrated that the location and intensity of σ_{tr} hot spots is strongly influenced by grain interactions.

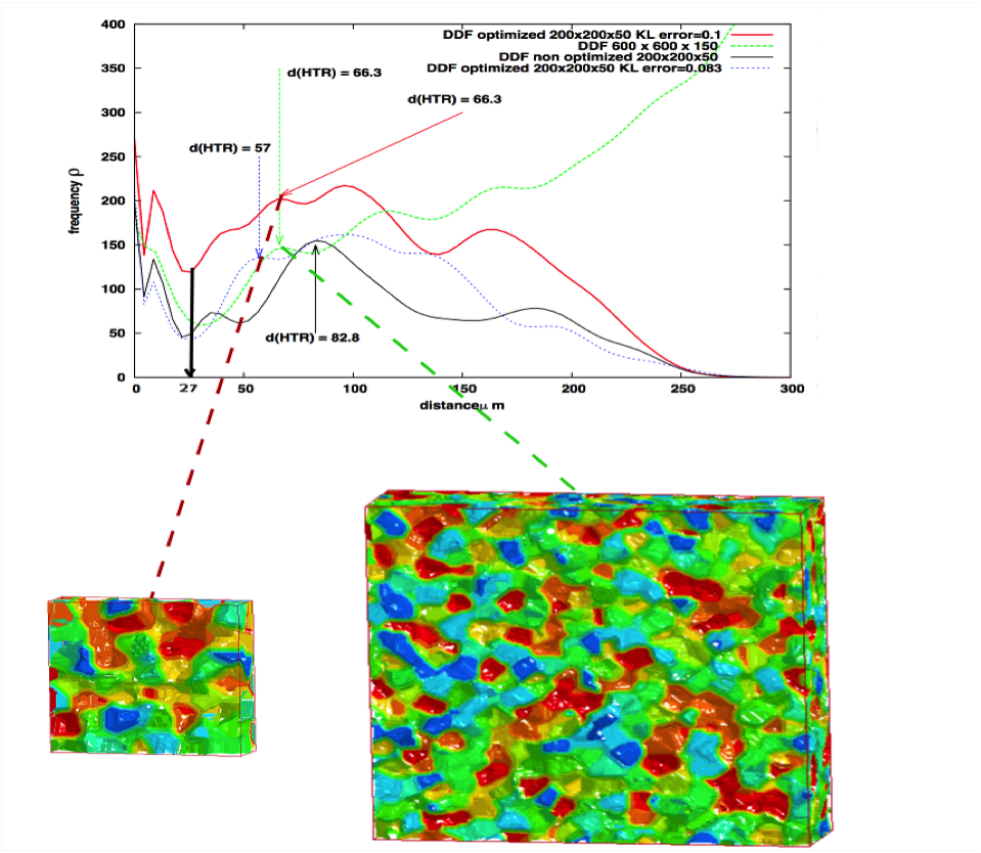

Figure 4.17: Stress triaxiality frequency distribution cross-correlation function ρ_{tr} obtained for different microstructures with different optimization errors

4.4 Conclusions

In this research a new framework for 3D cross-correlation analysis is presented. The study is based on the analytical construction of the DDF. The analytical model gives a possibility to calculate the distance-disorientation statistics in the 3D microstructure. The application of the functional form solution of the DDF applied to the 3D microstructure cross-correlation analyses and reconstruction is the first results presented in the literature for the sample dimensions much larger than a grain size.

The method of functional form statistics is extended from the 2D EBSD case to a 3D space using the same grain morphological analyses presented in the recent research of Staraselski et al. [87]. The framework developed by Rollett et al. [43] was extended using the new cross-correlation formulation as a basis optimization method to reconstruct the synthetic microstructure for the 3D data.

Finally, after constructing mathematical model and improving the computational part of the microstructure builder, the new microstructure is employed in a CPFEM analyses. Predictions show, that for nearly identical uniaxial tension stress-strain curves, the locations and intensities of a stress triaxiality hot spots are significantly different in the simulations with the different microstructure reconstructions. Thus, accurate representation of the 3D microstructure is critical in polycrystalline metals.

Chapter 5

The effect of the representative data on the modeling of dynamic recrystallization in magnesium alloys

The recrystallized texture obtained from the DRX model depends on the size of the EBSD scan. In this work, the effect of the representative scan size (RSS) on such important characteristics of DRX as nucleation sites and their distribution, grain growth and the final texture is analyzed. Different scan sizes are taken as input for the crystal plasticity finite element framework in order to compare the simulation results of the RSS and non-RSS scans used to model DRX phenomenon. Both microstructure evolution and the final texture prediction are shown for AZ31 magnesium alloy. The present research seeks an answer to the question of how precise should the quantity of the input data be while modeling DRX?

5.1 Introduction

DRX accompanying deformation can enhance formability beyond what can be accomplished due to increased slip activity and grain boundary sliding at elevated temperatures. DRX removes new defects continuously and extends the stress-strain curve to high strain values without hardening. Once the material is loaded at elevated temperatures deformation is accommodated either by slip or twinning till a critical value is reached. After this critical value (ρ_c), the material starts showing some degree of recrystallization, of a new undeformed grain in a highly deformed zone (nucleation) and (b) growth of the nucleus at the expense of deformed matrix. Unlike static recrystallization (SRX), the dislocation content during DRX evolves with time both in the matrix and the recrystallized region. Thus understanding and characterization of nucleation and growth by modeling the dislocation content by crystal plasticity methods provides a method to model DRX. DRX has been modeled in the past using cellular automata (see Raabe et al., [101]) (CA) methods that use a phenomenological model such as Kocks and Mecking law [102] to calculate the change in dislocation density, which cannot account for local evolution of deformed microstructure that determine the nucleation sites. This study presents a coupled FE model to compute local evolution of

deformation in a sample of AA5754 aluminum sheet that uses microstructural data from EBSD maps as input and accounts for the known operative deformation mechanisms. A nucleation criterion is developed and implemented into an existing in-house crystal plasticity finite element (CPFEM) model to predict the new in the microstructure reconstruction and ρ tensor determination for basal and nonbasal slip systems in HCP Mg alloys are discussed to make this approach applicable to Mg alloys that need to be processed at elevated temperatures for enhanced formability where DRX becomes important. After the effect of the threshold of the critical value on nucleation of the new grains is shown for Aluminum, the effect of the representative scan size on the modeling of the DRX in Magnesium is presented.

5.2 Nucleation of Dynamic Recrystallization

The concept of recrystallization nuclei as initiators of growth based on the dislocation density was introduced in the works of Cahn et al. [103]. The major assumption was to identify subregions with high dislocation density mismatch with surroundings within the grain across all neighboring grains. Two main concepts of nucleation and growth have been accepted in the literature: (i) pre-existing nucleation sites, which grow under deformation; (ii) nuclei are not instantaneous, but evolve during deformation. Experimental observations of Humphreys [104] show that subgrain grows sweeping away dislocations and leaving relatively clean grain. In order to satisfy to the mechanical instability, grains with lower dislocation content surrounded by neighbours with higher dislocation density are to be chosen. In order to implement this nucleation criterion, first, dislocation density was calculated from the plastic part of the strain gradient, which is obtained from the crystal plasticity part of the model. The dislocation density is calculated based on the local crystal frame for each slip system α using its descriptive vectors $\mathbf{s}_{(\alpha)}$ (slip plane normal) and $\mathbf{m}_{(\alpha)}$ (slip direction).

Geometrically necessary dislocation (GND) density is taken into account and its screw and edge parts are calculated using the shear strain γ on each slip system following the arsenlis [105] equation:

$$\rho^{\alpha}_{GN(e)} b = -\nabla\gamma^{\alpha} \cdot \mathbf{m}^{\alpha} = -\gamma^{\alpha}_{,\mathbf{k}} \mathbf{s}^{\alpha}_{\mathbf{k}} \tag{5.1}$$

$$\rho^{\alpha}_{GN(s)} b = \nabla\gamma^{\alpha} \cdot \mathbf{n}^{\alpha} = \gamma^{\alpha}_{,\mathbf{k}} \mathbf{n}^{\alpha}_{\mathbf{k}} \tag{5.2}$$

where (e) and (s) are for edge and screw parts of dislocation density respectively, and $\mathbf{n}^{\alpha} = \mathbf{s}^{\alpha} \times \mathbf{m}^{\alpha}$. Equations 5.2 are re-derived from the Nye's tensor ([106]), projecting the total deformation gradient as defined earlier on the particular slip plane and direction. This formulation gives more representative information about the contribution of particular slip plane to the dislocation density. The total GND density tensor can be consequently obtained from:

$$\rho^{\alpha} = \sqrt{(\rho^{\alpha}_{GN(s)})^2 + (\rho^{\alpha}_{GN(e)})^2} \tag{5.3}$$

The nucleation criterion is based on the difference ("jump") in the dislocation density (DDT) between the neighbouring elements i and j, and is calculated:

$$d\rho = \|\rho_i\| - \|\rho_j\| \tag{5.4}$$

The critical value of $d\rho_c$ is chosen depending on the maximum value of the dislocation density and takes into account extreme value statistics for a given data. The critical value of the $d\rho$ controls the amount

of nucleation sites as well as final texture. The smaller the value of the threshold, the more nucleation sites will be defined as potential nuclei. In the proposed model, the nucleation sites are not limited to the oriented growth or nucleation, however, new grains are not formed during recrystallization process. That means that new nucleation sites can be obtained due to deformation and new nuclei are defined in this model as deformed states of existing grains. Due to inhomogeneous distribution of dislocation density in the material (as discussed below), it is important to accurately implement it in the numerical model.

5.3 Effect of the threshold value on the recrystallized nuclei texture

Figure 5.2 shows the evaluated ρ tensor on a synthetic microstructure EBSD data from an annealed Aluminum 5754 aluminum sheet using procedure described in the previous section. Since the actual reconstructed microstructure obtained by this method is not unique, i.e. the nearest neighbor grains can be rearranged, two different microstructures that have the same statistical grain size, orientation and misorientation distributions were constructed as shown in Fig.5.1, marked MI and MII respectively.

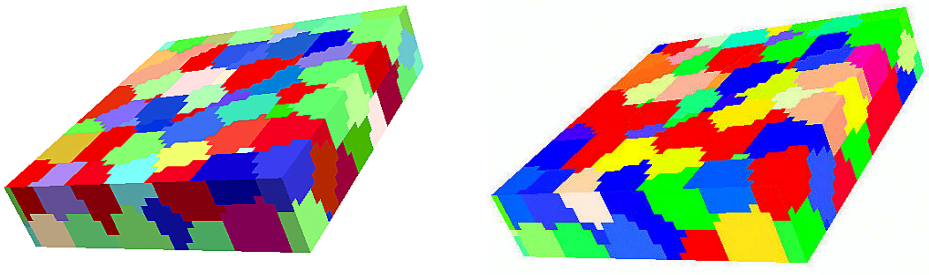

(a) Microstructure MI (b) Microstructure MII

Figure 5.1: Initial microstructure MI and MII

The Figure 5.2 represents the evaluated ρ^{α} in arbitrary units for each element in the microstructure. The value of ρ^{α} depends on the local value of the deformation, i.e. the higher values of ρ^{α} correspond to the higher dislocation content but do not imply a higher likelihood of nucleation. The local mismatch or jump in the dislocation density is calculated and is reported as an average value $d\rho^{\alpha}$ in each element. And this value is then used as an indicator of nucleation probability.

The two microstructures were subjected to uniaxial tension along the rolling direction (RD), which coincides with X-axis. The methodology of nuclei selection was applied to both microstructures and was analyzed after 20 % of total elongation along RD. The dislocation content ρ^{α} and the average jump in dislocation content $\mathrm{d}\rho^{\alpha}$ are evaluated at each integration point of the finite element.

The contour plots of the $d\rho^{\alpha}$ distribution for both MI and MII microstructures are shown in Figure 5.3 (a) and (b) respectively. Comparing these figures (Fig. 5.3 (a) and (b)), it can be seen that the two microstructures give a very different distributions of $d\rho^{\alpha}$. This is due to the differences in the local microstructure, which results in different slip system activity, and hence, in different local deformation

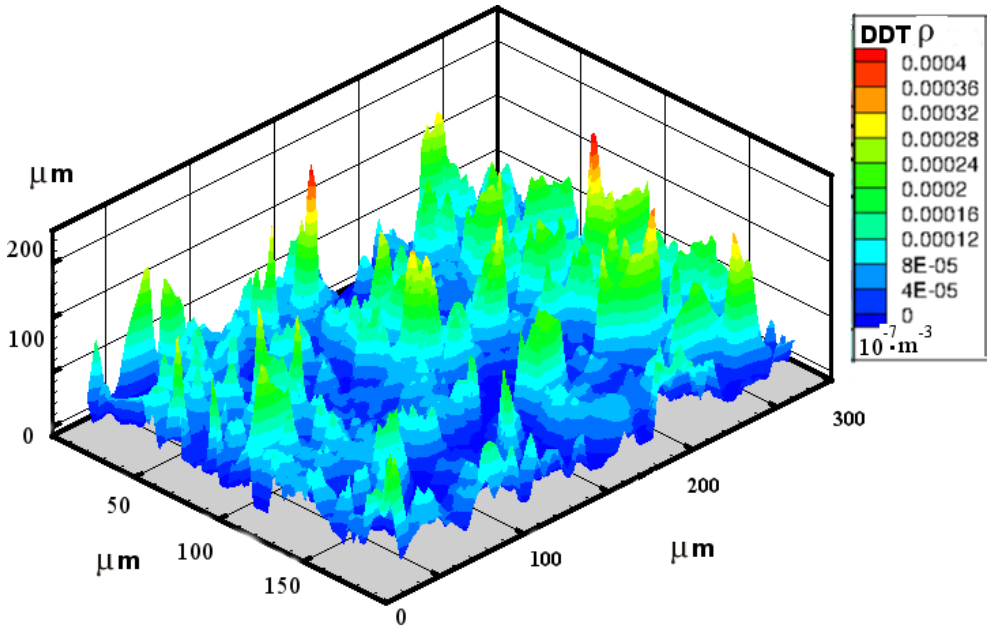

Figure 5.2: Dislocation density ρ tensor in a 3D space for the microstructure MI

distribution. A high value of $d\rho^{\alpha}$ in a particular location implies that such a region in the microstructure has higher ρ^{α} and is surrounded by regions with lower ρ^{α} or vice versa. The latter case corresponds to a possible nucleation site for a recrystallized grain as it denotes that the region of interest has lower dislocation content than its surrounding matrix and it can grow to reduce the stored work, thus, to lower the total energy of the system. By selecting an appropriate threshold value, of $d\rho^{C}$ one can have a method of identifying nucleation sites. If a region in the microstructure has $d\rho^{\alpha}$ higher than a certain predetermined threshold,$d\rho^{C}$, then, it will be identified as a nucleus.

Figure 5.4 shows the texture plots, which correspond to the orientations of the nucleated grains of the recrystallized microstructure MII, selected using different threshold values for $d\rho^{C}$ (in the range $d\rho^{C} = 5 \times 10^{-5}$ to $\rho^{C} = 4 \times 10^{-4}$ in relative units. Figure 5.4(d) has the highest threshold, which resulted in a few nucleation sites. As a result, the pole figure shows high values for poles with only a few poles. Figure 5.4 (a) has smallest threshold, and hence, has the most spread in orientations of the nuclei. Clearly, values of $d\rho^{C} = 3 \times 10^{-4}$ and 4×10^{-4} provide very few nuclei and the dρ^{α} =5×10^{-5} provides too many. The actual value of the threshold should be in between these bounds. For purposes of comparison of the recrystallization texture between the two microstructures (MI and MII) a value of dρ^{α} threshold=1.5×10^{-4} is chosen. For comparison of the prediction of the orientations of the nucleated grains produced from the two microstructures, MI and MII, dρ^{α} was calculated and a threshold value for $d\rho^{\alpha}$ =1.5×10^{-4} was used to identify nuclei.

The resultant nuclei texture is shown in Figure 5.5. Comparison with the texture for the same value of threshold for microstructure MI shows that the predicted texture for both microstructures are similar despite both of them have very different distributions of ρ^{α}.

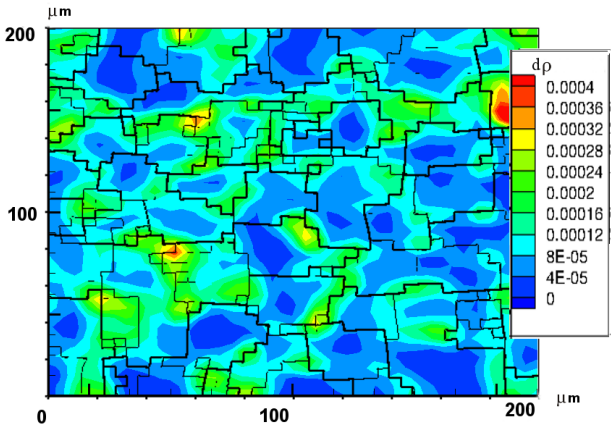

(a) $d\rho$ distribution for the microstructure MI

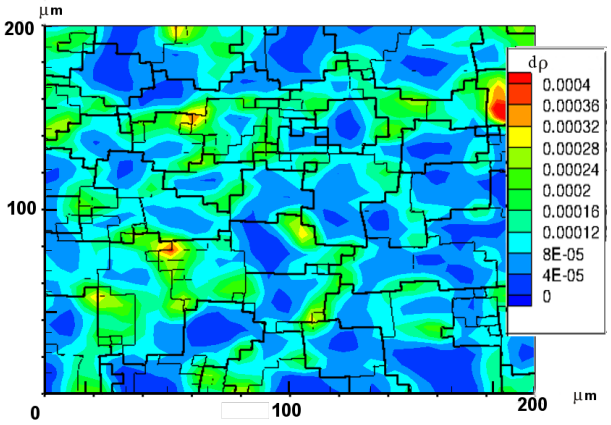

(b) $d\rho$ distribution for the microstructure MII

Figure 5.3: $d\rho$ distribution for the microstructure MI and MII

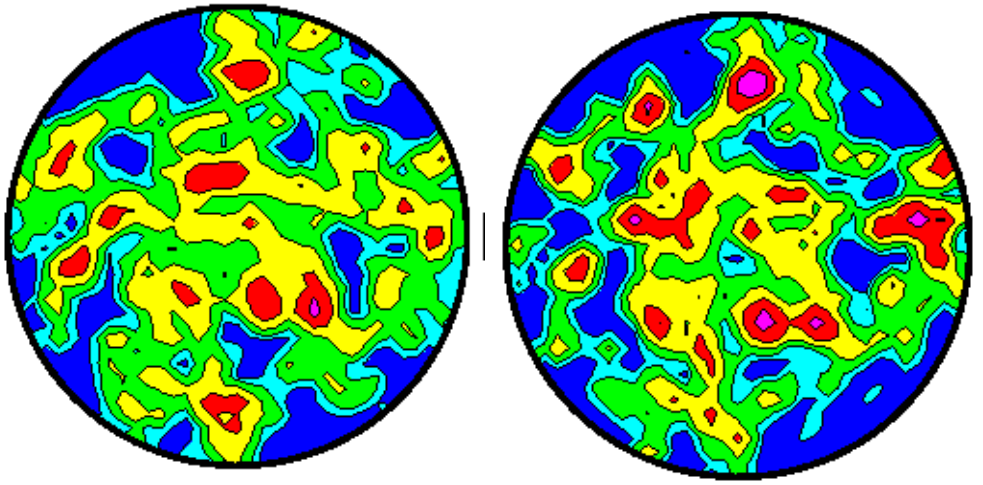

(a) $d\rho^C = 5 \times 10^{-5}$ (b) $d\rho^C = 1.5 \times 10^{-4}$

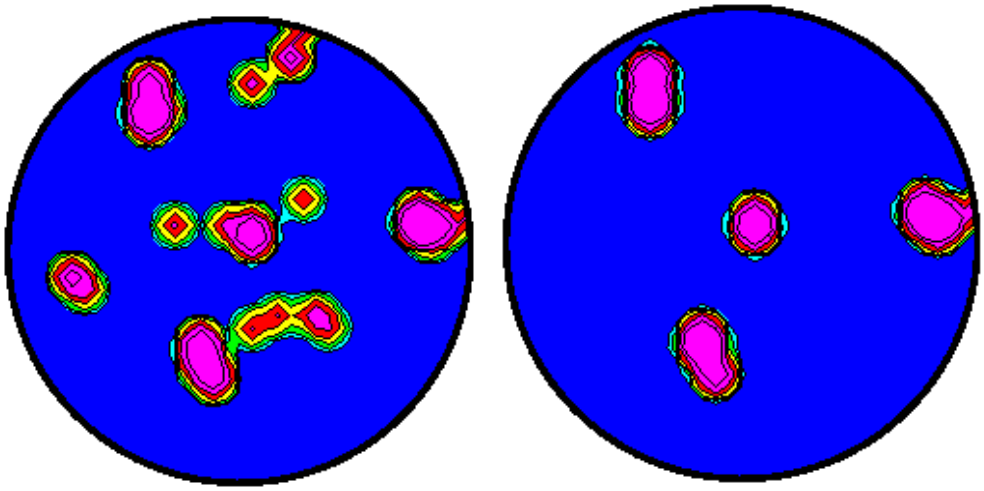

(c) $d\rho^C = 3 \times 10^{-4}$ (d) $d\rho^C = 4 \times 10^{-4}$

Figure 5.4: $d\rho$ distribution for the microstructure MII for different $d\rho^C$ values

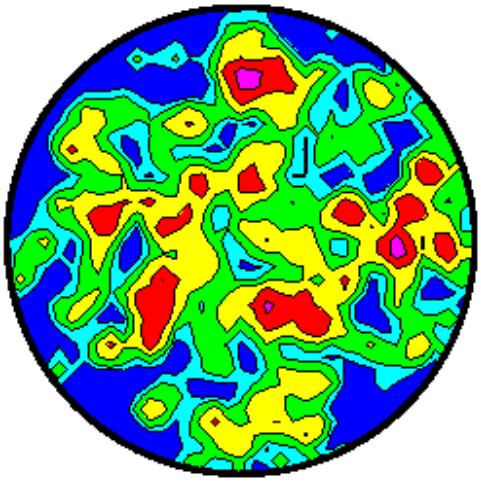

Figure 5.5: $d\rho$ distribution for the microstructure MI for $d\rho^C = 1.5 \times 10^{-4}$

5.4 Effect of the representative scan size on DRX

The initial EBSD map and pole figures from as-received AZ31 magnesium alloy sheet are given in Fig. 5.6. The pole figures show a strong basal texture typical for this alloy. The EBSD pattern is mapped into the finite element mesh with an element size equal to the EBSD step size, $4\mu m$. The grain colors represent their crystallographic orientation. The average grain size is $15\mu m$.

Different crops were taken from the initial EBSD map in order to analyze the effect of the structure size on the results of the DRX simulations in the CPFEM. The following dimensions were considered:

- $100 \times 100\mu m$ with ~ 50 grains
- $200 \times 200\mu m$ with ~ 190 grains
- $400 \times 400\mu m$ with ~ 750 grains
- $800 \times 300\mu m$ with ~ 1300 grains
- $800 \times 800\mu m$ with ~ 3000 grains

The schematic of the crops from the as-received material's EBSD map is presented in Fig.5.7. The dimension of $800 \times 300\mu m$ represents the RSS dimensions for AZ31 alloy obtained using the approach described in the previous section. The RSS for DRX and nucleation site identification are discussed in the work of Brahme et al. [107] The concept of the RSS constitutes that if the larger structure is taken the results of the CPFEM simulations will be identical. Therefore, in order to prove the RSS dimensions, the larger crop of $800 \times 800\mu m$ was taken into account and the results are presented below.

The model of DRX was implemented based on the CPFEM using cellular automata (CA) model and can be found in the [108]. The CPFEM parameters were calibrated to fit the experimental curve taken from [109]. After the parameters were obtained, the different EBSD crops were used as input and simulated

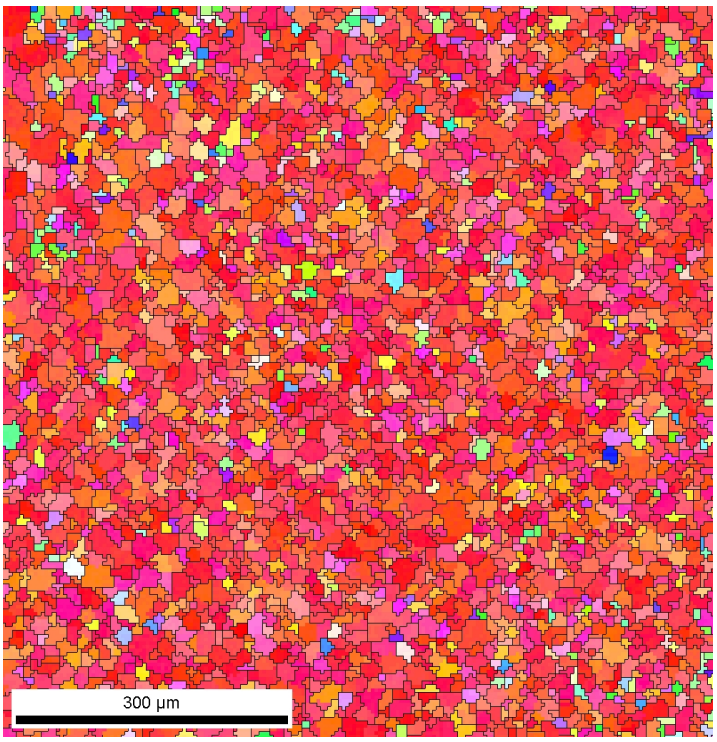

(a) Initial EBSD IPF map

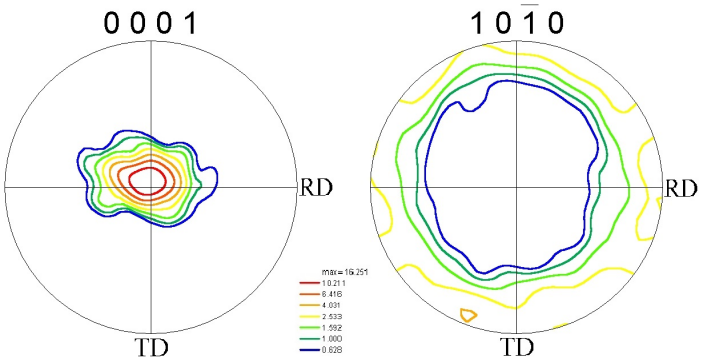

(b) {0001} and {10$\bar{1}$0} pole figures

Figure 5.6: Initial EBSD IPF map and {0001} and {10$\bar{1}$0} pole figures of AZ31 Mg alloy sheet with strong basal texture

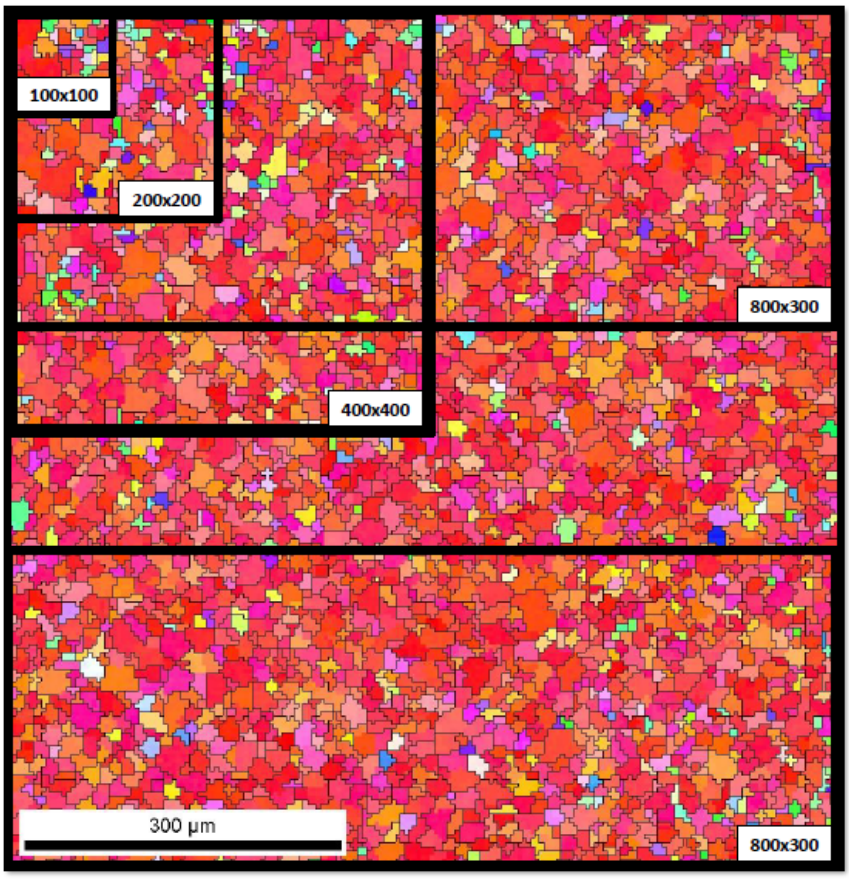

Figure 5.7: Schematic of the crops taken for the simulations

using the same parameters for all of them. A uniaxial tension test was simulated with periodic boundary conditions. The results below are presented as EBSD IPF maps and pole figures of the recystallized texture to show the effect of the scan size.

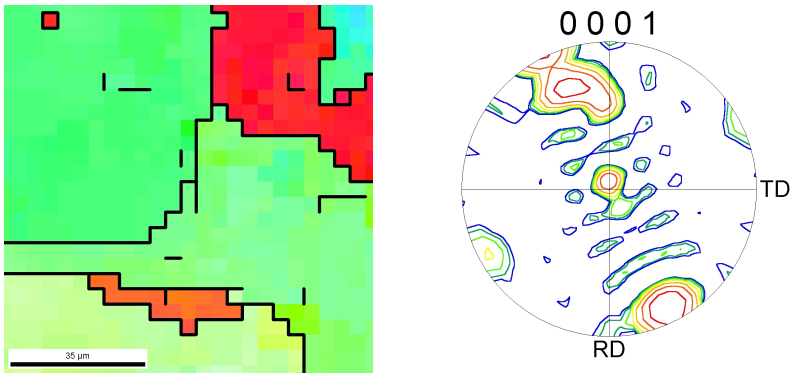

(a) EBSD IPF map (b) {0001} pole figure

Figure 5.8: EBSD IPF map and {0001} pole figure of the recrystallized AZ31 $100 \times 100 \mu m$ crop

From the Fig.5.8 it is seen that a few nuclei have grown to consume the entire structure. The orientations of the nuclei are mostly slightly rotated prismatic as plotted in Fig.5.8(b).

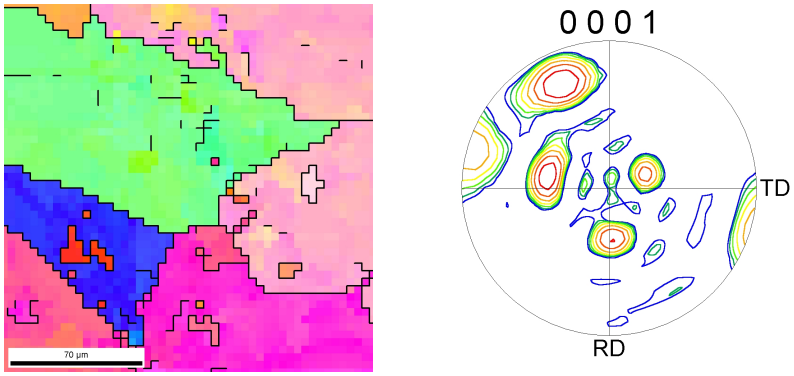

(a) EBSD IPF map (b) {0001} pole figure

Figure 5.9: EBSD IPF map and {0001} pole figure of the recrystallized AZ31 $200 \times 200 \mu m$ crop

However, the different nucleation sites from the $100 \times 100 \mu m$ crop, were identified for the larger $200 \times 200 \mu m$ structure (Fig.5.9). The EBSD map shows that the sample was nearly fully recrystallized and the texture looks more random. The results of the $400 \times 400 \mu m$ crop are presented in Fig.5.10. Random texture is observed and more nuclei are defines, which can be seen from EBSD map of the recrystallized texture (5.10(a)).

If the results should be compared to the experimental observations, it is important in crystal plasticity

model, how qualitatively the textures match both initial and recrystallized. The smaller crops, presented here have not enough amount of grains to be representative for AZ31 for DRX analysis.

The RSS scan with dimensions $800 \times 300 \mu m$ gives a pole figure close to the experimentally observed texture from [1]. The experiments showed that recrystallized texture of AZ31 doesn't change significantly, preserving close to basal {0001} texture. Another crop of RSS was taken from the full sample (bottom one in Fig.5.7) and was run with the same parameters and threshold values. The results are shown in Fig.5.12. As it can be seen, the pole figures are similar, however, the nuclei orientations are slightly different for these crops.

In Figure 5.13, the recrystallized experimental {0001} and $\{10\bar{1}0\}$ pole figures are shown. Figure shows that simulated DRX texture is in a good agreement with experimental observations.

The number of grains play a significant role while modeling DRX. In order to get reliable results, which can be compared to the experimental results, enough amount of grains should be considered. In other words, the input grains should be representative for the material.

Finally, the recrystallized texture was obtained for the larger structure with dimensions $800 \times 800 \mu m$

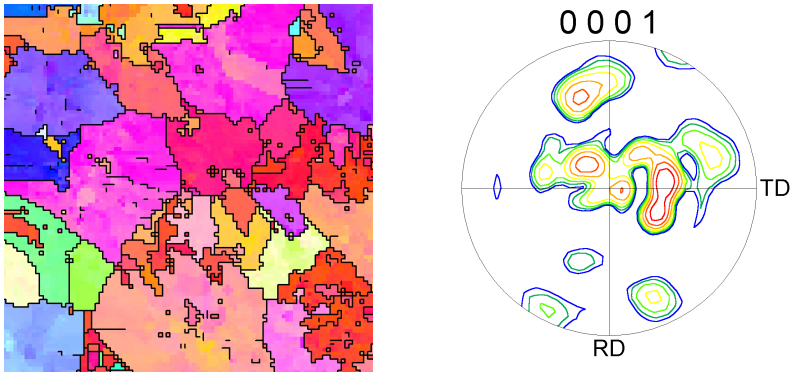

(a) EBSD IPF map (b) {0001} pole figure

Figure 5.10: EBSD IPF map and {0001} pole figure of the recrystallized AZ31 $400 \times 400 \mu m$ crop

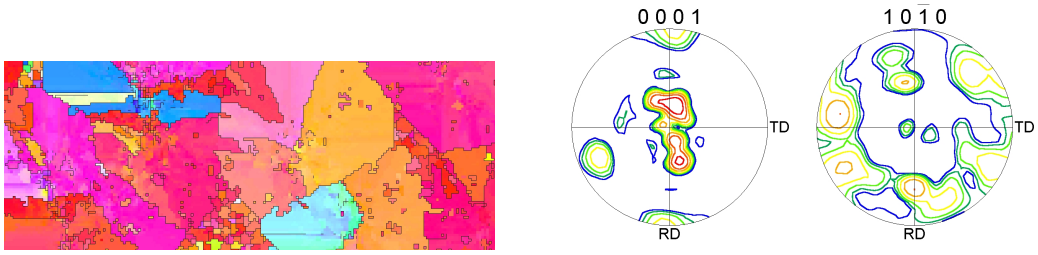

(a) EBSD IPF map (b) {0001} pole figure

Figure 5.11: EBSD IPF map and {0001} and $\{10\bar{1}0\}$ pole figures of the recrystallized AZ31 representative scan size(RSS)- $800 \times 300 \mu m$- the crop #1

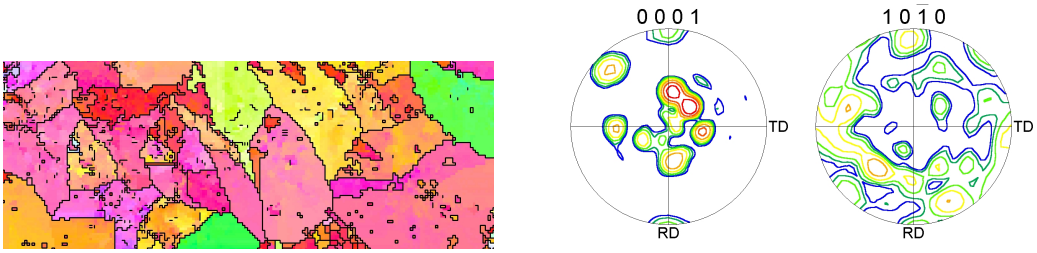

(a) EBSD IPF map (b) {0001} pole figure

Figure 5.12: EBSD IPF map and {0001} and {10$\bar{1}$0} pole figures of the recrystallized AZ31 representative scan size(RSS)- $800 \times 300 \mu m$ - the crop #2

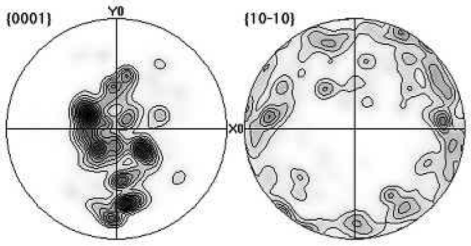

Figure 5.13: Experimental {0001} and {10$\bar{1}$0} pole figures of the recrystallized AZ31 taken from [1]

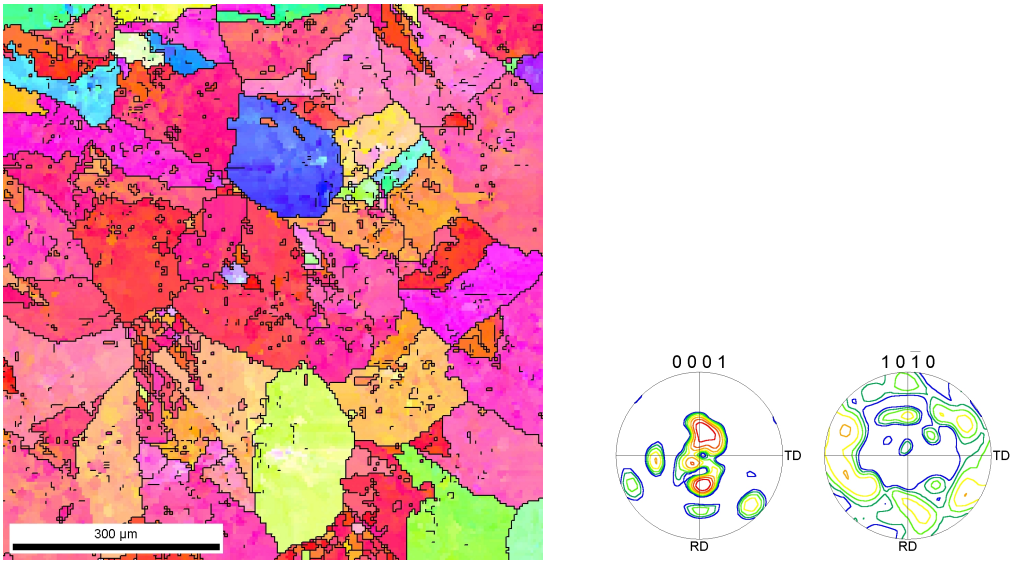

(a) EBSD IPF map (b) {0001} and {10$\bar{1}$0} pole figures

Figure 5.14: EBSD IPF map and {0001} and {10$\bar{1}$0} pole figures of the recrystallized AZ31 with dimensions $800 \times 800 \mu m$

(Fig.5.14), from where the smaller crops were cut. The same nucleation sites were observed in the full structure as in the two RSS-sized crops, which can be seen in the EBSD map. The nucleation criterion depends on the local mismatch in the dislocation content. If the simulated area is representative, the full required information will be included in it. The pole figures of $\{0001\}$ and $\{10\bar{1}0\}$ planes, presented in Fig.5.14 (b), show similar distribution compared to the RSS. Thus, it proves that if the larger than RSS dimensions are taken, they will result in the similar recrystallized texture. And therefore, there is no significant reason to take into account as large sample as possible in order to analyze the DRX behaviour, hence, the local incompatibilities.

5.5 Conclusion

Different scan sizes were taken as input for DRX model coupled with CPFEM and recrystallized textures were compared. Magnesium AZ31 alloy was used for the simulations. Representative scan size was calculated for this particular alloy based on the previous work [79]. The main conclusions of the presented work are as follows:

1. The nuclei texture will define the DRX texture. The viable nucleation sites grow during DRX consuming other grains/elements, and finally, nuclei orientations will be the ones to define recrystallized texture.

2. The DRX nuclei will grow to fill the microstructure and the average grain size increases. Since the model takes into account the first cycle of recrystallization, i.e. the grain/element can be recrystallized only one time, the growth will stop as the grains impinge.

3. The nuclei texture for different scan sizes are different. It is important to consider representative scan size while modeling DRX using crystal plasticity. The smaller dimensions can lead to the different results, which might not be representative. The results show that the effect of the considered EBSD data as input to the DRX CPFE model can be significant.

4. The DRX nucleation and growth model along with RSS provides an opportunity to predict DRX texture and microstructure.

Chapter 6

On the CPFEM analyses of the microstructure effects on the material incompatibilities initiation

This chapter presents the study of the micro-level incompatibilities. The concept of the research is based on the study of the different physical incompatibilities phenomena on the so-called meso scale (grain level). The incompatibilities are carefully defined through an extreme value statistics problem. Different aspects are discussed, such as: grain boundaries analyses, triaxiality tensor analyses, effects of the microstructures sampling on the results of the failure initiation, incompatibilities dynamics during deformation. The new metric based on the cross-correlation analyses of the stress-triaxiality tensor is presented.

6.1 Introduction

Prediction of the ductile fracture and understanding of the failure initiation mechanisms are one of the oldest material science problems, and perhaps, one of the most studied. There is a large amount of the experimental, theoretical and modeling work ([110, 111, 112, 113, 114, 115, 116, 99]) done on the study of the ductule failure. However, even the basic concepts developed in the literature such as void growth and coalescence are not well established in the community from the perspective of the initiation of the fracture [117, 116]. Moreover, there is no clear understanding of the fracture initiation neither from the perspective of the continuum mechanics, nor from the micro-mechanics (see Das et al. [116]). Understanding of the fracture mechanisms is a complicated problem due to the experimental techniques for validation are expensive and time consuming and data deficiency is an well-known issue as well. Another important problem is in the separation of the factors which leads to the failure. The material phenomenas and structure are more complicated and advanced than any measurements and techniques that can be applied. However, it is generally believed that failure initiation mechanisms are controlled and determined by the incompatibilities in the material ([118, 119, 100, 99]). Incompatibilities can be of the different nature: caused by inclusions and particles, which can effect the fracture initiation and crack propagation (shape

and directionality of the void growth etc.) (as it was reviewed in the works of Thomson et al. and Orlov et al.[120, 114]); due to the accumulated deformation (stress/strain incompatibilities) [117]; material meso-scale pre-defined inhomogeneities (distribution of the grain size, grain shape, average misorientation etc.). To explain the effect of the incompatibilities from the side of the material physics and mechanics there is a need to explain all of them in the terms of a single metrics. As it was discussed in the work of Ghadbeigi et al. [117] - strain accumulation and stress triaxiality being one of the measurements of the material localized deformation and failure cause from the perspective of the physical material incompatibilities. Therefore, there is no clear criteria of what incompatibilities are dominant for the failure process, which is commonly recognized [117]. One of the reasons is that validation of the failure is mostly based on the post-processed data, and it is hard to verify what was the exact reason of fracture initiation and propagation and as result failure. On the other hand, various failure initiation criteria on micro-level are available in the literature. Slip accumulation mismatch, incompatibility of the slip or plastic flow between grains, stress triaxiality distribution, specific grains distribution inside the material (for example Σ_3 boundaries believed to accumulate more slip incompatibilities in a simple tension) are the criteria, which can be found in literature.

The presented research work presents an analysis of the measurements and techniques mentioned above in order to answer the material science questions listed below. (i) How the incompatibilities are different for the same microstructure during the same deformation path and for different microstructures during the same deformation. (ii) How the incompatibilities are different for the different deformation paths? (iii) Are there any correlation patterns between them? (iv) What is the effect and correlation between the microstructure features and representations on the different material incompatibilities metrics. Although in order to evaluate how the incompatibilities evolve during the deformation process a new metric is presented. This work does a comparative study of how the different initial microstructures affect failure. For this purpose different microstructure were generated with and without long range texture ordering and different strain paths were investigated such as uniaxial tension and simple shear.

6.2 Experimental data

The EBSD data used in this study was acquired from AA5754 aluminum sheet samples, using a LEO 1450 scanning electron microscope (SEM) fitted with a TSL EBSD camera. The EBSD data was analyzed using the TSL^{TM}OIM software (Ver. 4.6). The data was cleaned, using grain dilation method with single iteration, neighbor CI correlation and single orientation per grain, to remove the bad data points and only data points having a confidence index (CI) above 0.2 were retained for the analyses. Grains were identified with a disorientation tolerance of 10°. Thus, the pixels having a disorientation of less that 10° were grouped together and identified as a grain. For the analyses, grains with less than 10 data points were excluded. Once grains were identified all the pixels in the grain were assigned average orientation of the grain. As a result, the disorientation of any two pixels within a grain is zero. The data was obtained from a direct chill cast and rolled aluminum sheet with grain size of 21.38μm and 23.94μm along the X and Y direction respectively. For this sample, the step size for the EBSD map was 5μm and the texture strength was 3.4. The number of grains in the scans was ∼8500 for the sample.

6.3 Concepts of the Analyses

6.3.1 Microstructure design model

In this section, the numerical model presented recently by [98] is employed in the simulations of the uniaxial tension and simple shear with the different types of the microstructure. For brevity, details of this model such as constitutive laws, parameters of the model, calibration and microstructure generation procedures will not be discussed in this work and can be found in the original work of [98]. The simulations of the uniaxial tension and simple shear tests are performed on the continuous cast aluminum alloy AA 5754 with optimized (MI) and non-optimized (MII) 3D microstructures as presented in the Table 6.1. The pole figures for the initial EBSD data and reconstructed are presented in the Figs 6.1, 6.2, 6.3. As we can see there are aceptable variations of the textural components for both microstructures MI and MII comparing to the initial data. It is important to mention that the localized textures for both of the microstructures is different. This fact will be used in the analyes of the deofmration of the microstructures MI and MII to see what is the effect of the texture localization on the localization of the incompatibilities in the same deformation mode.

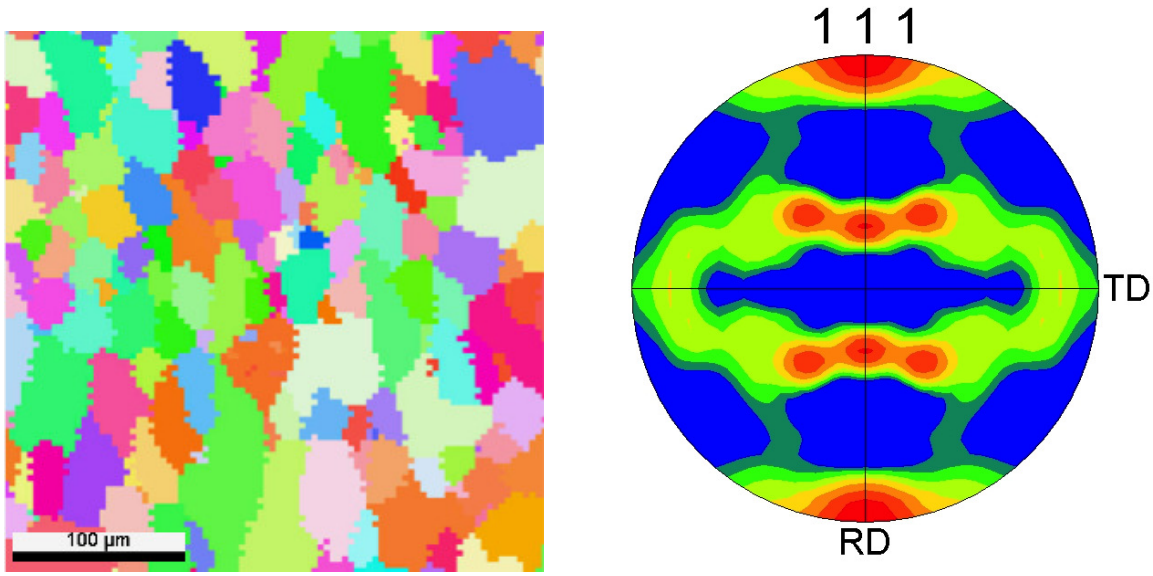

(a) initial microstructure

(b) ODF pole figure of initial ebsd data

Figure 6.1: Initial material ebsd (500x500 μ m) and pole figure .

A table below 6.1 is presenting a base microstructures used for a study with the basic microstructure descriptors.

In the purpose of particular research, the optimized microstructure is a representative volume element (RVE) with the dimensions $(200 \times 200 \times 50 \mu m)$ taking into account long range ordering of the grains. The element size was chosen to be a $5 \mu m$, which is the same as the EBSD step size. The presented dimensions

Microstructure	Dimensions(μm)	Grains	Avg. Grain Size	pixels/elements
RSS	500x500	513	25	10000
MI	200x200x50	215	25.1	160000
MII	200x200x50	215	25.1	160000

Table 6.1: Table of the base microstructures considered in the research

of the microstructures as well as RVE generation is based on the recent published works in the filed of the 3D statistical reconstruction and RVE optimization. The next statistical descriptor is taking into account is a orientation distribution function(ODF). For the statistically homogenized crystal plasticity formulation it is always important to make sure that ODF of the different 3D data sets matched, than we can expect a similar material response behavior.

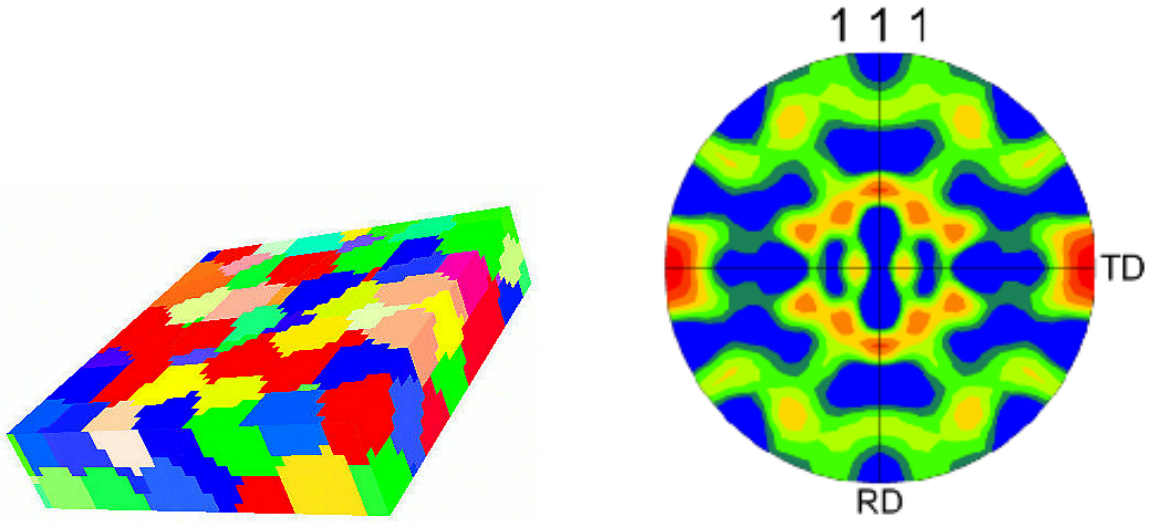

(a) microstructure MI

(b) microstructure MI pole figure

Figure 6.2: Microstructure MI with optimized long range ordering of grains and its pole figure

Each of the microstructures was loaded in the tension and shear test before the failure point for the Aluminium CC 5754 alloy which is 20% and 70% respectively (see Kang et al. [121]). The details of the simple shear modeling process are presented in the Fig. 6.4. The shear deformation γ_{shear} was obtained as a ratio $\frac{H}{W}$, where H is relative displacement of the sample. The initial dimensions of the sample L and W are kept constant. The direction of the load is shown by arrow on the top surface of the specimen. After loading the material and extracting the raw data for the analyses, it is always important to have a clear definition of the filter applied for a data to obtain a representative set of points of interest for a study. It is even more important, while working with the failure data due to the complexity of identifying weather the point is standing out of the interest bound or not. Most of the recent physical reviews and approaches treat data not in the context of such clear formulation. The definition of the data hot spots

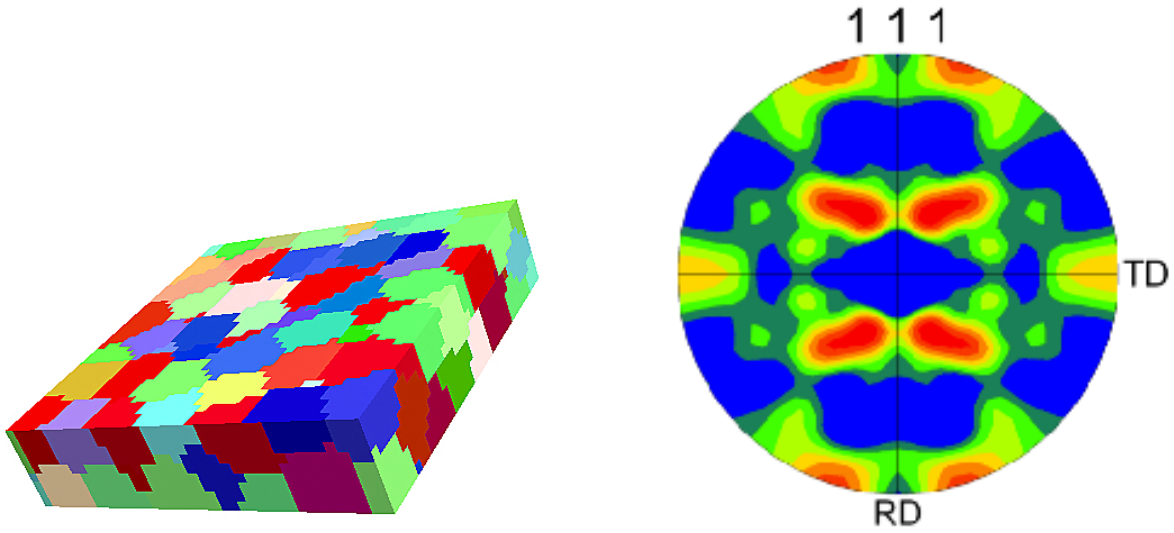

(a) optimized microstructure MII

(b) microstructure MII ODF pole figure

Figure 6.3: Microstructure MII without long range ordering of grains and its ODF pole figure

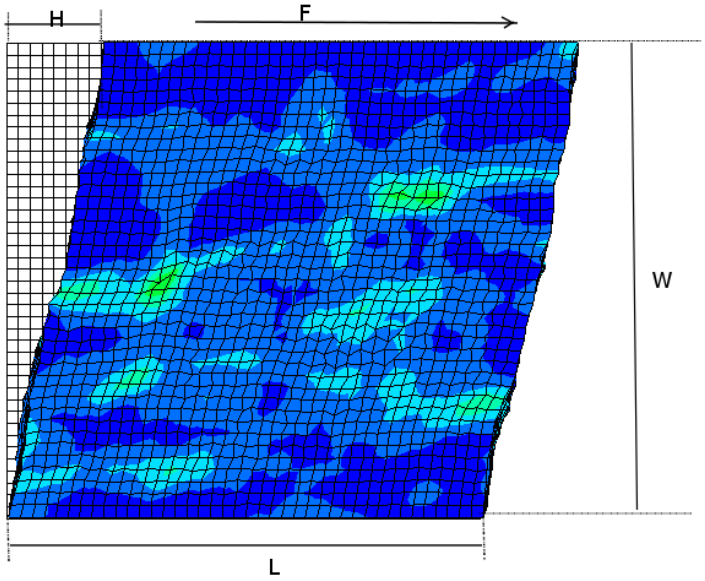

Figure 6.4: Illustrative description of the simple shear deformation mode.

are dangling in the most of the material science paper which includes data analyses. To clarify that issue of identification, the next section gives a detailed technique description of the incompatibilities definition and identification.

6.3.2 Incompatibilities definition

The metrics of the local incompatibilities (γ^{inc} and σ_{tr}) are chosen as they are widely known and published in the recent works [122, 85, 123, 124]. It is important to mention that σ_{tr} is a local measure (over element), which shows an anisotropy (or incompatibility) of the hydrostatic pressure over the applied effective stress, while γ^{inc} shows a mismatch in the neighborhood. The σ_{tr} is believed to control the growth rate of the micro void [110, 115, 114, 120]. The mismatch of the accumulated slip across the grain boundaries or transition of the plastic flow [123], which is directly proportional to the dislocation density mismatch, is chosen as an incompatibility that could lead to failure.

The characterization of the stress triaxiality (σ_{tr}) and the total slip (γ_{tr}) incompatibilities was performed for both MI and MII microstructures. The different microstructures were chosen to show the effect of the local texture sampling on the localization analysis. The stress triaxiality was calculated for each finite element as:

$$\sigma_{tr} = -\frac{\sigma_{hydr}}{\sigma_{eq}} \tag{6.1}$$

where σ_{hydr} is the hydrostatic stress, σ_{eq} is the Von Mises equivalent stress. The mismatch of the accumulated slip was calculated for each element,i, and its neighbors as an absolute value of the difference:

$$\gamma_i^{inc} = \sum_{j=1}^{9} \sum_{\alpha=1}^{12} \int_0^t \left| (\dot{\gamma_i^{\alpha}} - \dot{\gamma_j^{\alpha}}) \right| dt \tag{6.2}$$

where j goes over all neighboring elements (1..9 for the case), and α goes over all (12) slip systems. The effect of the slip incompatibility on the failure and its importance on the grain boundary cracking could be found for example in the works of Gertsman et al., Jaward et al., Shi et al., [125, 118, 124]. After the tests were performed and the data metrics were extracted from the deformed microstructure, the results were analyzed from the perspective of the new density metric analyses for σ_{tr} and specific boundaries analysis for the γ^{inc} metrics. The microstructure analysis was based on the principal measurements of the mismatch in the Euler space, so-called a disorientation analysis. The idea is to calculate the disorientation (θ_{ij}) between each neighbor grain pair (i and j) with high mismatch in accumulated slip ro see how they correlate with each other.

6.3.3 Hot spots identification procedure

After microstructures are generated, the uniaxial tension and simple shear tests were performed in order to analyze the extreme value statistics values (hot spots) for the incompatibilities. The hot spots were identified for each of the incompatibility (σ_{tr}, γ^{inc}) consistently using the method presented in the Figs. 6.5, 6.6. First, the data is collected for the entire sample 6.5b, then, the median ($\sigma_{tr} = 0.32$ for example for tension case) is obtained as shown in Fig. 6.5b. The data points, which exceed the median are extracted, and the filtered data is obtained as a standard 5% extreme value statistics.

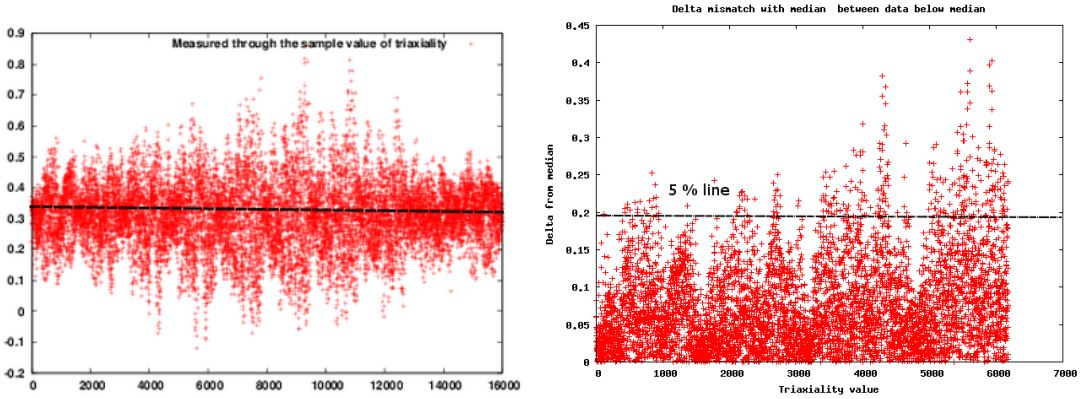

(a) Initial distribution of the σ_{tr} for the each element of the microstructure

(b) Δ of the below the median data with 5% line - filtered hot spots data line

Figure 6.5: Filtering process for the hot spots identification based on median

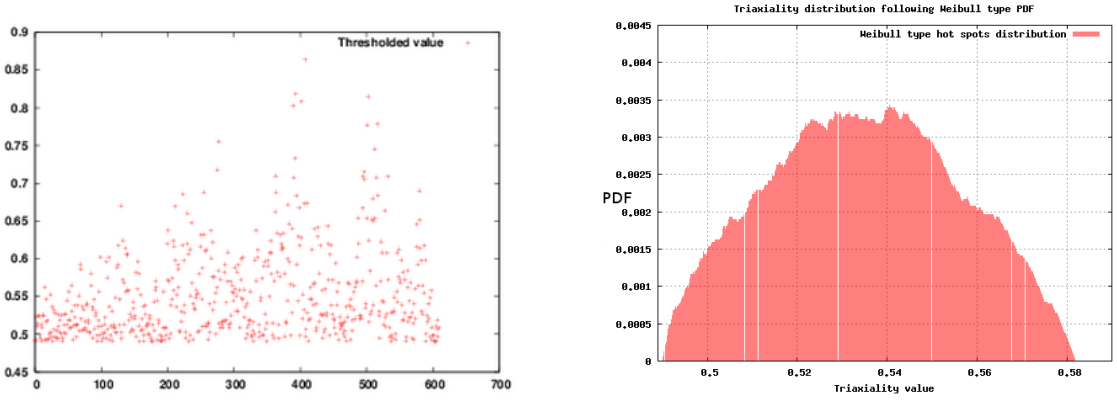

(a) Filtered distribution of σ_{tr} data

(b) Extreme value statistics data PDF of σ_{tr}

Figure 6.6: Process of obtaining the data for the hot spot of the incompatibility.

An example of the filtering data process is presented in Fig. 6.6a. The final distribution of the hot spots is expected to follow the extreme point statistic of the Weibull distribution as shown in Fig. 6.6b. The presented distribution is obtained after the modeling 20 % tension for the microstructure MI. For the consistency, the same technique is applied for both incompatibilities types (i.e. σ_{tr} and γ_{inc}). The described procedure is a classical example of the extreme value theory ([126, 119]) and is called point over threshold (POT) approach in statistics. By following this simple steps,

6.3.4 Correlation function analysis of the incompatibilities

While material deforms, the major changes can happen with the incompatibility clusters *(IC)*: (i) the clusters will change their shapes, (ii) the location of the *IC* will change (clusters start merging).(iii) the clusters might disappear and re-distribute. In order to quantify this behavior, the distances between the clusters are measured inside the material microstructure using a form of two point correlation function with respect to the incompatibility function and distance-distribution function. In other words, the frequency of the incompatibility hot spots' values that appear in a particular fixed distance inside the material sample is estimated. The introduced norm is similar to the distance-disorientation correlation function (DDF) but applied to the case of the *IC* between any material points instead of the disorientation θ_{ij}. Thus, the norm of the value of the *IC* between any two points i and j can be rewritten as:

$$\rho_{tr} = \frac{max_{i,j}(f_{ij})D_{ij}^{m}}{\sum D_{ij}^{m}} \tag{6.3}$$

where D_{ij} is the distance distribution estimated between any two points of interest (elements or pixels), and f_{ij} is the observed function of interest(σ_{tr} ,γ_{inc}). The analysis of the frequency distribution of the *IC* is a new concept for the *IC* study, it includes the evolution of the *IC* during the dynamic deformation processand not at the final stage only. The general shape of the frequency curve is presented in the Fig.6.7. As it can be seen, the frequency of the *IC* hot spots distribution over the distance has almost identical shape for different loads in the scope of the same deformation mode, however, the intensity of the hot spots changes. This can be explained by the fact that more load activates more localization of the particular microstructure metrics such as σ_{tr} for a case. The curve can be divided by 3 local minima(or maxima), each of them has its own meaning in the clustering process. First local minima (highlighted by "2") identifies the cluster size, the cluster size is expected to be constant for all the cases and is about (as the distance of the neighboring elements with step size $5\mu m$ $15\sqrt{2} \sim 23.6$). The next minima point ("3") shows the minimal inter-cluster distance, this minima does not change over the amount of deformation, however, changes in its intensity, which means that amount of the clusters on the minimum distance is increased.

The full information about the deformation metric can be obtained from this curve. For example, the Fig. 6.7 shows that the simple shear test has fewer clusters of σ_{tr}, also the size of the simple shear clusters is the same as those for the tension case. The intensity of the inter-cluster distance is much lower, which means that the global spread of the σ_{tr} value is times less than for the tension case. More general conclusion can be made: the shear process requires less texture evolution in general deformation. Analyzing ρ_{tr} curve behavior, it can be understood how the clusters change with respect to each other, and how the inter cluster distance changes as well.

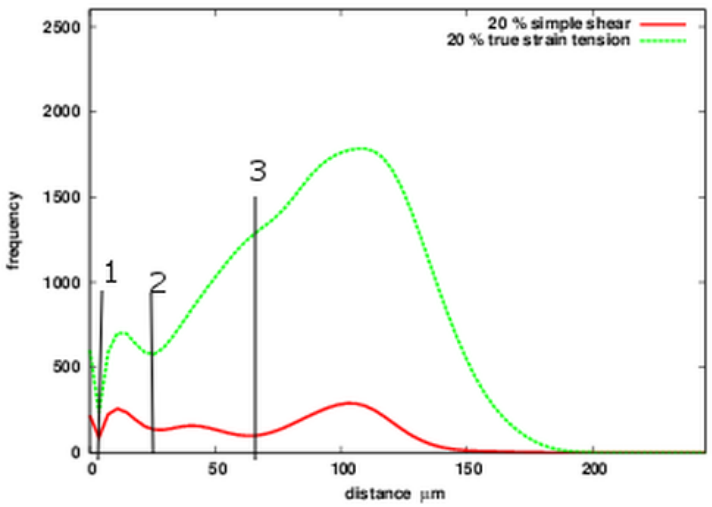

Figure 6.7: ρ_{tr} density function for different strain levels tension case

6.4 Results and discussion

6.4.1 Preliminary results

The results of the tension and simple shear tests are presented in the figures 6.8 and 6.9. As it can be seen, different microstructures for both strain paths give significantly different deformed structures. Comparing simple shear test results at 70% of shear strain (cases a and b) one can see that microstructure MI shows the strain localization along the middle line from the right side (parallel to the shearing direction). The reason is that the top part of the structure accommodated more strain, while the bottom part stays almost undeformed. However, the microstructure MII has almost uniform shear deformation. The deformed surfaces show that the localizations of σ_{tr} and γ_{inc} are different in MI and MII microstructures. It can be seen also from the Fig. 6.9 that the uniaxial tension shows more hot spots of stress triaxiality than simple shear test.

Analyzing the same regions in tension and shear, one can see that picture has changed. At 20% of the tensile strain, the deformed microstructures exhibit high localization of the σ_{tr} values and low localization of the γ^{inc}.

Next, it needs to be found out how the incompatibility of the slip transition match with localization of the σ_{tr} for the both cases. Assuming that we have a void initiated at a zone with high level of the accumulated slip across grains, if we consider the void coalescence failure model, the growth rate of the void will be controlled by the triaxiality value at the particular point. Zones, where σ_{tr} intersect with the zones of the high value of γ^{inc} might lead to the higher probability of crack initiation and its growth [124, 118].

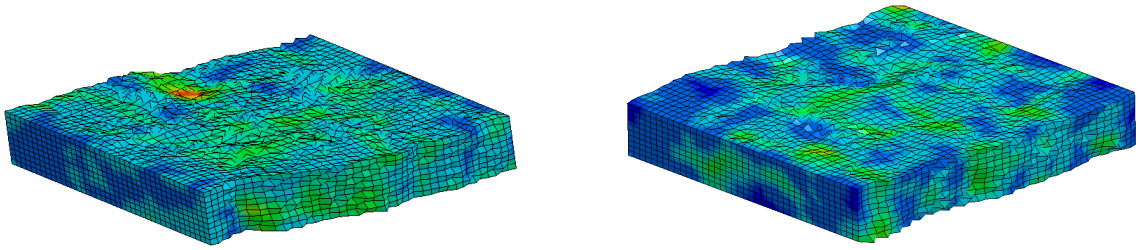

(a) 70 % shear γ_{acc} localization microstructure MII

(b) 70% shear γ_{acc} localization microstructure MI

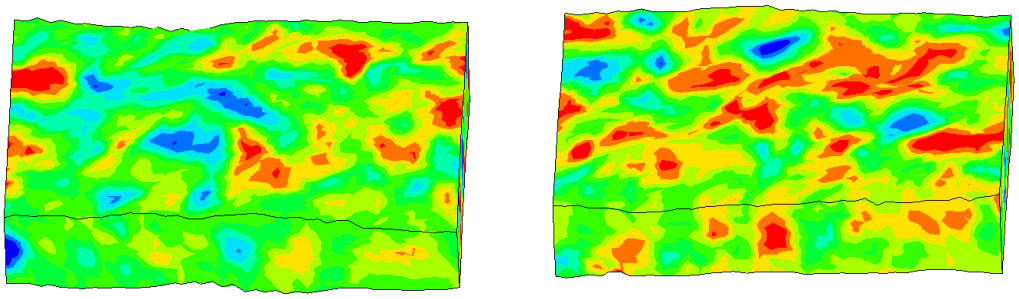

(c) 70% shear σ_{tr} localization microstructure MII

(d) 70% shear σ_{tr} localization microstructure MI

Figure 6.8: Simple shear result for both microstructures (MI and MII -200x200x50 μ m) in case of the simple shear. γ^{inc} distribution on the top and σ_{tr} on the bottom

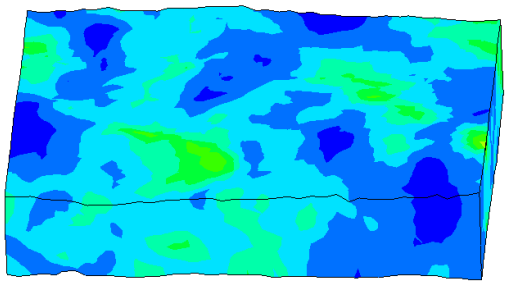

(a) 20 % tension γ_{acc} localization microstructure MI

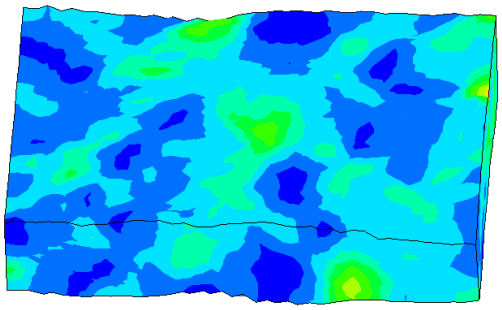

(b) 20 % tension γ_{acc} localization microstructure MII

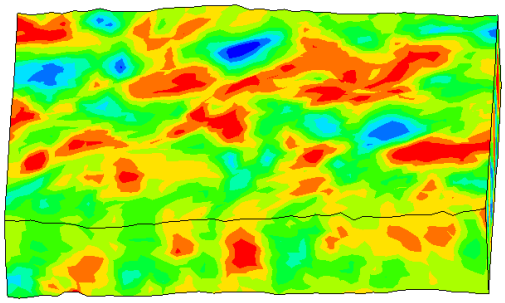

(c) 20 % tension microstructure σ_{tr} localization MI

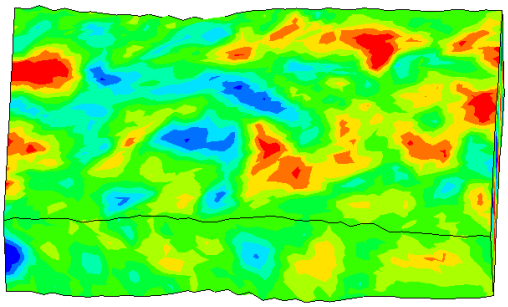

(d) 20 % tension microstructure σ_{tr} localization MII

Figure 6.9: Comparing of the micro structures ($200x200x50\mu m$) for uniaxial tension test.

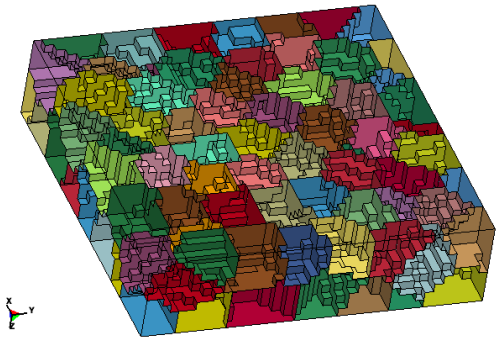

(a) Initial microstructure MI

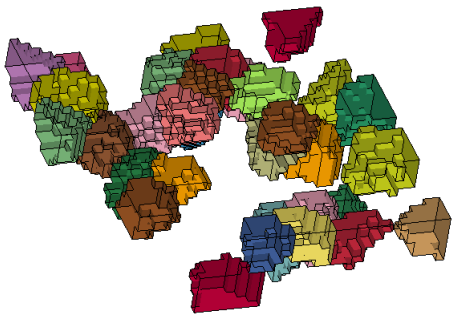

(b) 20 % tension σ_{tr} localization microstructure MI

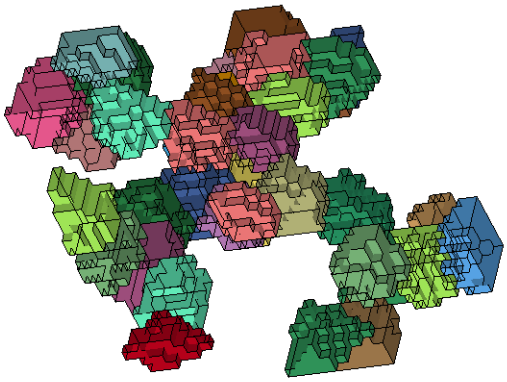

(c) 20 % tension microstructure γ_{acc} localization MI

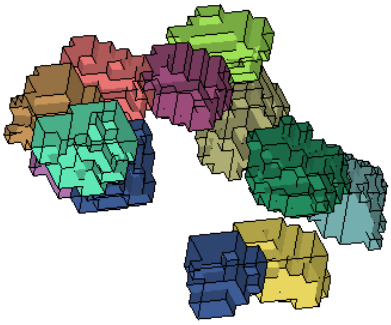

(d) 20 % tension $\Sigma 3$ boundaries MI

Figure 6.10: Comparing of the tensile microstructure MI grains with the hot spots of σ_{tr} and γ^{inc} as well as Σ_3 GB for uniaxial tension test.

6.4.2 Incompatibilities analyses

It can be seen from the plot that the localization zones for each criteria are different. Moreover, the preliminary analysis does not show any correlations between them (Figs.6.11 6.12) In order to understand if a correlation exists, the analysis of the full 3D microstructure with identification of the σ_{tr} and γ^{inc} was performed. First, the results of the simple shear and uniaxial tension cases are compared for one microstructure (namely MI) to see if there is any correlation within the clusters for the different strain paths. The results of the 3D projection of the hot spots of triaxiality to a 2D (collapsed by z) are presented in the Figures 6.11 6.12.

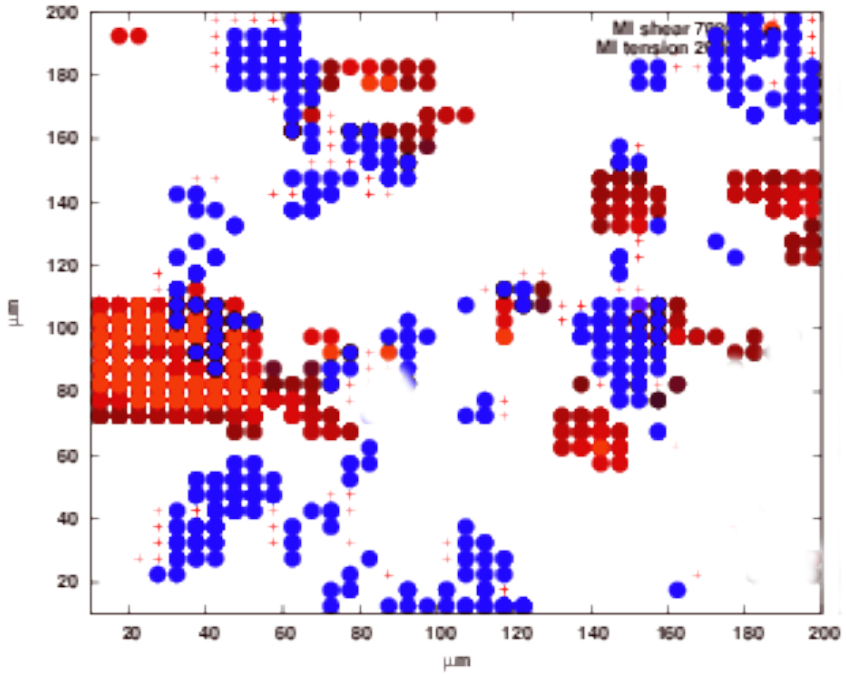

Figure 6.11: Element of grains identified by high value of the γ^{inc} for both shear and tension

As one can see, the elements of the grains identified by high value of the mismatch are different for different strain paths. There is very little correlation between grains that exhibit high mismatch of γ_{inc} or σ_{tr} in the same microstructure for the different loads. The analysis of the grain incompatibility shows a high disorientation angle between those the grains that have higher incompatibility, θ_{ij}, for both cases (tension and shear). Hence, the slip transition across these boundaries is expectedly high.

The next question is how the incompatibilities intersect during the same deformation path 6.16 **??**.

There are a few grains that have common incompatibilities for both tension and shear. This result is supported by the previous works of Das et al.,[116]. The results show that microstructure features that lead to the localization of the strain (γ^{inc}) are different from those for stress. This might be explained from the perspective of the failure initiation and propagation mechanisms. As it was shown earlier, the slip incompatibility is correlated with the high disorientation grains.

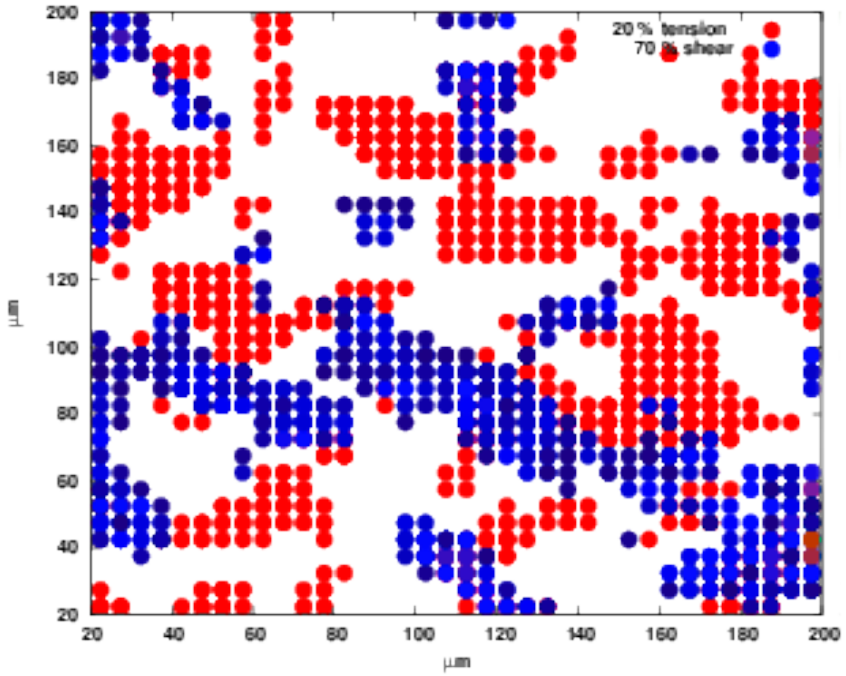

Figure 6.12: Element of grains identified by high value of the σ_{tr} mismatch for both shear and tension

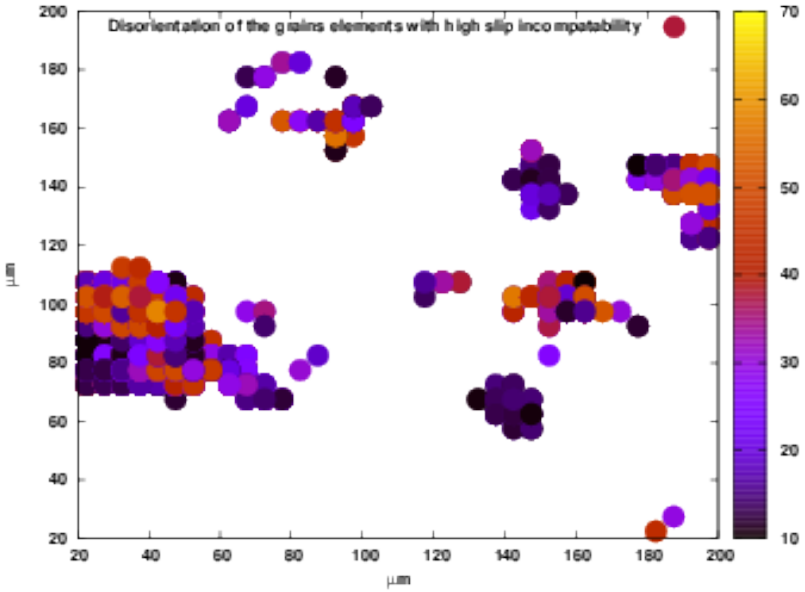

Figure 6.13: Disorientation of grains elements identified by high location of the accumulated slip mismatch γ^{inc}. 70 % simple shear case

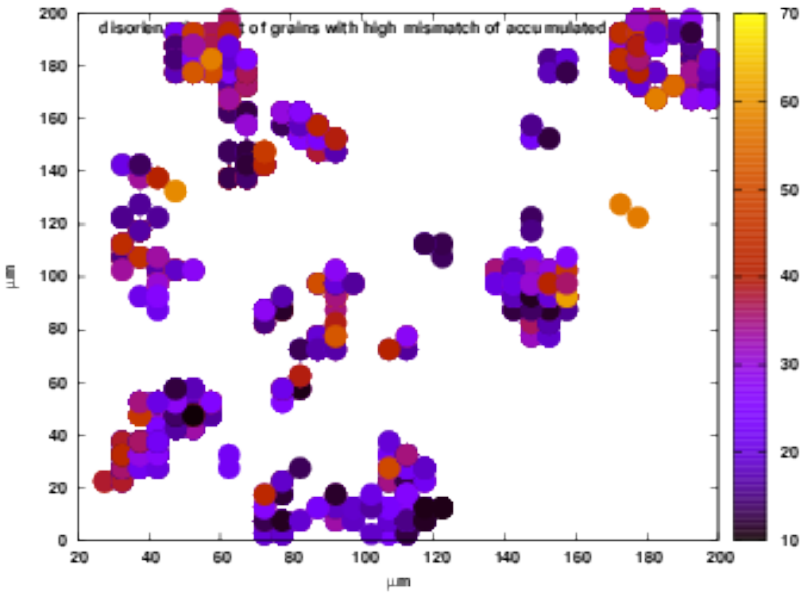

Figure 6.14: Disorientation of grains elements identified by high location of the accumulated slip mismatch γ^{inc}. 20 % tension case

As the next step of microstructure research, the boundaries are characterized according to their energy or specific cite such as lattices structure, which corresponds to the localization of the incompatibilities. For that purpose, the CSL analysis was performed.

It is already known that fracture might be initiated most likely at the grain scale at the coincidence site lattices (CSL), which are close to Σ_5 or Σ_3 as the low energy configuration boundaries. This CSL boundaries rarely exist in the real material due to their complexity. However, they are of the high interest and focus of the fracture research because of their energy configuration. The results presented in Fig. 6.18 show that after the tension test, the amount of Σ_3 and Σ_5 boundaries within the γ^{inc} hot spots, significantly increased. The density increased to about ~ 3 times, which is in a good agreement with the results obtained in the works of Stein et al. [122].

6.4.3 Dynamics of the σ_{tr} localization behavior. Correlation analysis and microstructure effects

After the preliminary analyses of the deformation hot spots, there is a question of what happens in a material during the deformation before the failure point. The experimental techniques cannot still answer the question due to the complexity of this kind of analysis.

This analysis is more complex because the metric should be introduced for the dynamic change of the incompatibility. First, the analysis of the hot spots on the different strain levels was done. The results presented in Figs. 6.20, 6.26 show that σ_{tr} hot spots do not evolve significantly during deformation process.

The localization of the triaxiality occurs at the level of 2% strain and it slightly evolves at the higher strains ($2 - 10\%$ true strain) up to the failure (20%). This observation is also explained due to the insignificant changes of for the 20% strain. This fact was checked for the simple shear test as well (Fig. 6.26). The pattern is more complicated as the basic clusters do not change during the deformation and are defined in the preliminary steps.

To quantify this behavior without visual analysis, the distance density cross-correlation tensor, ρ, is presented. Dynamics of the incompatibility metrics can be explained based on the figures 6.23, 6.21. From the Fig. 6.21, which represents the uniaxial tension case, it is clear that the clusters and their locations are formed at the initial strains. The mismatch between the cluster densities and distance levels is insignificant. It is clearly seen that after 2% strain level, all the triaxiality hot spot localizations are nearly identical (the same behavior can be observed in Fig. 6.20).

6.4.4 Local texture effect on the deformed microstructure

The idea of the method, which will be presented below, is to identify the effect of the different microstructural components on the deformation. As it was already shown, the different microstructures with different

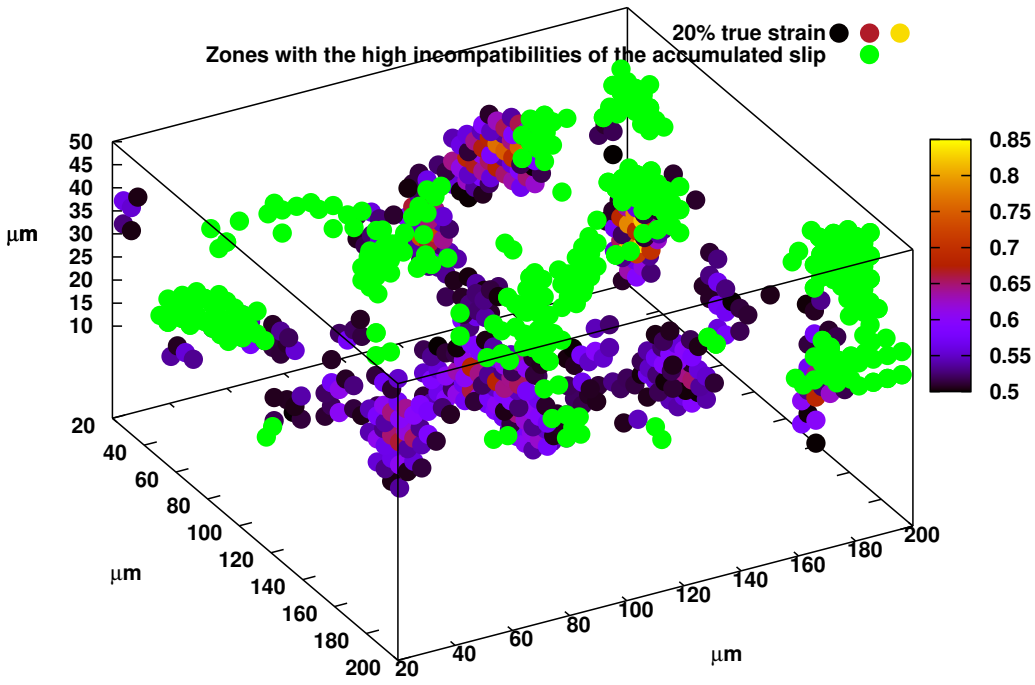

Figure 6.15: stress σ_{tr} triaxiality distribution and accumulated gamma mismatch γ^{inc} MI tension 20% final step

RVE's give different deformation localization patterns. Therefore, it is important to determine what has more effect on the deformation localization - boundary conditions or localization of the specific microstructural features? How much the matrix affects the localization of the strain and γ^{inc}?

To answer this question, the following analysis was performed as presented in Fig.6.24, 6.24. First, the data for slip localization γ^{inc} was extracted and the grains were identified as it was discussed in the previous procedures. The grains that have an effect on the localized strain partitioning are extracted from the microstructure in the microstructure block of the smaller size (see Fig. 6.25). Then, the same shear test simulation with the same boundary conditions was run for the cropped microstructural cube. This procedure was carried out for both microstructures MI and MII. The results are shown for the microstructure MI, however, the same pattern was obtained for both microstructures. If the matrix had a significant effect on the deformation, similar deformation patterns would not be expected (distribution of ϵ_{eff}). And if the localized deformation is predominately caused by the specific grains (textural effect) one should expect to see close γ_{inc} pattern, as well as deformed grains structures and deformation distribution(ϵ_{eff}).

The results of the proposed procedure are presented in Fig. 6.26. The top set presents the zoomed

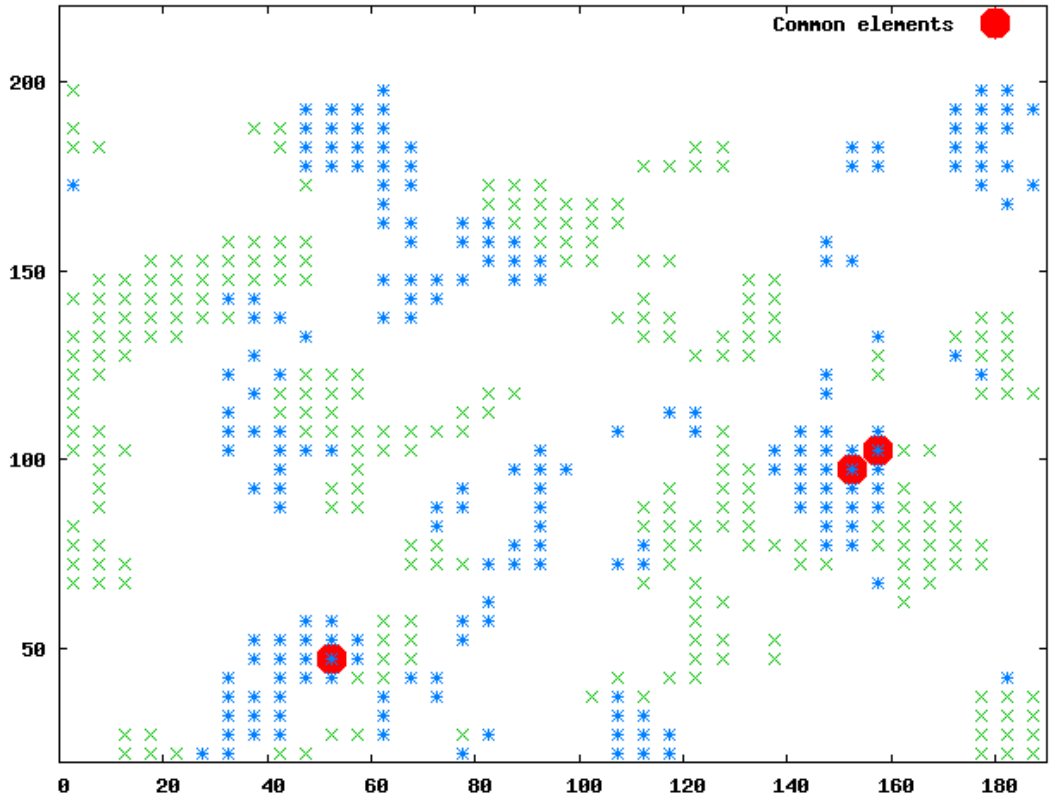

Figure 6.16: The interception of all hotspots inside the microstructure MI tension case

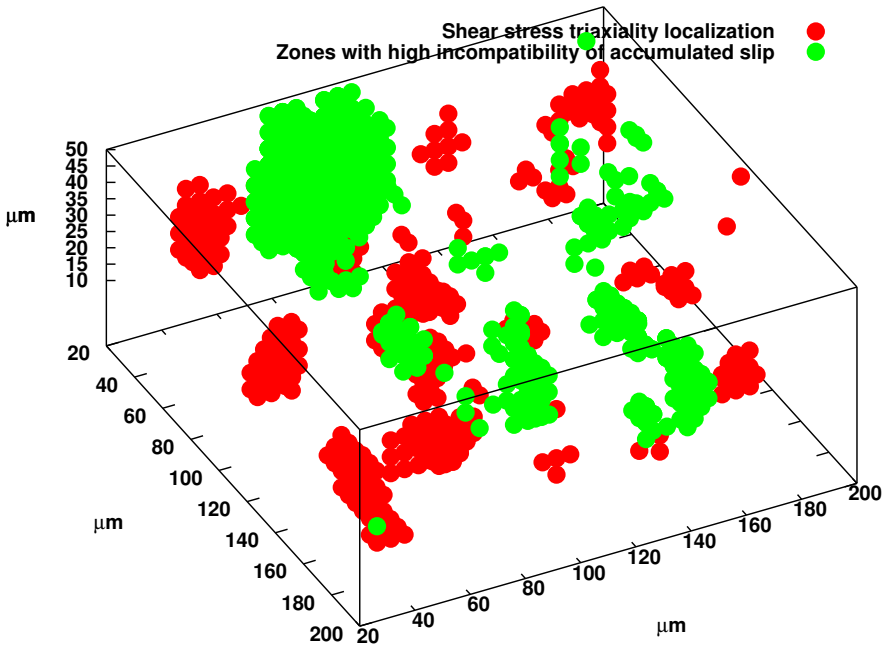

(a) stress σ_{tr} triaxiality distribution and accumulated gamma mismatch γ^{inc} and σ_{tr} MI shear 70% final step

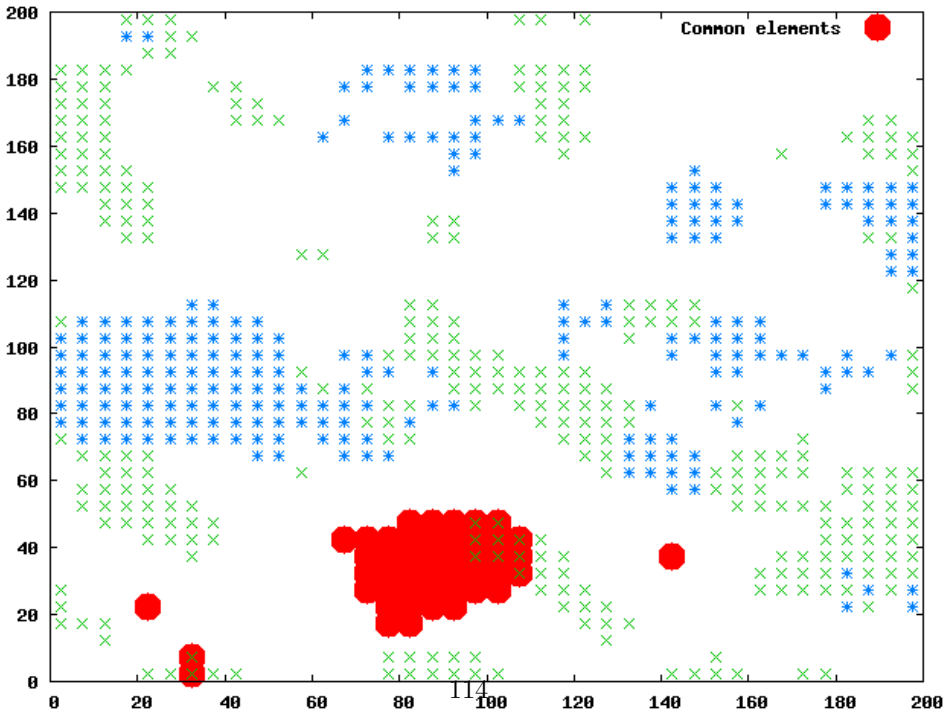

(b) Interception of the γ^{inc} and σ_{tr}

Figure 6.17: The interception of all hotspots inside the microstructure MI shear case

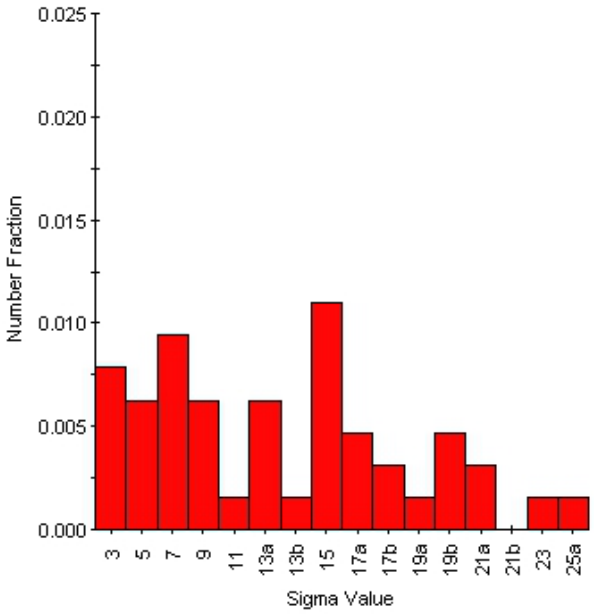

(a) Specific low angle Σ boundaries for the initial microstructure

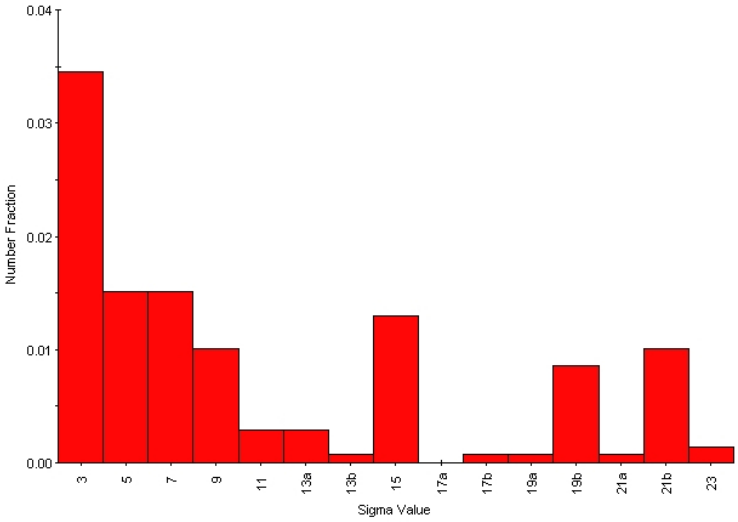

(b) Specific low angle Σ boundaries for the grains identified by a high value of the γ^{inc} - after 20% tension

Figure 6.18: CSL boundaries analyses after CPLFEM tension and shear case triaxiality.

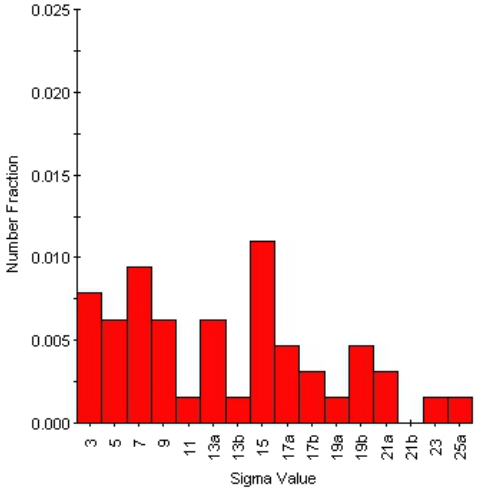

(a) Specific low angle Σ boundaries for the initial microstructure

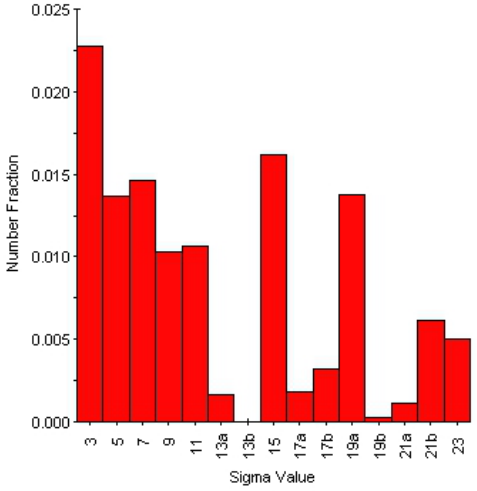

(b) Specific low angle Σ boundaries for the grains identified by a high value of the γ^{inc} after 70% shear

Figure 6.19: CSL boundaries analyses after CPLFEM simple shear case.

area of interest (as presented in Fig. 6.25) of the full $200 \times 200 \times 50\mu m$ sample. And the bottom set is the deformed crop with dimensions $50 \times 50 \times 50\mu m$. As it can be seen, each of the patterns of the deformation is nearly identical (including the local features). The grain deformation structure and Euler angles (see Fig. 6.26 (a,d)) are similar as well as the distribution of the strain (σ_{eff} (c,f)). The analysis of the Euler angles for the full and cropped structure shows that the "blue" grain orientation is harder than the surrounding grains, which have the softer orientations ("red"). This type of neighborhood causes high strain incompatibility as the softer grains tend to deform more easily than the harder ones.

The similar effect of the localized deformation for the combination of the hard and soft grains was shown in the work of [98] The results presented show that the localized combination of the hard and soft grains can have a significant effect on the deformation and strain localization, hence, on the possible fracture initiation. These results are significantly different compared to the tension test, where, as it was shown in the previos section, the same localization of the texture does not cause any specific localization of γ^{inc} or σ_{tr}. The results support the conclusion that incompatibilities on the microstructural level are strongly influenced by the deformation path and there is no universal combination of grains that would cause the incompatibilities formation during different strain paths. Thus, the optimized microstructure can be obtained for the specific deformation load only, and the same microstructure would not give the same results if it is used for the different strain path.

6.5 Conclusions

The presented paper suggests the new methods to analyze the incompatibilities occur during the deformation. As an example, aluminum DC 5754 material was used in the CPFEM simulations. The concept of

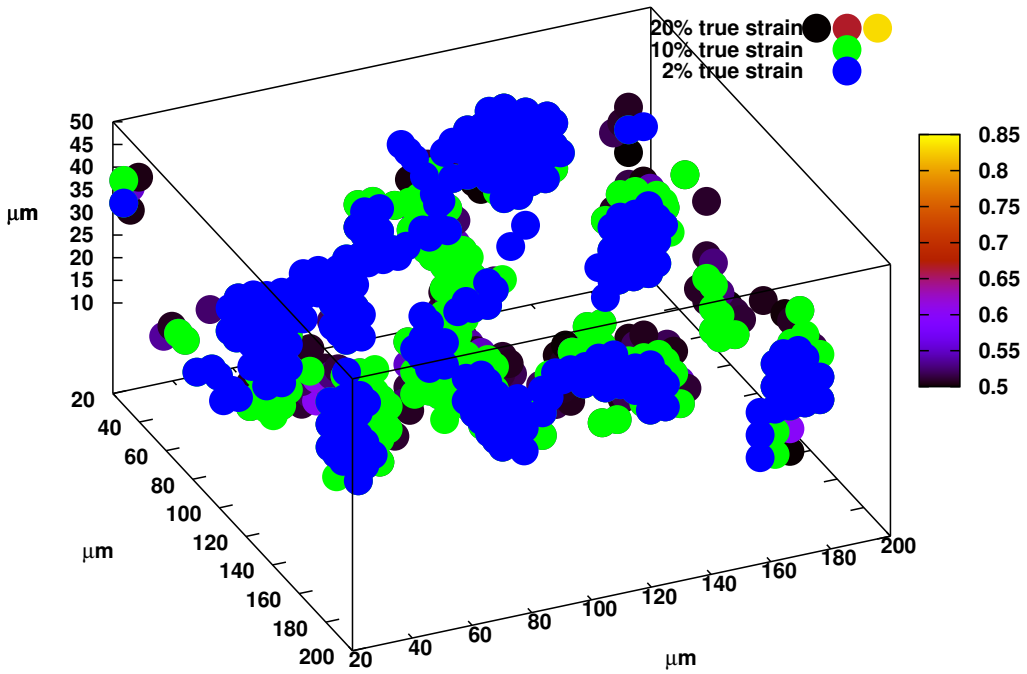

Figure 6.20: stress σ_{tr} triaxiality distribution in the dynamic load uniaxial tension MI

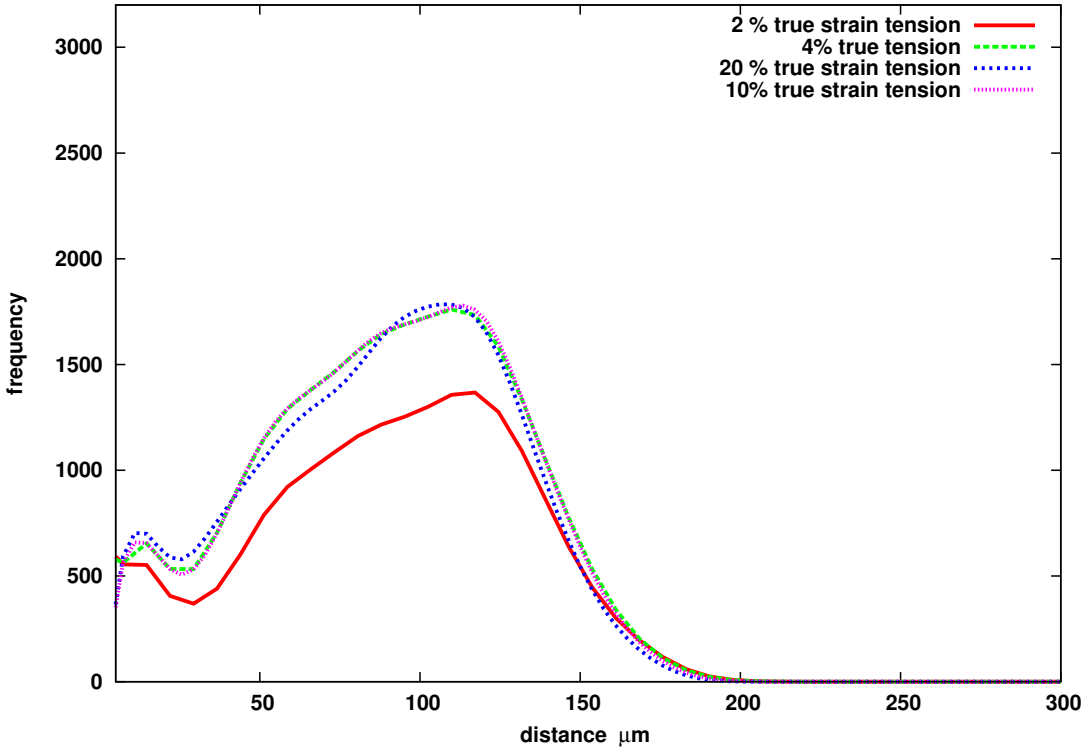

Figure 6.21: ρ_{tr} density function for different strain levels tension case

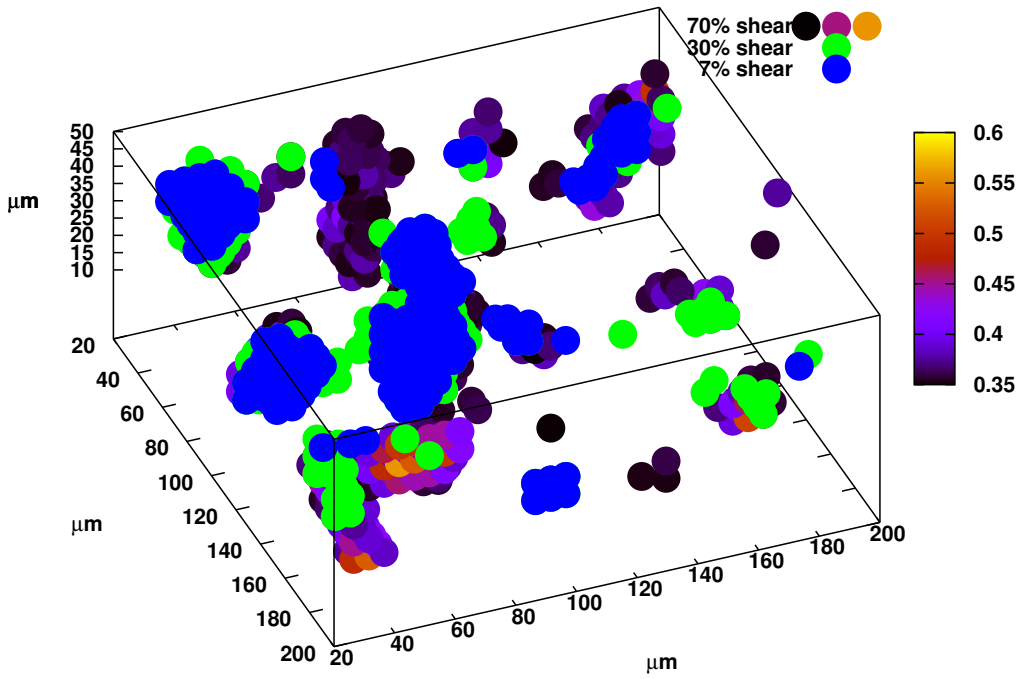

Figure 6.22: stress σ_{tr} triaxiality distribution in the dynamic load simple shear MI

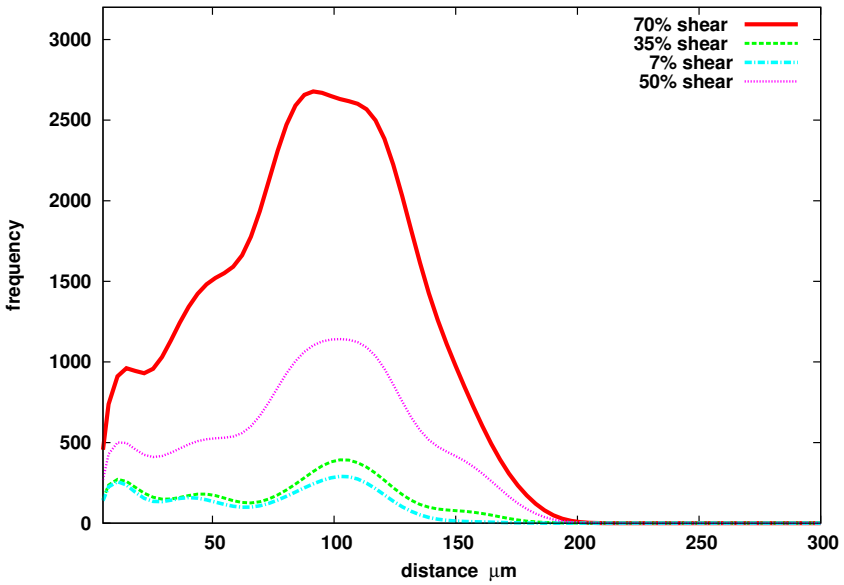

Figure 6.23: ρ_{tr} density function for different strain levels tension case

the analysis can be divided into two main categories. First, the identification of the hot spots of the deformation, and then, the analysis of the dynamics of their measurements. The presented cross-correlation analysis, method of hot spots identification and comparison in 3D give a tool for the analysis of the hot spots localization and their distribution without making any crops of the data or specific points of interest. One of the goals of the present research was to see the common patterns in the incompatibilities of the stress and strain (slip) metrics during deformation on the polycrystal level.

Various incompatibilities are analyzed for different microstructures and the effect of the random sampling is excluded. This was concluded using the analysis of the deformation and localization patterns rather than making a global conclusions about deformation.

The current research shows the following important results:

1. Localization and incompatibilities of the stress (σ_{tr}) and strain (γ_{inc}) metrics are not correlated (by relative position inside the microstructure) during deformation. As it was shown, no correlation patterns of the incompatibility formation were observed for the different strain paths. That means that in the studies of the fracture initiation mechanisms, the microstructural effects, which are believed to lead to the failure, should be properly treated for the different strain paths (material with improved microstructural characteristics can be obtained for the specific load).

   However, there are similarities within the metrics of the grains, which cause the incompatibilities, these are the grains of high disorientation with higher concentration of the specific low energy CSL boundaries. The presented CPFEM results are in a good agreement with known experimental works and FEM works, although this work shows the analyses of the deformation dynamics using CPFEM techniques.

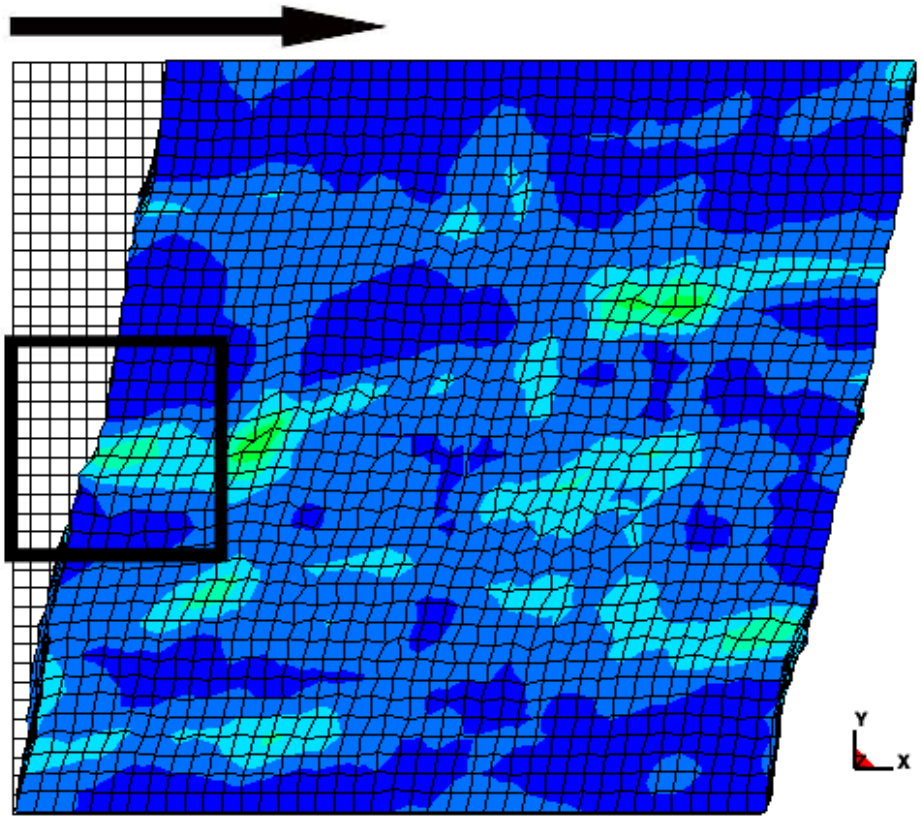

Figure 6.24: Shear on deformed and underformed grid. Window is presenting the stain localization as point of interest.

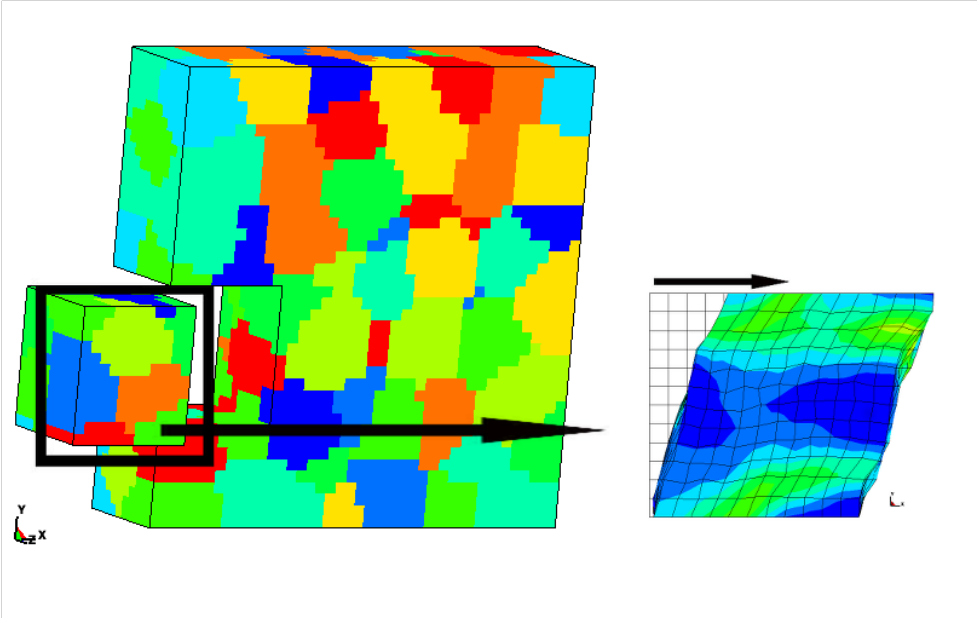

Figure 6.25: The procedure of obtaining the crop of microstructure with the zone of interest. (localization of one of the incompatibilities.)

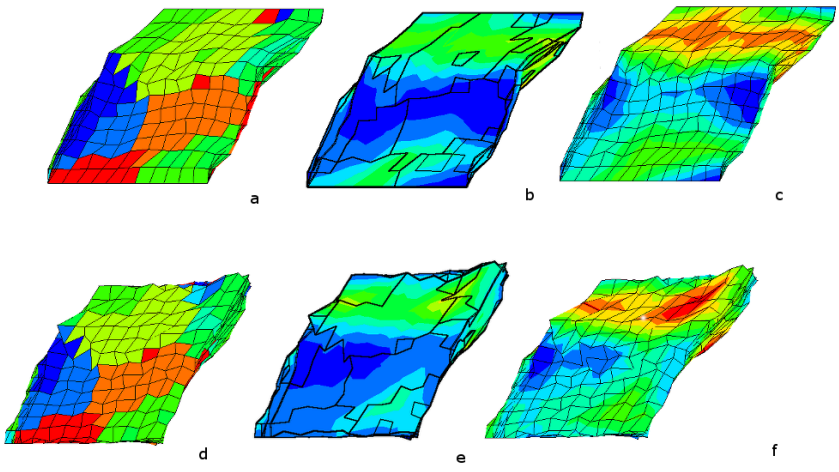

Figure 6.26: Results of the microstructure features (Euler angles, grains a,d) on the slip incompatibilities accommodation (b,e) γ^{inc} and effective strain ϵ_{eff} localization in the case of shear of the full dimensions microstructure MI and crop of the point of interest with dimensions $(50 \times 50 \times 50 \mu m)$.

2. The dynamics of the incompatibilities during deformation shows that the localization of the deformation incompatibilities σ_{tr} and γ^{inc}, which are strongly correlated with fracture initiation and propagation, is defined at the small strains ($1-2\%$ of tension and $5-7\%$ for the simple shear case). These results are important in understanding of the microstructure control for the improvement of the material properties. The preliminary results of the work suggest that the failure is pre-determined on the microstructure level and localization of incompatibilities is mostly influenced by the specific properties of the polycrystal such as grain distribution and local texture .

3. The microstructural features such as localization of specific orientations have a significant effect on the localization of the accumulated slip mismatch as well as the localization of the effective strain ϵ_{eff}. As it was shown in simulations, the grains neighboring any specific distribution of the orientations which are harder to deform have more influence on the deformation than a matrix. Both of the studied microstructures MI and MII showed the same trend, the localization zone will deform in the same way irrespective of the matrix γ^{inc} and ϵ_{eff}. As the result, it was observed that if the localization formed and slip incompatibility start accumulating, that process becomes irreversible and by fact could be explained by the lattent hardening phenomena. When some grains start accumulating and localizing slip - the slip systems in other grains become harder and harder and require significantly more energy to be activated.

Chapter 7

Thesis summary

This thesis presents new research methodologies for characterization of material microstructure and experimental design with advanced applications in the prediction of material behavior during large strain deformation. The general objective of this research work is the development of novel material microstructure analyses techniques, which can assist in improving the understanding of the contributions of the local material behavior (the microstructure) to the initiation of localized deformation and to dynamic recrystallization. Thus, the focus of the research is on the study of the specific material cross-correlation functions with further implementation into the problems of material response analyses. The study presented in this thesis; (i) develops new microstructure analyses techniques, (ii) applies these techniques to the problem of 3D microstructure reconstruction methods and, (iii) creates mathematical tools that improve our understanding of the relation between the microstructure and the macroscopic performance of a polycrystalline material.

Chapters (Chap. 2, 3) propose a new method for analyzing the material microstructure to improve our understanding of the complex physical phenomena that exist in a material on different length-scales. The proposed new analytical method is based on the so-called distance-disorientation correlation function of the microstructure. A systematic study of the distance-disorientation function is proposed to evaluate the long range dependence of texture. This function calculates the average disorientation as a function of distance between data points as measured by electron backscatter diffraction patterns. This novel investigation technique provides a measure for the clustering of texture and is used to accurately evaluate the effective grain size. This procedure in conjunction with the *Information theory* is used to estimate a representative scan size (RSS) for various polycrystalline materials. Analyses show that the optimal scan size depends on the grain morphology and the crystallographic texture. The scan area alone is not a sufficient quantity to determine the RSS. Both the asymmetry in the grain size and assymetry in the texture give rise to asymmetric RSS. Thus the extension of RSS along the Rolling Direction (RD)-Transverse Direction (TD) cross section is not enough to determine the RSS for the RD-Normal Direction (ND) cross section. The RSS obtained from such analysis should be used as an input to generate 3D microstructures as well as in numerical modeling. The RSS can also be used as building blocks for much larger samples. Accordingly, the computational integration of the DDF into the existing reconstruction models could improve the development of accurate synthetic 3D microstructures.

In order to make the next step in microstructure design and sensitive analyses problem, an in-between

step was required to establish the results for the DDF applicable to microstructure reconstruction. Following the systematic study of the DDF cross-correlation function and establishment of new methods of obtaining representative grain-level data from the measured EBSD, the analytical solution for the DDF correlation function is presented (Chap. 3). The need for the analytical solution is motivated by the complexity of obtaining DDF for real data in reconstruction problems due to a significant amount of calculations required. The proposed solution separates the crystallographic domain into texture defined by its Euler angles(ϕ_1, Φ, ϕ_2) and geometrical domain defined by distance distribution function D_{ij}. The crystallographic domain is treated as independent (known) variable and an analytical estimate for the Euclidian distance distribution function (D_{ij}) is obtained. The proposed analytical solution for the estimation of D_{ij} is based on existing statistical growth models and the logistic probability distribution function (PDF). The solution is optimized for the measured experimental data and takes into account morphological features of the microstructure such as grain volume, grain radius, grain size as well as their distribution inside the material. An analytical model is proposed for constructing the distance-disorientation function (DDF) using the estimated Euclidian distance between pixel pairs. The new functional solution is an extremely effective way to calculate DDF values, making it suitable for applications to microstructure optimization and reconstruction problems. The DDF obtained by using the results of the probabilistic solution are validated by comparison to the DDF obtained from experimental electron back-scatter diffraction (EBSD) data. After the complex problem of the integration of the DDF into the computational framework is solved, the next step in microstructure analyses is to develop a computational framework for a 3D reconstruction, which incorporates all the new knowledge from DDF.

Chapter 4 of this thesis presents a new technique for reconstructing three-dimensional (3D) microstructure from two-dimensional (2D) electron backscatter diffraction (EBSD) data (experimental). The microstructure reconstruction is performed by extending the simulated annealing techniques to perform a three-term reconstruction with the minimization of the DDF, which is combined with the new analytical solution. After establishing the novel 3D reconstruction technique, the methodology similar to the 2D RSS is employed to determine the 3D representative volume element (RVE). The 3D RVE contains all the relevant microstructure information for accurately computing the large strain deformation of solids, especially when local micro-structural variations influence the general response of the material. The new (generated) microstructures are used as a tool for understanding the effects of the local texture clustering on the important material phenomena such as initation and propogation of localized deformation and dynamic re-crystallization.

Chapters (5, 6) present the applications of the RSS and RVE to material design and to predictions of the material behavior during straining. DRX and micro- localization are chosen as the focus of the study due to the strong evidence that these two phenomena on the clustering of the micro-structural properties. The effects of the local texture on the nucleation of the new grains during re-crystallization are discussed in detail. The importance of the RSS on the modeling of the DRX phenomena is presented in 5. The application of the RVE is highlighting important observations made recently in the material design community. Both strain and stress modes are important characteristics of the material failure. This work demonstrates that a material is as strong as the weakest point inside it (the localization process is irreversible), and the determination of this weakest points require accurate representation of the 3D microstructure.

7.1 Future work Recommendations

The research presented in this thesis offers a latge number of possible directions to be taken in the future. As a topic of primary importance to the RSS study, the effect of the second phase particles should be mentioned. As it was shown in Rollet et al. [11] the experimental particle distribution should be included at the statistical level. The so-called particle correlation function (PCF) should be studied in conjunction with the already developed numerical frameworks based on the minimization of the information entropy. There is little doubth that the particle information would change the RSS. The particle distributions will add another level of non-homogeneity to the scale of analyses for the RSS research, which will improve the precision of the measurements of the EBSD data used for computational purposes.

After improving the statistical characterization level of the research, the next suggested direction is an unconstrained parametric optimization study to evaluate the role of various parameters in the microstructure in the mechanical response. The idea behind this approach is to demonstrate, based on the DDF parameter space constructed on the axes of main morphological estimators at different deformation modes, which of the DDF curves, and corresponding grain distributions and morphologies, can improve and affect various material performance. This approach coupled with the Crystal Plasticity Finite Element Model (CPFEM) will enable the evaluation of the effects of the grain morphologies, spatial orientation distributions and certain texture components on the initiation and propagation of non-uniform deformation. The local strain distribution between the grains can be investigated in detail since neighbor interactions (interactions of grains within the texture map) are the main factor in determining the spread of the applied deformation among the crystals. Combining the results from above, the microstructure with the most optimal mechanical properties can be identified through CPFEM predictions. Those predictions can be then used to identify material production conditions that would deliver potentially more effective microstructures. Finally, the CPFEM approach can be employed to determine a micro-scale dependent relation between the microstructure and the different material performance metrics (energy absorption capability, recrystallization, formability, etc.).

References

[1] Nali Li, Guangjie Huang, Xiaoyu Zhong, and Qing Liu. Deformation mechanisms and dynamic recrystallization of az31 mg alloy with different initial textures during hot tension. *Materials & Design*, 2013.

[2] B.L. Adams, A. Henrie, B. Henrie, M. Lyon, S.R. Kalidindi, and H. Garmestani. Microstructure-sensitive design of a compliant beam. *Journal of the Mechanics and Physics of Solids*, 49(8):1639–1663, 2001. cited By (since 1996) 71.

[3] M. Lyon and B.L. Adams. Gradient-based non-linear microstructure design. *Journal of the Mechanics and Physics of Solids*, 52(11):2569–2586, 2004. cited By (since 1996) 23.

[4] Shankar Ganapathysubramanian and Nicholas Zabaras. Deformation process design for control of microstructure in the presence of dynamic recrystallization and grain growth mechanisms. *International Journal of Solids and Structures*, 41(7):2011 – 2037, 2004.

[5] Veera Sundararaghavan and Nicholas Zabaras. Design of microstructure-sensitive properties in elasto-viscoplastic polycrystals using multi-scale homogenization. *International Journal of Plasticity*, 22(10):1799 – 1824, 2006.

[6] Surya R. Kalidindi, Joshua R. Houskamp, Mark Lyons, and Brent L. Adams. Microstructure sensitive design of an orthotropic plate subjected to tensile load. *International Journal of Plasticity*, 20(89):1561 – 1575, 2004.

[7] H J Bunge. *Texture Analysis in Materials Science*. Butterworths (London and Boston), 1982.

[8] U.F. Kocks and H. Mecking. Physics and phenomenology of strain hardening: the fcc case. *Progress in Materials Science*, 48(3):171 – 273, 2003.

[9] P.J. Gregson and H.M. Flower. Microstructural control of toughness in aluminium-lithium alloys. *Acta Metallurgica*, 33(3):527 – 537, 1985.

[10] Anthony D Rollett, S-B Lee, R Campman, and GS Rohrer. Three-dimensional characterization of microstructure by electron back-scatter diffraction. *Annu. Rev. Mater. Res.*, 37:627–658, 2007.

[11] AD Rollett, D Saylor, J Fridy, BS El-Dasher, A Brahme, S-B Lee, C Cornwell, and R Noack. Modeling polycrystalline microstructures in 3d. *AIP Conference Proceedings*, 712:71, 2004.

[12] David T Fullwood, Stephen R Niezgoda, Brent L Adams, and Surya R Kalidindi. Microstructure sensitive design for performance optimization. *Progress in Materials Science*, 55(6):477–562, 2010.

[13] Eugène Cosserat, François Cosserat, Maurizio Brocato, and Konstantinos Chatzis. *Théorie des corps déformables*. A. Hermann Paris, 1909.

[14] M.J. Beran and J.J. McCoy. The use of strain gradient theory for analysis of random media. *International Journal of Solids and Structures*, 6(9):1267 – 1275, 1970.

[15] AP Roberts and Max Teubner. Transport properties of heterogeneous materials derived from gaussian random fields: Bounds and simulation. *Physical Review E*, 51(5):4141, 1995.

[16] Anthony P Roberts. Statistical reconstruction of three-dimensional porous media from two-dimensional images. *Physical Review E*, 56(3):3203, 1997.

[17] Mark D Rintoul, Salvatore Torquato, et al. Reconstruction of the structure of dispersions. *Journal of colloid and interface science*, 186(2):467–476, 1997.

[18] CLY Yeong and S Torquato. Reconstructing random media. ii. three-dimensional media from two-dimensional cuts. *Physical Review E*, 58(1):224, 1998.

[19] CLY Yeong and S Torquato. Reconstructing random media. *Physical Review E*, 57(1):495, 1998.

[20] David Basanta, Peter Bentley, Mark Miodownik, and Elizabeth Holm. Evolving cellular automata to grow microstructures. *Genetic Programming*, 2610:77–130, 2003.

[21] BL Hansen, BL Adams, ME Lyon, and AJ Henrie. On the reconstruction of polycrystalline microstructures from two-point correlation statistics. *Journal of computer-aided materials design*, 10(3):163–173, 2005.

[22] H Lee, M Brandyberry, A Tudor, and K Matouš. Three-dimensional reconstruction of statistically optimal unit cells of polydisperse particulate composites from microtomography. *Physical Review E*, 80(6):061301, 2009.

[23] M. Baniassadi, S. Ahzi, H. Garmestani, D. Ruch, and Y. Remond. New approximate solution for n-point correlation functions for heterogeneous materials. *Journal of the Mechanics and Physics of Solids*, 60(1):104 – 119, 2012.

[24] M.E. Glicksman, K.G. Wang, and P. Crawford. Stochastic Effects in Microstructure. *Materials Research*, 5:231 – 241, 09 2002.

[25] K.G. Wang, M.E. Glicksman, and K. Rajan. Length scales in phase coarsening: Theory, simulation, and experiment. *Computational Materials Science*, 34(3):235 – 253, 2005.

[26] K. G. Wang, M. E. Glicksman, and Chaogang Lou. Correlations and fluctuations in phase coarsening. *Phys. Rev. E*, 73:061502, Jun 2006.

[27] Y. Jiao, F. H. Stillinger, and S. Torquato. Geometrical ambiguity of pair statistics. ii. heterogeneous media. *Physical Review E - Statistical, Nonlinear, and Soft Matter Physics*, 82(1), 2010.

[28] Stephen R. Niezgoda, David M. Turner, David T. Fullwood, and Surya R. Kalidindi. Optimized structure based representative volume element sets reflecting the ensemble-averaged 2-point statistics. *Acta Materialia*, 58(13):4432 – 4445, 2010.

[29] Siddiq M. Qidwai, David M. Turner, Stephen R. Niezgoda, Alexis C. Lewis, Andrew B. Geltmacher, David J. Rowenhorst, and Surya R. Kalidindi. Estimating the response of polycrystalline materials using sets of weighted statistical volume elements. *Acta Materialia*, 60(1314):5284 – 5299, 2012.

[30] Peter B.Corson. Correlation functions for predicting properties of heterogeneous materials. *Journal of applied Physics*, 45(7):3165–3170, 1974.

[31] S Torquato and G Stell. Microstructure of two-phase random media. i. the n-point probability functions. *The Journal of Chemical Physics*, 77:2071, 1982.

[32] S Torquato, B Lu, and J Rubinstein. Nearest-neighbor distribution functions in many-body systems. *Physical Review A*, 41(4):2059, 1990.

[33] V. Sundararaghavan and A. Kumar. Probabilistic modeling of microstructure evolution using finite element representation of statistical correlation functions. *International Journal of Plasticity*, 30 31(0):62 – 80, 2012.

[34] H. Garmestani, S. Lin, B.L. Adams, and S. Ahzi. Statistical continuum theory for large plastic deformation of polycrystalline materials. *Journal of the Mechanics and Physics of Solids*, 49(3):589 – 607, 2001.

[35] A Tewari, A.M Gokhale, J.E Spowart, and D.B Miracle. Quantitative characterization of spatial clustering in three-dimensional microstructures using two-point correlation functions. *Acta Materialia*, 52(2):307 – 319, 2004.

[36] Brent L. Adams, Xiang (Carl) Gao, and Surya R. Kalidindi. Finite approximations to the second-order properties closure in single phase polycrystals. *Acta Materialia*, 53(13):3563 – 3577, 2005.

[37] S. Torquato. Optimal design of heterogeneous materials. *Annual Review of Materials Research*, 40(1):101–129, 2010.

[38] C. J. Gommes, Y. Jiao, and S. Torquato. Microstructural degeneracy associated with a two-point correlation function and its information content. *Phys. Rev. E*, 85:051140, May 2012.

[39] C. J. Gommes, Y. Jiao, and S. Torquato. Density of states for a specified correlation function and the energy landscape. *Phys. Rev. Lett.*, 108:080601, Feb 2012.

[40] Zhaohui Shan and Arun M Gokhale. Representative volume element for non-uniform micro-structure. *Computational Materials Science*, 24(3):361 – 379, 2002.

[41] F.J. Humphreys. Review grain and subgrain characterisation by electron backscatter diffraction. *Journal of Materials Science*, 36:3833–3854, 2001.

[42] M. Groeber, S. Ghosh, M.D. Uchic, and D.M. Dimiduk. A framework for automated analysis and simulation of 3d polycrystalline microstructures. *Acta Materialia*, 56(6):1274–1287, 2008. cited By (since 1996) 31.

[43] A. Brahme, M.H. Alvi, D. Saylor, J. Fridy, and A.D. Rollett. 3d reconstruction of microstructure in a commercial purity aluminum. *Scripta Materialia*, 55(1):75 – 80, 2006.

[44] Jonathan E. Spowart. Automated serial sectioning for 3-d analysis of microstructures. *Scripta Materialia*, 55(1):5 – 10, 2006. ¡ce:title¿Viewpoint set no. 41 3D Characterization and Analysis of Materials Organized by G. Spanos¡/ce:title¿.

[45] J. A Venables and C" "J Harland. Electron back-scattering patterns new technique for obtaining crystallographic information in the scanning electron microscope. *Phil. Mag.*, 27(5):1193–1200, 1973.

[46] Brent Adams, Stuart Wright, and Karsten Kunze. Orientation imaging: The emergence of a new microscopy. *Met. Mat. Trans. A*, 24:819–831, 1993. 10.1007/Bf02656503.

[47] K Kunze, S I Wright, B L Adams, and D J Dingley. Advances in automatic ebsp single orientation measurements. *Tex. and Micros.*, 20(1-4):41–54, 1993.

[48] D. R. Steinmetz and S. Zaefferer. Towards ultrahigh resolution ebsd by low accelerating voltage. *Mat. Sci. Tech.*, 26(6):640–645, 2010.

[49] Abhijit Brahme, Joseph Fridy, Hasso Weiland, and Anthony D. Rollett. Modeling texture evolution during recrystallization in aluminum. *Model. Simul. Mater. Sci. Eng.*, 17(1), Jan 2009.

[50] O M Ivasishin, S V Shevchenko, N L Vasiliev, and S L Semiatin. A 3-d monte-carlo (potts) model for recrystallization and grain growth in polycrystalline materials. *Mat. Sci. Eng. A.*, 433(1-2):216 – 232, 2006.

[51] Dierk Raabe and Luc Hantcherli. 2d cellular automaton simulation of the recrystallization texture of an if sheet steel under consideration of zener pinning. *Comp. Mat. Sci.*, 34(4):299 – 313, 2005.

[52] A Bhattacharyya, E El-Danaf, S R Kalidindi, and R D Doherty. Evolution of grain-scale microstructure during large strain simple compression of polycrystalline aluminum with quasi-columnar grains: Oim measurements and numerical simulations. *Int. J. Plasticity*, 17(6):861–883, 2001. Cited By (Since 1996) 59.

[53] D. Raabe, M. Sachtleber, Z. Zhao, F. Roters, and S. Zaefferer. Micromechanical and macromechanical effects in grain scale polycrystal plasticity experimentation and simulation. *Acta Mater.*, 49(17):3433–3441, 2001. Cited By (Since 1996) 122.

[54] A. Musienko, A. Tatschl, K. Schmidegg, O. Kolednik, R. Pippan, and G. Cailletaud. Three-dimensional finite element simulation of a polycrystalline copper specimen. *Acta Mater.*, 55(12):4121–4136, 2007. Cited By (Since 1996) 34.

[55] K Inal, M H Simha, and R K Mishra. Numerical modeling of second-phase particle effects on localized deformation. *J. Eng. Mat. Tech.*, 130(2):021003–1 – 021003–8, 2008.

[56] R.A. Lebensohn, R. Brenner, O. Castelnau, and A.D. Rollett. Orientation image-based micromechanical modelling of subgrain texture evolution in polycrystalline copper. *Acta Mater.*, 56(15):3914–3926, 2008. Cited By (Since 1996) 24.

[57] V V Fedorov. *Teory of imal Experiments*. Academic press (New York), 1972.

[58] Christopher A. Schuh, Mukul Kumar, and Wayne E. King. Analysis of grain boundary networks and their evolution during grain boundary engineering. *Acta Mater.*, 51(3):687 – 700, 2003.

[59] F J Humphreys. Quantitative metallography by electron backscattered diffraction. *J. Micros.*, 195(3):170–185, 1999.

[60] Stuart I. Wright, Matthew M. Nowell, and John F. Bingert. A comparison of textures measured using x-ray and electron backscatter diffraction. *Met. Mater. Trans. A*, 38A(8):1845–1855, AUG 2007.

[61] T Baudin and R Penelle. Determination of the total texture function from individual orientation measurements by electron backscattering pattern. *Met. Trans. A*, 24(10):2299–2311, OCT 1993.

[62] K. Davut and S. Zaefferer. Statistical reliability of phase fraction determination based on electron backscatter diffraction (ebsd) investigations on the example of an al-trip steel. *Met. Mater. Trans. A*, 41A:2187–2196, 2010.

[63] Benot Beausir, Claude Fressengeas, Nilesh P. Gurao, Laszlo S. Toth, and Satyam Suwas. Spatial correlation in grain misorientation distribution. *Acta Mater.*, 57(18):5382 – 5395, 2009.

[64] B.L. Adams, P.R. Morris, T.T. Wang, K.S. Willden, and S.I. Wright. Description of orientation coherence in polycrystalline materials. *Acta Metallurgica*, 35(12):2935 – 2946, 1987.

[65] N R Barton and P R Dawson. On the spatial arrangement of lattice orientations in hot-rolled multiphase titanium. *Modelling and Simulation in Materials Science and Engineering*, 9(5):433, 2001.

[66] Raymond A Ryan. *Introduction to tensor products of Banach spaces*. Springer, 2002.

[67] A Heinz and P Neumann. Representation of orientation and disorientation data for cubic, hexagonal, tetragonal and orthorhombic crystals. *Acta Crystallographica Section A: Foundations of Crystallography*, 47(6):780–789, 1991.

[68] A. Vorhauer, T. Hebesberger, and R. Pippan. Disorientations as a function of distance: A new procedure to analyze local orientation data. *Acta Mater.*, 51(3):677 – 686, 2003.

[69] Robert M Gray. *Entropy and Information Theory*. Springer-Verlag New York, 2009.

[70] S Kullback and R A Leibler. On information and sufficiency. *Ann. Math. Stat.*, 22(1):79–86, 1951.

[71] Joong Hyuk Chang and Won Suk Lee. Efficient mining method for retrieving sequential patterns over online data streams. *J. Inf. Sci.*, 31:420–432, October 2005.

[72] D. Shechtman, I. Blech, D. Gratias, and J. W. Cahn. Metallic phase with long-range orientational order and no translational symmetry. *Phys. Rev. Lett.*, 53:1951–1953, 1984.

[73] P. Debye, H. R. Anderson, and H. Brumberger. Scattering by an inhomogeneous solid. ii. the correlation function and its application. *Journal of Applied Physics*, 28(6):679–683, 1957. cited By (since 1996) 480.

[74] Samuel Forest, Fabrice Barbe, and Georges Cailletaud. Cosserat modelling of size effects in the mechanical behaviour of polycrystals and multi-phase materials. *International Journal of Solids and Structures*, 37(4647):7105 – 7126, 2000.

[75] MJ Beran, J Molyneux, et al. Use of classical variational principles to determine bounds for the effective bulk modulus in heterogeneous media. *Quart. Appl. Math*, 24(2), 1966.

[76] MJ Beran. Application of statistical theories to heterogeneous materials. *physica status solidi (a)*, 6(2):365–384, 1971.

[77] John J McCoy. Macroscopic response of continua with random microstructures. *Mechanics today*, 6:1–40, 1981.

[78] M.J. Beran, T.A. Mason, B.L. Adams, and T. Olsen. Bounding elastic constants of an orthotropic polycrystal using measurements of the microstructure. *Journal of the Mechanics and Physics of Solids*, 44(9):1543 – 1563, 1996.

[79] A Brahme, Y. Staraselski, K. Inal, and Raja Mishra. Determination of the minimum scan size to obtain representative textures by electron backscatter diffractions. *Metallurgical and Materials Transactions A*, pages 1–10. 10.1007/s11661-012-1364-5.

[80] A. Heinz and P. Neumann. Representation of orientation and disorientation data for cubic, hexagonal, tetragonal and orthorhombic crystals. *Acta Crystallographica Section A*, 47(6):780–789, Nov 1991.

[81] J S Cramer. *Logit Models from Economics and Other Fields*. Cambridge Univeristy Press, 2011.

[82] N. Balakrishnan. *Handbook of the Logistic Distribution*. Statistics, textbooks and monographs. Dekker, 1992.

[83] Gnter Gottstein. *Physical Foundations of Materials Science*. Springer, 2004.

[84] J. Rossiter, A. Brahme, K. Inal, and R. Mishra. The effects of crystal orientation on surface roughness during bending of fcc single crystals and polycrystals. *International Journal of Plasticity*, xx(xx):xx, 2012.

[85] J. Rossiter, A. Brahme, K. Inal, and R. Mishra. Distribution of stress triaxiality in face-centered cubic polycrystals under equibiaxial loading. *Scripta Materialia*, 65(3):183 – 185, 2011.

[86] A D Rollett, R A Lebensohn, M Groeber, Y Choi, J Li, and G S Rohrer. Stress hot spots in viscoplastic deformation of polycrystals. *Modelling and Simulation in Materials Science and Engineering*, 18(7):074005, 2010.

[87] Staraselski Yauheni, Abhijit Brahme, , Raja K Mishra, and Kaan Inal. Analytical estimation of distance-disorientation function of the material microstructure. *Philosophical magazine*, pages 1–12, 2012. In Press.

[88] D.M. Saylor, J. Fridy, B.S. El-Dasher, K.-Y. Jung, and A.D. Rollett. Statistically representative three-dimensional microstructures based on orthogonal observation sections. *Metallurgical and Materials Transactions A: Physical Metallurgy and Materials Science*, 35 A(7):1969–1979, 2004. cited By (since 1996) 45.

[89] T. Kanit, S. Forest, I. Galliet, V. Mounoury, and D. Jeulin. Determination of the size of the representative volume element for random composites: statistical and numerical approach. *International Journal of Solids and Structures*, 40(1314):3647 – 3679, 2003.

[90] Wei Li and Nicholas Zabaras. A virtual environment for the interrogation of 3d polycrystalline microstructures including grain size effects. *Computational Materials Science*, 44(4):1163 – 1177, 2009.

[91] M Miodownik, A.W Godfrey, E.A Holm, and D.A Hughes. On boundary misorientation distribution functions and how to incorporate them into three-dimensional models of microstructural evolution. *Acta Materialia*, 47(9):2661 – 2668, 1999.

[92] Bogdan Bochenek and Ryszard Pyrz. Reconstruction of random microstructures a stochastic optimization problem. *Computational Materials Science*, 31(12):93 – 112, 2004.

[93] Brent L Adams. Orientation imaging microscopy: application to the measurement of grain boundary structure. *Materials Science and Engineering: A*, 166(1):59–66, 1993.

[94] Stuart I Wright, Brent L Adams, and Karsten Kunze. Application of a new automatic lattice orientation measurement technique to polycrystalline aluminum. *Materials Science and Engineering: A*, 160(2):229–240, 1993.

[95] Brent L Adams, Stuart I Wright, and Karsten Kunze. Orientation imaging: the emergence of a new microscopy. *Metallurgical Transactions A*, 24(4):819–831, 1993.

[96] Nicholas Metropolis and S. Ulam. The monte carlo method. *Journal of the American Statistical Association*, 44(247):335–341, 1949.

[97] Nicholas Metropolis. The beginning of the monte carlo method. *Los Alamos Science*, 15(584):125–130, 1987.

[98] J. Rossiter, A. Brahme, M.H. Simha, K. Inal, and R. Mishra. A new crystal plasticity scheme for explicit time integration codes to simulate deformation in 3d microstructures: Effects of strain path, strain rate and thermal softening on localized deformation in the aluminum alloy 5754 during simple shear. *International Journal of Plasticity*, 26(12):1702 – 1725, 2010.

[99] Viggo Tvergaard. Material failure by void growth to coalescence. *Advances in applied Mechanics*, 27(1):83–151, 1990.

[100] T Pardoen and JW Hutchinson. An extended model for void growth and coalescence. *Journal of the Mechanics and Physics of Solids*, 48(12):2467–2512, 2000.

[101] D. Raabe. Cellular automata in materials science with particular reference to recrystallization simulation. *Annual review of materials research*, 32(1):53–76, 2002.

[102] H. Mecking and U.F. Kocks. Kinetics of flow and strain-hardening. *Acta Metallurgica*, 29(11):1865–1875, 1981.

[103] R.W. Cahn. A new theory of recrystallization nuclei. *Proceedings of the Physical Society. Section A*, 63(4):323, 1950.

[104] F.J. Humphreys and M. Hatherly. *Recrystallization and related annealing phenomena*, volume 416. Elsevier Oxford, 2004.

[105] A. Arsenlis and D.M. Parks. Crystallographic aspects of geometrically-necessary and statistically-stored dislocation density. *Acta Materialia*, 47(5):1597 – 1611, 1999.

[106] J.F Nye. Some geometrical relations in dislocated crystals. *Acta Metallurgica*, 1(2):153 – 162, 1953.

[107] A. Brahme, Y. Staraselski, R.K. Mishra, and K. Inal. A new model to predict grain nucleation during dynamic recrystallization. In *The 9th International Conference on Magnesium Alloys and their Applications (Mg 2012)*, 2012.

[108] E. Popova, Y. Staraselski, A. Brahme, R.K. Mishra, and K. Inal. Coupled crystal plasticity - cellular automata approach to model dynamic recrystallization in magnesium alloys. Submitted for publication.

[109] S.B. Yi, S. Zaefferer, and H.-G. Brokmeier. Mechanical behaviour and microstructural evolution of magnesium alloy az31 in tension at different temperatures. *Materials Science and Engineering: A*, 424(12):275 – 281, 2006.

[110] C.D. Beachem and G.R. Yoder. Elastic-plastic fracture by homogeneous microvoid coalescence tearing along alternating shear planes. *Metallurgical Transactions*, 4(4):1145–1153, 1973. cited By (since 1996)17.

[111] W.M. Garrison Jr. and N.R. Moody. Ductile fracture. *Journal of Physics and Chemistry of Solids*, 48(11):1035–1074, 1987.

[112] E.M. Bringa, S. Traiviratana, and M.A. Meyers. Void initiation in fcc metals: Effect of loading orientation and nanocrystalline effects. *Acta Materialia*, 58(13):4458–4477, 2010. cited By (since 1996)24.

[113] F.A. McClintock. *J Appl Mech*, pages 363–371, 1968. cited By (since 1996)1.

[114] O Orlov, Eric Maire, Jérôme Adrien, Michael J Worswick, and DJ Lloyd. Application of the three-dimensional damage percolation model and x-ray tomography for damage evolution prediction in aluminum alloys. 519:1011–1016, 2006.

[115] G.P. Potirniche, J.L. Hearndon, M.F. Horstemeyer, and X.W. Ling. Lattice orientation effects on void growth and coalescence in fcc single crystals. *International Journal of Plasticity*, 22(5):921 – 942, 2006.

[116] Arpan Das, Tamshuk Chowdhury, and Soumitra Tarafder. Ductile fracture micro-mechanisms of high strength low alloy steels. *Materials and Design*, 54(0):1002 – 1009, 2014.

[117] H. Ghadbeigi, C. Pinna, and S. Celotto. Failure mechanisms in {DP600} steel: Initiation, evolution and fracture. *Materials Science and Engineering: A*, 588(0):420 – 431, 2013.

[118] F.F. Jawad and M.A. Zikry. The effects of grain-boundary orientations on failure behavior in f.c.c. polycrystalline systems. *International Journal of Damage Mechanics*, 18(4):341–369, 2009.

[119] Benjamin Epstein. Statistical aspects of fracture problems. *Journal of Applied Physics*, 19(2):140–147, 1948.

[120] CIA Thomson, MJ Worswick, AK Pilkey, and DJ Lloyd. Void coalescence within periodic clusters of particles. *Journal of the Mechanics and Physics of Solids*, 51(1):127–146, 2003.

[121] Jidong Kang, David S Wilkinson, Mike Bruhis, Mukesh Jain, Pei Dong Wu, J David Embury, Raja K Mishra, and Anil K Sachdev. Shear localization and damage in aa5754 aluminum alloy sheets. *Journal of Materials Engineering and Performance*, 17(3):395–401, 2008.

[122] Clayton Stein, Sukbin Lee, and Anthony Rollett. An analysis of fatigue crack initiation using 2d orientation mapping and full-field simulation of elastic stress response. *Superalloys 2012*, pages 439–444, 2012.

[123] Ekaterina Viatkina. *Micromechanical modelling of strain path dependency in FCC metals*. Technische Universiteit Eindhoven, 2005.

[124] J. Shi and M.A. Zikry. Grainboundary interactions and orientation effects on crack behavior in polycrystalline aggregates. *International Journal of Solids and Structures*, 46(21):3914 – 3925, 2009.

[125] V.Y. Gertsman and S.M. Bruemmer. Study of grain boundary character along intergranular stress corrosion crack paths in austenitic alloys. *Acta Materialia*, 49(9):1589 – 1598, 2001.

[126] EJ GUMBEL. Statistics of extremes. 2004.